

EXOTIC NUCLEAR EXCITATIONS:
THE TRANSVERSE WOBBLING MODE IN ^{135}Pr

A Dissertation

Submitted to the Graduate School
of the University of Notre Dame
in Partial Fulfillment of the Requirements
for the Degree of

Doctor of Philosophy

by
James Till Matta

Umesh Garg, Director

Graduate Program in Physics

Notre Dame, Indiana

July 2015

© Copyright by

James Till Matta

2015

All Rights Reserved

EXOTIC NUCLEAR EXCITATIONS:
THE TRANSVERSE WOBBLING MODE IN ^{135}Pr

Abstract

by

James Till Matta

The exotic collective excitation transverse wobbling has been investigated in the nucleus, ^{135}Pr . A pair of zero and one-phonon wobbling bands has been observed. The nature of these wobbling bands was confirmed by the $\Delta I = 1, E2$ nature of the $n_w = 1 \rightarrow n_w = 0$ interband transitions making ^{135}Pr the first nucleus observed to exhibit wobbling behavior other than five nuclei in the $A \sim 160$. Additionally, a possible two-phonon wobbling band has been observed and its nature has been partially confirmed by measuring the $\Delta I = 1, E2$ nature of the $n_w = 2 \rightarrow n_w = 1$ interband transitions. The theory of transverse wobbling was proposed to explain contradictions in the wobbling energy predicted by previous quasiparticle plus triaxial rotor calculations; this theory has been confirmed. In this model, the quasiparticle aligns with an axis perpendicular to the axis with maximal moment of inertia (in contrast to previous theories, which aligned the quasiparticle with the axis with maximum moment of inertia). With this modification the fall in the energy of the wobbling phonon, observed in experiment, is now correctly predicted by theory. This confirmation of theory suggests a reevaluation of the previously discovered wobbling nuclei in the $A \sim 160$ region in the framework of transverse wobbling as well.

DEDICATION:

To my fiancé Tina.

&

To my parents, James and Margaret.

In loving recognition of their support.

CONTENTS

FIGURES	v
TABLES	x
ACKNOWLEDGMENTS	xi
SYMBOLS	xiv
CHAPTER 1: INTRODUCTION	1
1.1 Rotation of Deformed Nuclei	1
1.1.1 Axial Deformation	1
1.1.2 Triaxiality	2
1.1.2.1 Chirality	3
1.1.2.2 Wobbling	3
1.1.2.3 Triaxiality in the $A \sim 130$ Region	4
1.2 Previous Cases of Wobbling	5
1.3 Motivation	6
CHAPTER 2: NUCLEAR MODELS FOR HIGH SPIN PHENOMENA	10
2.1 Introduction	10
2.2 The Shell Model	13
2.3 The Deformed Shell Model	15
2.3.1 Parameterization of Deformation	15
2.3.2 The Nilsson Model	17
2.4 Collective Rotation	20
2.4.1 Rigid Triaxial Rotor Model (TRM)	20
2.4.2 Quasiparticle + Triaxial Rotor (QTR)	25
2.4.3 Pairing	26
2.4.4 Tilted Axis Cranking	29
2.4.4.1 Rotation About A Principal Axis	33
2.4.4.2 Rotation About A Tilted Axis	35
2.5 The Wobbling Mode in Nuclei	36
2.5.1 Models of the Wobbling Mode	36
2.5.1.1 Simple Wobbling	36
2.5.1.2 Transverse Wobbling	39

2.5.1.3	Longitudinal Wobbling	42
2.5.2	Signatures of Wobbling	43
CHAPTER 3: EXPERIMENTAL METHODS		44
3.1	Heavy-ion Fusion-evaporation Reaction	44
3.1.1	Creation and Decay of the Compound Nucleus	44
3.1.2	Choice of Beam and Target	48
3.2	Gamma-ray Spectroscopy	49
3.2.1	Gamma-ray Interaction with Matter	49
3.2.2	High Purity Germanium (HPGe) Detectors	53
3.2.3	Escape Suppression with BGO Detectors	58
3.2.4	The Gammasphere Detector Array	60
3.2.5	Indian National Gamma Array (INGA)	62
3.3	Experimental Details	64
3.3.1	ATLAS/Gammasphere	65
3.3.2	TIFR - BARC Pelletron LINAC / INGA	66
3.4	Data Processing	67
3.4.1	Calibration	68
3.4.2	Level Scheme Scheme Determination	73
3.4.3	Background Subtraction	75
3.4.3.1	Symmetric Gates	75
3.4.3.2	Asymmetric Gates	76
3.5	Directional Correlation of Gamma-rays from Oriented Nuclei (DCO)	80
3.5.1	Angular Distributions	84
3.5.2	DCO Ratios	85
3.5.3	Polarization	87
CHAPTER 4: TRANSVERSE WOBBLING IN ^{135}Pr		90
4.1	Level Scheme of ^{135}Pr	90
4.1.1	Angular Distributions and DCO-like Ratios	98
4.1.2	Polarizations	102
4.2	Description by Theory	103
4.3	Discussion	107
CHAPTER 5: SUMMARY AND OUTLOOK		111
APPENDIX A: GAMMASPHERE RING AND DETECTOR INFORMATION		113
APPENDIX B: INGA RING AND DETECTOR INFORMATION		135
APPENDIX C: NEGATIVE PARITY LEVEL AND TRANSITION INFORMATION		142
BIBLIOGRAPHY		152

FIGURES

1.1 Quadrupole deformation parameter β_2 across the nuclear chart. Plot adapted from [93] which used data from [76].	2
1.2 Partial level schemes of ^{163}Lu (left) and ^{165}Lu (right). Figures adapted from Ref. [60] and Ref. [102], respectively. In ^{163}Lu the $n_w = 0, 1, 2$ bands are labeled TSD1, TSD2, and TSD3, respectively. In ^{165}Lu the $n_w = 0, 1, 2$ bands are labeled TSD1, TSD2, and TSD3, respectively.	6
1.3 Partial level schemes of ^{167}Lu (left) and ^{161}Lu (right). Figures adapted from Ref. [1] and Ref. [23], respectively. In ^{167}Lu the $n_w = 0, 1$ bands are labeled TSD1 and TSD2, respectively. In ^{161}Lu the $n_w = 0, 1$ bands are labeled TSD1 and TSD2, respectively.	7
1.4 Partial level scheme of ^{167}Ta . Figure adapted from Ref. [54]. The $n_w = 0, 1$ bands are labeled TSD1 and TSD2, respectively.	8
1.5 Wobbling frequencies of the $A \sim 170$ wobblers. Top Left: ^{163}Lu . Top Right: ^{165}Lu . Middle Left: ^{167}Lu . Middle Right: ^{161}Lu . Bottom: ^{167}Ta .	9
2.1 Binding energies per nucleon plotted versus mass number. Values calculated from Ref. [3, 118].	11
2.2 Left: Two proton separation energies plotted versus proton number. Each line is a set of isotones. Right: Two neutron separation energies plotted versus neutron number. Each line is a set of isotopes. Values calculated from Ref. [3, 118].	12
2.3 Left: First excited 2^+ energies of nuclei with even Z and N, plotted versus proton number. Each line is a set of isotones. Right: First excited 2^+ energies of nuclei with even Z and N, plotted versus neutron number. Each line is a set of isotopes. Figures adapted from Ref. [97].	12
2.4 Schematic of a square well, SHO potential, and a realistic Woods-Saxon potential. Figure adapted from Ref. [26].	14
2.5 Spectrum of a single nucleon in an SHO potential, SHO + l^2 , and, SHO + l^2 + spin-orbit. Figure adapted from Ref. [26].	14
2.6 Schematic of the Lund convention. Figure adapted from Ref. [4].	17

2.7 Schematic of an axially symmetric nucleus and the various quantum numbers that are used in the description of the system. Here R is the angular momentum of collective rotation, J is the total nuclear angular momentum, j is the total angular momentum of the particle, l is the orbital angular momentum of the particle, s is the spin of the particle, M is the projection of J onto the non-symmetry axis, K is the projection of J onto the symmetry axis, Ω is the projection of j onto the symmetry axis, Λ is the projection of l onto the symmetry axis, and Σ is the projection of s onto the symmetry axis. Figure adapted from Ref. [4].	19
2.8 Nilsson diagram for protons in the $50 \leq Z \leq 82$ region with $\epsilon_4 = \epsilon_2/6$. Solid lines represent positive parity orbitals and dashed lines represent negative parity orbitals. Labels follow the $\Omega[N\ n_z\ \Lambda]$ convention. Figure adapted from Ref. [93].	21
2.9 Nilsson diagram for neutrons in the $50 \leq N \leq 82$ region with $\epsilon_4 = \epsilon_2/6$. Solid lines represent positive parity orbitals and dashed lines represent negative parity orbitals. Labels follow the $\Omega[N\ n_z\ \Lambda]$ convention. Figure adapted from Ref. [93].	22
2.10 One neutron separation energies vs neutron number for the five isotopes from $Z = 51$ to $Z = 55$. The staggering between even and odd masses gives strong evidence for the pairing interaction. Additionally the $N = 82$ shell gap can be seen. Figure adapted from Ref. [93].	27
2.11 Schematic of the occupancy of single particle states with and without pairing. Figure adapted from Ref. [117].	28
2.12 Orientation of the rotational axis with respect to the principal axes of the deformed density distribution. Figure taken from Ref. [4].	32
2.13 Discrete symmetries of the mean field of a rotating triaxial nucleus for each of the TAC solutions along with schematics of the band structures that arise from each solution. The axis of rotation (z), which coincides with the \vec{J} , is marked with a circular arrow. The operators are: \mathcal{P} : Parity inversion, $\mathcal{R}_{y,z}$ Rotation by π about the y or z axis, and \mathcal{T} : Time reversal. Figure adapted from Ref. [38].	34
2.14 Intersections of the angular momentum and energy surfaces for a simple wobbling system with $A_1 = 6 * A_3$ and $A_2 = 3A_3$ for $J = 2$ taken at progressively larger energies from a to c. Figure adapted from Ref. [41].	38
2.15 Intersections of the angular momentum and energy surfaces for a transverse wobbling system with $A_1 = 6 * A_2$ and $A_3 = 3A_2$ for $J = 3$ taken at progressively larger various energies from a to c. Figure adapted from Ref. [41].	40

3.1	Schematic illustration of heavy-ion fusion-evaporation, adapted from Ref. [69].	46
3.2	Isocontours of angular momenta that yield fission barriers of 8 MeV and 0 MeV at various masses. Note that the 0 MeV height barrier occurs at higher spins for a given mass, showing the inverse dependence of fission barrier height on angular momentum. Adapted from Ref. [29].	47
3.3	Schematic of the compound nuclear decay assuming that a rotational nucleus is being formed. Adapted from Ref. [4].	48
3.4	Cross-sections of various residual nuclei for a ^{16}O beam on ^{123}Sb at a variety of beam energies as calculated by PACE4. As ^{139}Pr is the compound nucleus produced all products that are not isotopes of Pr require the evaporation of a charged particle.	50
3.5	Gamma-ray attenuation coefficients for various processes in NaI, adapted from Ref. [63]. Note the dominance of photoelectric absorption at lower energies, Compton scattering at intermediate energies, and pair production at high energies. While the slopes of these processes change from material to material, the trends remain the same.	52
3.6	Above: Diagrammatic view of the depletion zone's with varying bias voltage. Below: Voltage difference across the depletion zone for each bias voltage shown above.	54
3.7	Diagram showing the uncertainty inherent in the gamma ray's angle of emission, and Gammasphere's segmented electrode scheme to reduce this.	56
3.8	Schematic of BGO escape suppression around an HPGE crystal.	58
3.9	Superimposed spectra of an escape suppressed and unsuppressed detector. Adapted from Ref. [69].	59
3.10	View of scattering chamber and interior of one of Gammasphere's hemispheres pulled back from the chamber. The hexagonal copper foils are x-ray absorbers.	61
3.11	Cross-section schematic of part of Gammasphere. Adapted from Ref.[69].	62
3.12	Exterior view of INGA.	63
3.13	Example isomer timing spectrum for INGA. From Ref. [87].	64
3.14	Histogram of the number of events in each multiplicity for the experiment at Gammasphere.	68
3.15	^{152}Eu calibration spectrum from a typical Gammasphere detector.	71
3.16	Typical ^{152}Eu and ^{133}Ba mixed source calibration spectrum from a single crystal of an INGA clover detector.	71
3.17	^{152}Eu extracted relative efficiencies and fit.	73
3.18	Total projection spectrum and its smooth background drawn below it.	76

3.19	Spectra of a symmetric triple gate on a hypercube showing the components of the gates spectrum. Top: The unsubtracted gated spectrum. Middle: The background spectrum for the gate. Bottom: The final background subtracted spectrum.	77
3.20	Extraction of the peak and background, where $p + b = 1$. Adapted from Ref. [109].	79
3.21	Emission of two successive radiations X_1 and X_2 from an oriented nuclear state, I_1	81
3.22	Diagram of the angles in a directional correlation of two successive radiations X_1 and X_2 emitted from an axial symmetric oriented source S.	82
3.23	Natural asymmetries and the linear fit to them.	88
4.1	Previous level scheme for ^{135}Pr , from Ref. [103].	90
4.2	Negative parity rotational band structure proposed for ^{135}Pr in Ref. [103].	91
4.3	Yrast band for ^{135}Pr presented in Ref. [90].	92
4.4	Top: Background spectrum for the symmetrized cube. Bottom: Background spectrum for the symmetrized hypercube.	93
4.5	Negative parity level scheme developed for ^{135}Pr	94
4.6	Sum of all possible double gates on M1 transitions in the dipole band. The labeling of the transitions is color coded according to the band the transition belongs to.	95
4.7	Triple gate on the specified transitions. The labeling of the transitions is color coded according to the band to which a transition belongs.	96
4.8	Important angular distributions fitted in this work. Top Left: The first $n_w = 1 \rightarrow n_w = 0$ transition (747.0 keV). Top Right: The second $n_w = 1 \rightarrow n_w = 0$ transition (812.8 keV). Mid Left: The third $n_w = 1 \rightarrow n_w = 0$ transition (754.6 keV). Mid Right: The first possible $n_w = 2 \rightarrow n_w = 1$ transition (450.1 keV). Bottom Left: The first signature partner to yrast transition (593.9 keV). Bottom Right: The fifth yrast in-band transition (1075.5 keV).	99
4.9	DCO-like ratios plotted versus transition energy for a wide variety of transitions in ^{135}Pr	101
4.10	Polarization asymmetries versus transition energy for several transitions in ^{135}Pr	103
4.11	Wobbling energies from experiment and QTR theory of the $n_w = 1$ band. Error bars for energies are not plotted as they are smaller than the plotted points.	106

TABLES

3.1	GAMMASPHERE FEATURE SUMMARY	60
3.2	INGA FEATURE SUMMARY	65
3.3	^{152}Eu PEAK DATA	69
3.4	^{133}Ba PEAK DATA	70
3.5	TYPICAL VALUES OF ANGULAR DISTRIBUTION COEFFICIENTS A_2 , A_4 FOR GAMMA-RAYS WITH DIPOLE (D), QUADRUPOLE (Q), OR MIXED DIPOLE-QUADRUPOLE MULTIPOLARITY, L . .	85
3.6	TYPICAL VALUES OF DCO RATIOS AND DCO-LIKE RATIOS FOR THE GAMMASPHERE ARRAY	87
4.1	TABLE OF EXTRACTED MIXING RATIOS, POLARIZATION ASYM- METRIES, AND $E2$ PERCENTAGES FOR THE $n_w = 1$, POSSIBLE $n_w = 2$, AND SIGNATURE PARTNER BANDS.	104
4.2	TABLE OF REDUCED TRANSITION PROBABILITIES CALCULATED FROM DATA AND FROM QTR THEORY FOR THE $n_w = 1 \rightarrow n_w = 0$ TRANSITIONS.	108
A.1	GAMMASPHERE RING CHARACTERISTICS.	114
A.2	GAMMASPHERE DETECTOR AZIMUTHAL ANGLES.	115
A.3	GAMMASPHERE MISSING DETECTORS.	116
A.4	GAMMASPHERE ENERGY CALIBRATION POLYNOMIALS . .	117
A.5	GAMMASPHERE RELATIVE EFFICIENCY CALIBRATION PA- RAMETERS	126
B.1	INGA RING CHARACTERISTICS.	136
B.2	INGA POCKET AND DETECTOR ELECTRONICS INFORMATION	137
B.3	INGA ENERGY CALIBRATION POLYNOMIALS	138
C.1	TABLE OF LEVEL INFORMATION FOR NEGATIVE PARITY ^{135}Pr , SORTED BY BAND	142
C.2	TABLE OF GAMMA-RAY TRANSITION INFORMATION FOR NEG- ATIVE PARITY ^{135}Pr SORTED BY GAMMA-RAY ENERGY . .	145

ACKNOWLEDGMENTS

In the long and difficult period I have been a student at Notre Dame many individuals have assisted me, giving their time, scientific guidance, and emotional support, without them I would have failed in this task and I remain indebted to them. I would like to sincerely thank every contributor to this work; thank you.

Foremost, I would like to offer my most profound thanks to Dr. Umesh Garg, my research advisor here at Notre Dame. I am grateful for his introducing me to the world of nuclear physics. Without his guidance, none of this would have been possible. Without his understanding, I would not have succeeded. His push to constantly improve my analysis and test *why* something happens rather than simply accept it has had a major impact on me and my way of thinking. Without his patience, comments, and advice, this manuscript would be much poorer. I am profoundly grateful for his advice and assistance.

I would like to thank my committee, past and present, for their assistance and advice. To Dr. James Kolata and Dr. Collin Jessop, I would like to apologize for the scheduling problems that prevented your participation in the defense, and accept my sincere thanks for steering my research and giving good advice on post-doctorate positions. Dr. Stefan Frauendorf's assistance has been invaluable in helping me understand the theory behind this work; I remain in your debt. To Dr. Anna Simon and Dr. Bruce Bunker, your willingness to become members of my committee on short notice has enabled me to complete this effort. You have my deepest thanks and gratitude.

I would like to extend thanks to Ms. Weichaun Li, Dr. Friedrich Dönau, and Dr.

Stefan Frauendorf for their excellent theoretical work. It has made a more complete interpretation and understanding of the data possible.

To Dr. Rajarshi Raut I extend my humble thanks. His patience with my many questions was genuinely appreciated. Equally appreciated was his guidance in a land that was new and different to me.

I would like to thank Dr. Robert V.F. Janssens, without his assistance, guidance, and patience in early conferences, I would have been lost.

What skills I have learned in the analysis and interpretation of gamma-ray coincidence data, I owe to Dr. Somsundar Mukhopadhyay, Dr. Shaofei Zhu, Dr. Xiaofeng Wang, and Dr. Daryl Hartley. The codes they provided and the skills they taught are a great boon to me, and I am thankful for their patience in passing them on.

I would like to deeply thank Dr. Akaa D. Ayangeakaa and Dr. Darshana Patel. They were my year-mates and friends while here. Their counsel has assisted me in maturing and their scientific discussions have enlightened. Further, their camaraderie has made for pleasant times while at Notre Dame. I thank you both from the bottom of my heart.

I would like to thank the other scientists who collaborated on the work presented in this dissertation Dr. Rudrajyoti Palit, Dr. Sudipta Saha, Dr. Jasmine Sethi, Dr. Tarkeshwar Trivedi, Dr. Sandeep S Ghugre, Dr. Ajit K Sinha, Dr. Michael P. Carpenter, Dr. Torben Lauritsen, Dr. Darek Seweryniak, Dr. Filip Kondev, Dr. Christopher J. Chiara, Ms. D. Vijaya Lakshmi, Dr. P.V. Madhusudhana Rao, Dr. M. Kumar Raju, Dr. Sujit Tandel, and Dr. Sudipta Ray. Without their support in sitting shifts and dealing with the data, this task would have been Herculean at best and impossible, more realistically.

I wish to thank the staff of the ATLAS facility and the TIFR-BARC Pelletron facility. Without their diligent troubleshooting and operation of the machines, this journey could not have started, let alone finished.

If in my haste, I have omitted anyone I offer my sincere apology. So many have been of assistance in this quest; I am profoundly moved by their generosity of spirit.

I would like to thank my parents Margaret and James. Without their anecdotes of their own time in graduate school, I would be much less sane. Without their copy editing, this document would be poorer, and rife with grammatical errors.

Last but most important, I would like to thank my fiancé Tina without her, love, understanding, and emotional support I would have fallen from this path long ago.

This work has been supported in part by the U.S. National Science Foundation [Grants No. PHY-0758100 (UND), PHY-1068192 (UND), PHY-1419765(UND), and No. PHY-1203100 (USNA)]; by the APS-IUSSTF Physics Student and Post-doc Visitation Program; by the U.S. Department of Energy, Office of Science, Office of Nuclear Physics, under Contracts No. DE-AC02-06CH11357 (ANL), No. DE-FG02-95ER40934 (UND), and No. DE-FG02-94ER40834 (UMCP); and by the Department of Science and Technology, Government of India (Grants No. IR/S2/PF-03/2003-II and No. IR/S2/PF-03/2003-III). This research used resources of ANLs ATLAS facility, which is a DOE Office of Science User Facility.

SYMBOLS

c Speed of light in vacuum

\hbar Reduced Planck Constant

$FWHM$ Full Width at Half Maximum

Z Number of protons within a nucleus

A Number of nucleons within a nucleus

$p n A$ particle nanoamps (6.24151×10^9 particles/second)

CHAPTER 1

INTRODUCTION

1.1 Rotation of Deformed Nuclei

Rotation is a universal phenomenon. It exists in the macroscopic world where objects can rotate independently about any set of axes. In the microscopic world of quantum mechanics, the situation is more complicated. Rotation about an axis of symmetry is forbidden since the wave function is unchanged. Rotation must be about an axis that is not an axis of symmetry; thus limiting it to objects that are deformed, *i.e.* not spherical.

1.1.1 Axial Deformation

Spherical nuclei are in many ways, exceptional; as Fig. 1.1 shows, deformation occurs in many regions of the nuclear chart. Near closed shells, the deformation is slight enough that spherical models can be employed to describe most nuclear properties. However, further from magic numbers, there are regions of the nuclear chart where the deformation grows large enough that it can no longer be ignored. Examples of these regions are the $A \sim 130$ region and the $A \sim 160$ region.

While axial symmetry includes both oblate (doorknob shaped) and prolate (cigar like) shapes, there are few oblate nuclei. The majority have prolate deformation. This is usually understood as an effect of single particle structure from the Nilsson model (the Nilsson model is discussed in more detail in Chapter 2). Overall, prolate deformation moves more orbitals to low energy than oblate deformation. Therefore

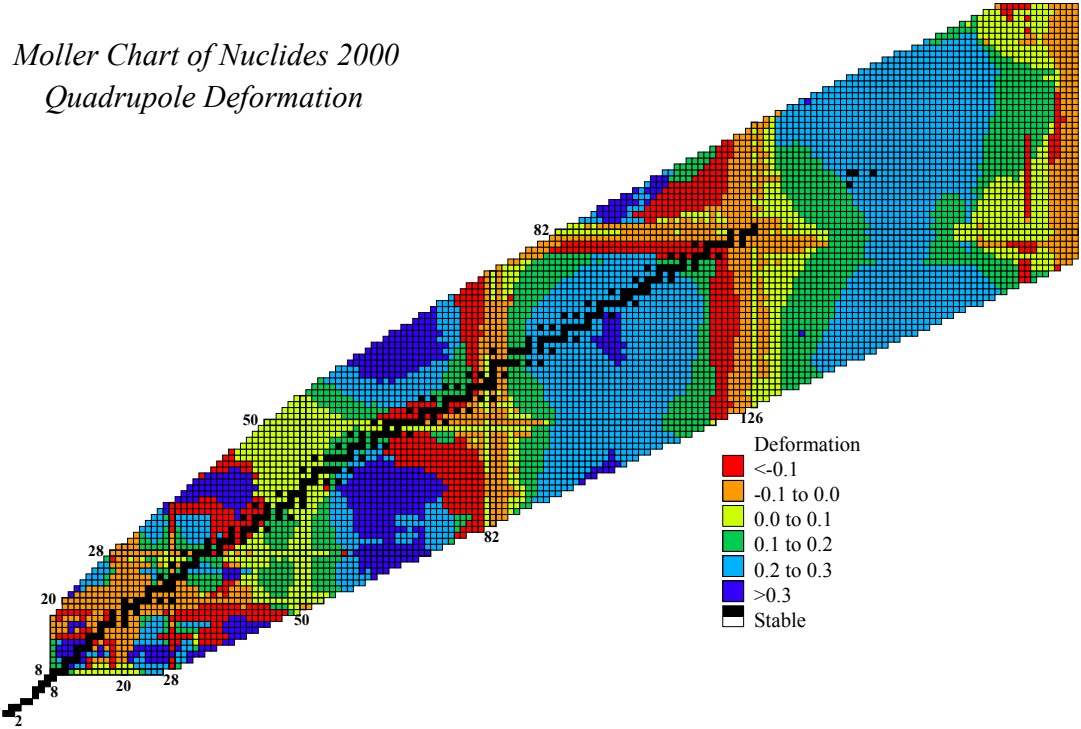


Figure 1.1. Quadrupole deformation parameter β_2 across the nuclear chart.
Plot adapted from [93] which used data from [76].

in situations where there are several particles, a sum over these particles will favor prolate shapes.

1.1.2 Triaxiality

Nuclear triaxiality has been a subject of interest for years. While most deformed nuclei are axial in their shape, triaxial shapes have been predicted at low to moderate spin for a few regions of the nuclear chart, *e.g.* $Z \sim 60$, $N \sim 76$ and $Z \sim 46$, $N \sim 66$ [77]. Triaxial shapes also occur in the $Z \sim 70$, $N \sim 90$ region, but are found in triaxial superdeformed bands at high spins. In searching for triaxiality we are aided by the existence of two unique fingerprints, chirality and wobbling; phenomena that cannot exist unless the nuclear shape is triaxial. Thus observation of either of these modes

is important as they constitute irrefutable evidence of triaxiality.

1.1.2.1 Chirality

First predicted in 1997 by S. Frauendorf and J. Meng, chirality occurs when the axis of rotation lies outside the plains spanned by the principal axes of the nucleus [34, 38, 42]. Here a particle-like quasiparticle couples to the short axis, a hole-like quasi-particle couples to the long axis, and the triaxial rotor core rotates about the intermediate axis. In this configuration the total angular momentum points away from any of the principal planes of the nucleus and the three components of the angular momentum form a screw with respect to the total [42]. When this configuration is present, the time-reversal symmetry of the nuclear wave function is broken and two nearly degenerate $\Delta I = 1$ bands with similar electromagnetic properties emerge. Experiments have confirmed the existence of pairs of chiral bands in the $A \sim 190$, $A \sim 130$, $A \sim 100$, and $A \sim 80$ regions of the chart of the isotopes; an example from each mass region can be found in Refs. [6, 115, 116, 123]

1.1.2.2 Wobbling

Of the two fingerprints of nuclear triaxiality, nuclear wobbling was perhaps the longest anticipated. First predicted by A. Bohr and B. Mottelson in Ref. [16], wobbling was not observed until the work in 2001 by Ødegård *et al.* [84]. Later four more wobbling nuclei were discovered, expanding the list to $^{161,163,165,167}\text{Lu}$ and ^{167}Ta [1, 23, 54, 60, 84, 102]. The wobbling mode is the quantum mechanical analog of the spinning motion of an asymmetric top. In the high spin limit the wobbling mode is a harmonic vibration describing oscillation of a principal axis of the nucleus about the angular momentum vector.

Understanding of the wobbling mode in nuclei has evolved quickly over the last 15 years. Bohr and Mottelson first showed that a rotating nucleus with stable triaxial

deformation could have its rotational angular momentum precess and nutate about the principal axis of a nucleus [16] (in analogy to the classical asymmetric top) quite some time ago. In 1995, Schnack-Petersen *et al.* suggested that bands in $^{163,165}\text{Lu}$ which are based on the $\pi(i_{13/2})$ configuration, occupied a triaxial superdeformed (TSD) minimum of the total Routhian surface [101]. Following this there was a rush of wobbling discoveries in $^{161,163,165,167}\text{Lu}$ from 2001 to 2005 [1, 23, 60, 84, 102]. Further searches conducted in the region on ^{171}Ta [52], ^{169}Ta [53], ^{163}Tm [89], $^{171,172}\text{Hf}$ [122], and $^{160,161}\text{Tm}$ [113] yielded no further wobbling bands. This left an open problem as to why wobbling was only appearing in the Lu isotopes.

A possible solution to this problem was offered up in the Tilted Axis Cranking calculations by Frauendorf, presented in Ref. [89]. The calculations suggest that the Lu TSD minima have a low density of states; low enough that the relatively high excitation energy wobbling mode can be observed. Contrariwise, the TSD minima of other nuclei in the region had a high density of states which could produce many different TSD bands with alternate configurations at similar energies. Thus, it is not that wobbling is absent in nuclei that are not Lu isotopes, but instead, that outside of the Lu isotopes there was a competition between wobbling and particle hole excitations that favored the latter. This result motivated a search of ^{167}Ta for wobbling which in 2009 yielded the first wobbling band outside the Lu isotopes [54].

1.1.2.3 Triaxiality in the $A \sim 130$ Region

As previously stated Ref. [77] predicts the region around $Z \sim 60$ and $N \sim 76$ to have triaxial shapes at low to moderate spin. The prevalence of triaxial shapes in this region is confirmed by the numerous observations of chirality [5, 51, 55, 64, 79, 91, 108, 123]. Additionally, a more exotic and stable chirality was identified in [79, 123] and confirmed via lifetime measurement to extract the $B(M1)$ and $B(E2)$ values of the partner bands to ensure that they are the same [79]. In fact, in this

case, a transition from the more usual chiral vibration (where the angular momentum vector oscillates in a plane perpendicular to the axes the quasiparticles are coupled to) to static chirality where this oscillation slows to nearly stationary resulting in the bands becoming quite close to degenerate.

With this demonstration that triaxiality is rampant in the $A \sim 130$ region, it becomes logical to set one's sights on that as the next region to search for wobbling.

1.2 Previous Cases of Wobbling

The wobbling bands of the previously known wobblers are pictured in Figs. 1.2, 1.3, and 1.4). These figures are in chronological order of discovery from left to right, top to bottom.

Following the discovery of the first wobbling structure, calculations using the QTR model were used to describe the wobbling mode [48, 49, 110, 111]. Later, microscopic random phase approximation (RPA) calculations [70, 71, 85, 104, 105] were used as well. Both theories do well in reproducing the large $B(E2)_{out}/B(E2)_{in}$ interband to intraband ratios seen in experiment. However, the QTR model, using the assumption that the odd quasiparticle aligns with the intermediate axis [48, 49, 110, 111], fails to reproduce the experimentally observed decrease in the wobbling energy (see Fig. 1.5) which is defined by:

$$\Delta E = \hbar\omega_w(I) = E(I, n_w = 1) - (E(I - 1, n = 0) + E(I + 1, n_w = 0))/2 \quad (1.1)$$

In contrast the microscopic RPA calculations were able to reproduce the observed decrease in wobbling energy.

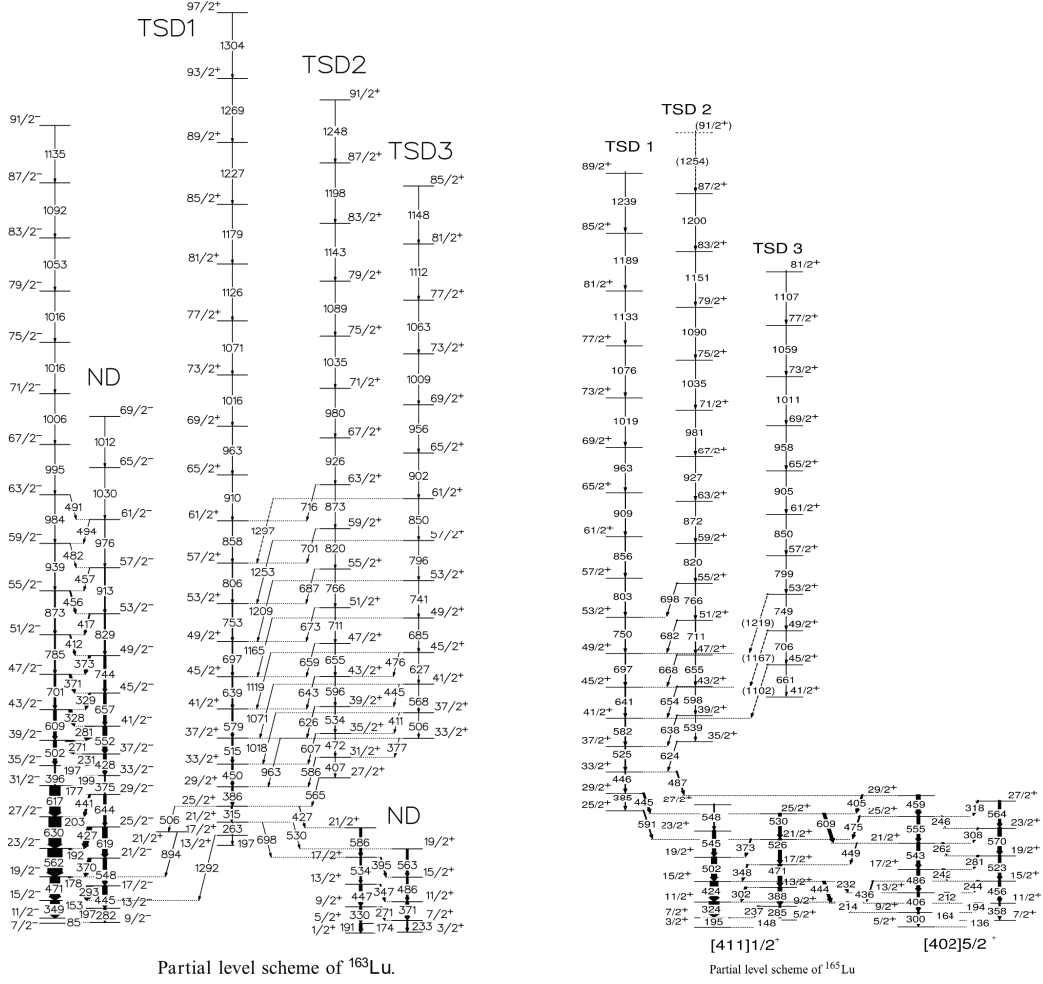


Figure 1.2. Partial level schemes of ^{163}Lu (left) and ^{165}Lu (right). Figures adapted from Ref. [60] and Ref. [102], respectively. In ^{163}Lu the $n_w = 0, 1, 2$ bands are labeled TSD1, TSD2, and TSD3, respectively. In ^{165}Lu the $n_w = 0, 1, 2$ bands are labeled TSD1, TSD2, and TSD3, respectively.

1.3 Motivation

To correct the deficiency in the QTR calculations of wobbling, S. Frauendorf and F. Dönau introduced the concept of transverse and longitudinal wobbling [41]. In this new scheme Refs. [48, 49, 110, 111] were describing longitudinal wobbling which is expected to have an increasing wobbling frequency. A semi-classical analysis of transverse wobbling, which has the quasiparticle couple to an axis perpendicular to the

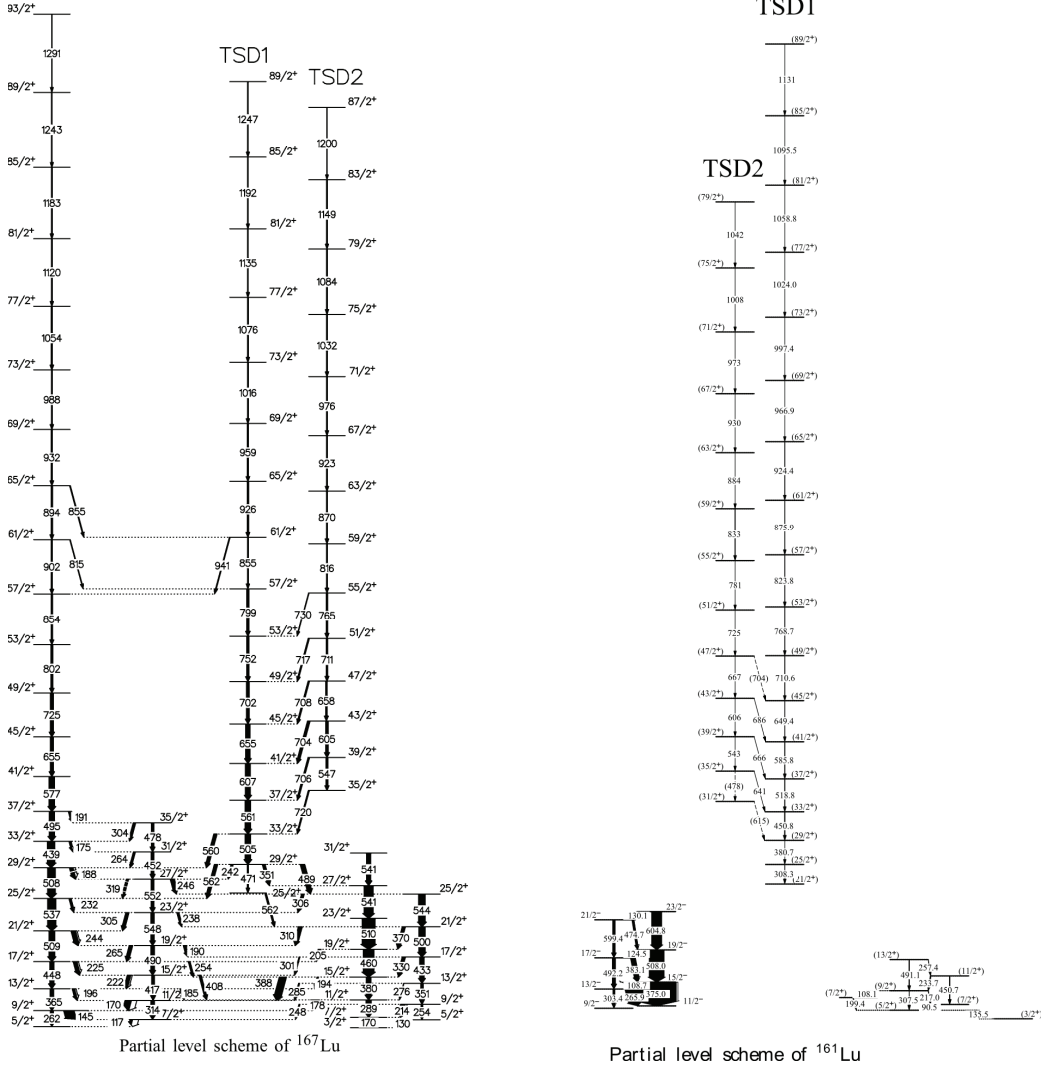


Figure 1.3. Partial level schemes of ^{167}Lu (left) and ^{161}Lu (right). Figures adapted from Ref. [1] and Ref. [23], respectively. In ^{167}Lu the $n_w = 0, 1$ bands are labeled TSD1 and TSD2, respectively. In ^{161}Lu the $n_w = 0, 1$ bands are labeled TSD1 and TSD2, respectively.

intermediate axis, shows that the modified mode exhibits a decreasing wobbling frequency as has been seen in experimental observations of wobbling while reproducing the interband to intraband $B(E2)$ ratios.

The work presented in this dissertation was performed to test the theory of transverse wobbling and show that the $A \sim 130$ region is a viable place to search for

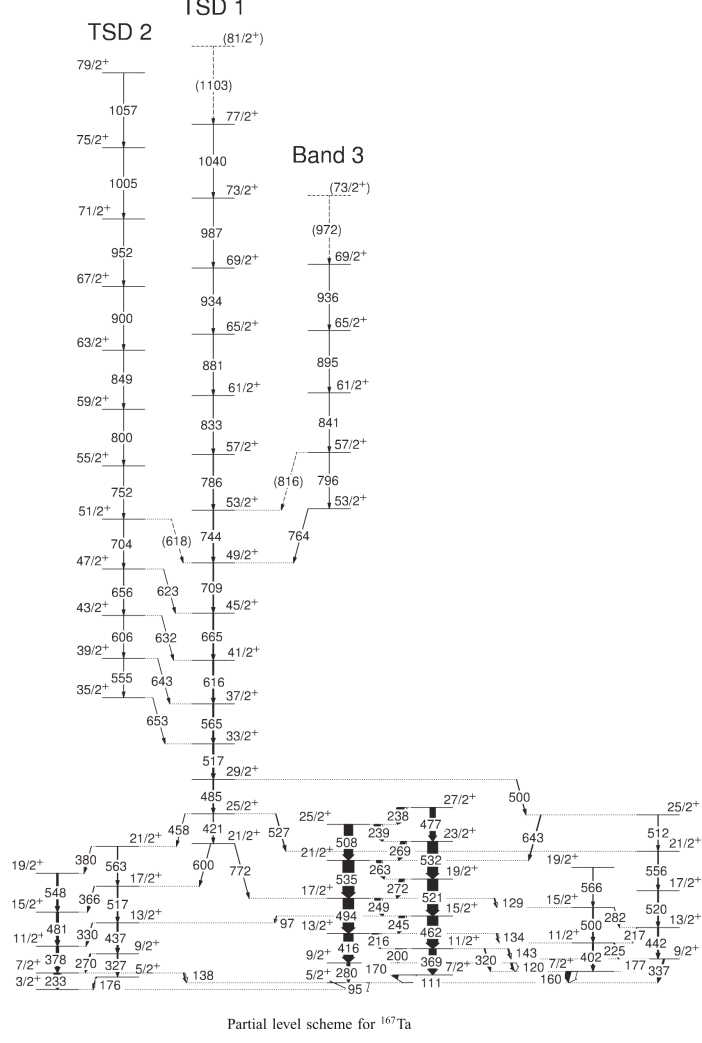


Figure 1.4. Partial level scheme of ^{167}Ta . Figure adapted from Ref. [54].
The $n_w = 0, 1$ bands are labeled TSD1 and TSD2, respectively.

the wobbling modes in nuclei. Toward that end, a suspected transverse wobbling was measured in ^{135}Pr and its transverse wobbling nature was confirmed by showing that interband $n_w = 1 \rightarrow n_w = 0$ transitions had $\Delta I = 1, E2$ nature using angular distribution and polarization asymmetry measurements. Finally, theoretical work in the framework of the QTR and TAC models was performed; thus confirming that the wobbling mode is well described by the QTR framework.

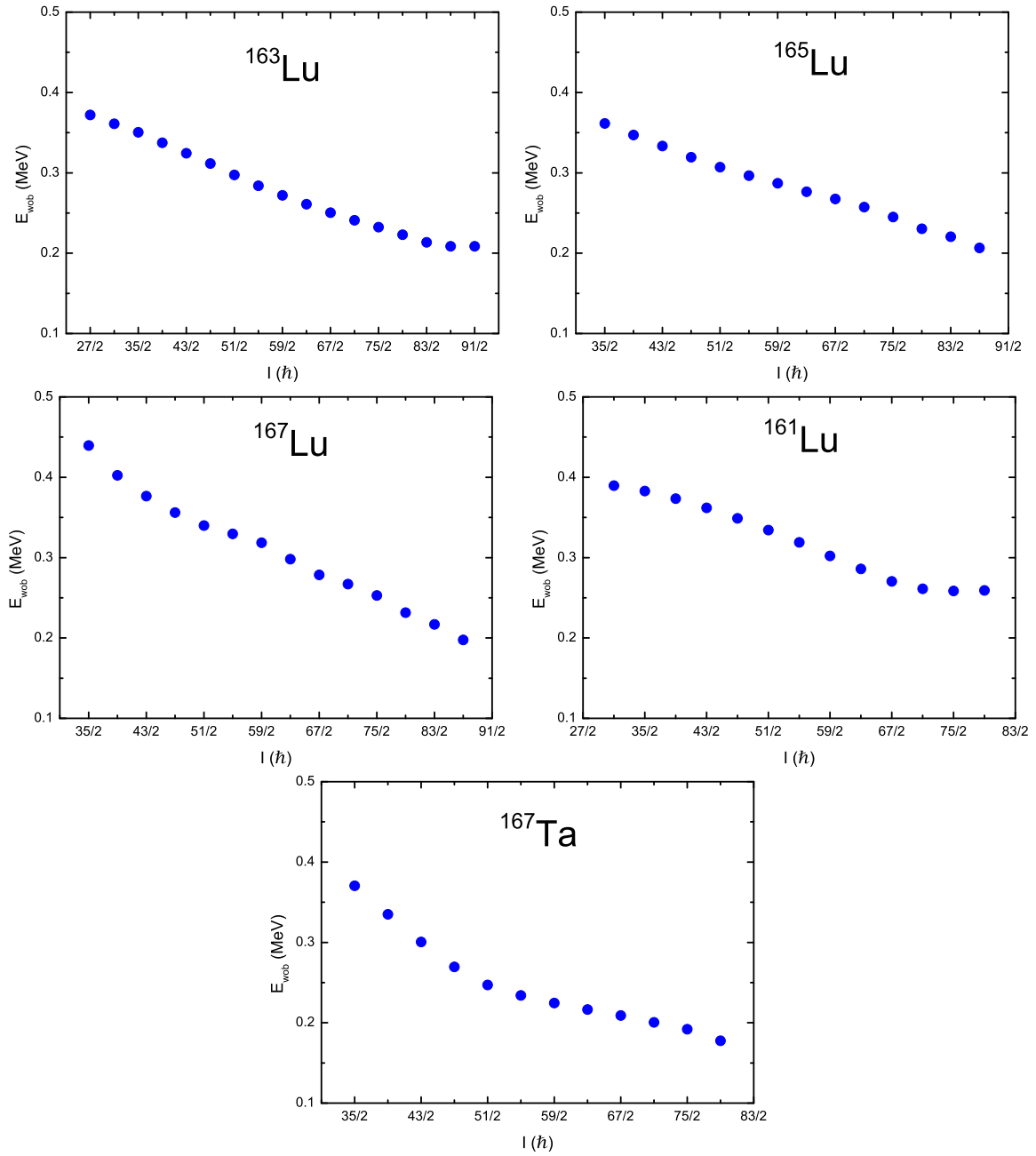


Figure 1.5. Wobbling frequencies of the $A \sim 170$ wobblers. Top Left: ^{163}Lu . Top Right: ^{165}Lu . Middle Left: ^{167}Lu . Middle Right: ^{161}Lu . Bottom: ^{167}Ta .

CHAPTER 2

NUCLEAR MODELS FOR HIGH SPIN PHENOMENA

2.1 Introduction

The atomic nucleus, discovered in 1911 by Ernest Rutherford [100], is a tiny concentration of matter at the heart of an atom. The nucleus is approximately $1 - 10$ fm across, contains more than 99.94% of an atom's mass, and is composed of protons and neutrons (collectively called nucleons). The force between nucleons is a powerful short range force that overcomes the Coulomb repulsion to produce a bound system. The range of this force is quite limited, to perhaps nearest neighbors only, as can be seen in the saturation of binding energy per nucleon around $A \sim 60$ at a value close to 8.5MeV.

Examination of the two proton and two neutron separation energies (Fig. 2.2) shows several distinct discontinuities at specific numbers of protons or neutrons. Further examination of the energies of the first 2^+ (Fig. 2.3) states shows peaks at the same numbers. These “magic numbers” occur at numbers of protons and neutrons where there is a dramatic drop off in the nucleon separation energy with the addition of another nucleon. Further evidence for magic numbers of protons and neutrons can be found in the increase first excited state energies located at these magic numbers, substantially decreased neutron absorption cross-sections at neutron magic numbers, and in the enhanced abundance of nuclides where N and Z are magic numbers. The magic numbers are 2, 8, 20, 28, 50, 82, and 126, with 40 and 64 also weakly magic over certain ranges of N and Z.

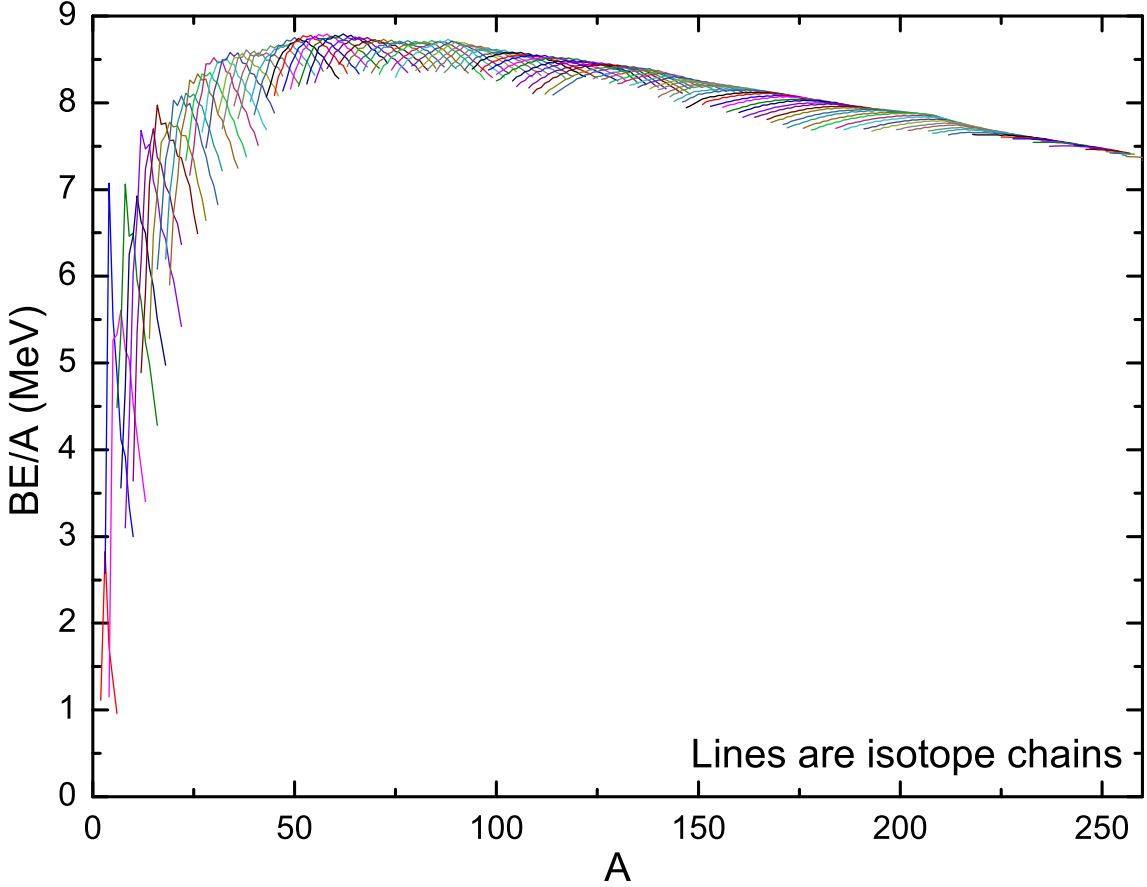


Figure 2.1. Binding energies per nucleon plotted versus mass number.
Values calculated from Ref. [3, 118].

Analogy to atomic theory shows these magic numbers are major shell closures. This leads to the conclusion that the nucleus has shell structure, leading to the shell model of the nucleus. These numbers can be derived from the calculation of a single particle in a mean field potential. Far from stability, quenching of the known shell gaps and the opening of new shell gaps has been observed [59].

The nucleus also exhibits collective excitations such as rotation and vibration which are described later in the chapter. The crucial differences between an atomic system and the nuclear system are as follows: First, the atom has a nucleus whose Coulomb field guides the electron cloud, preventing collective motions. Second, the

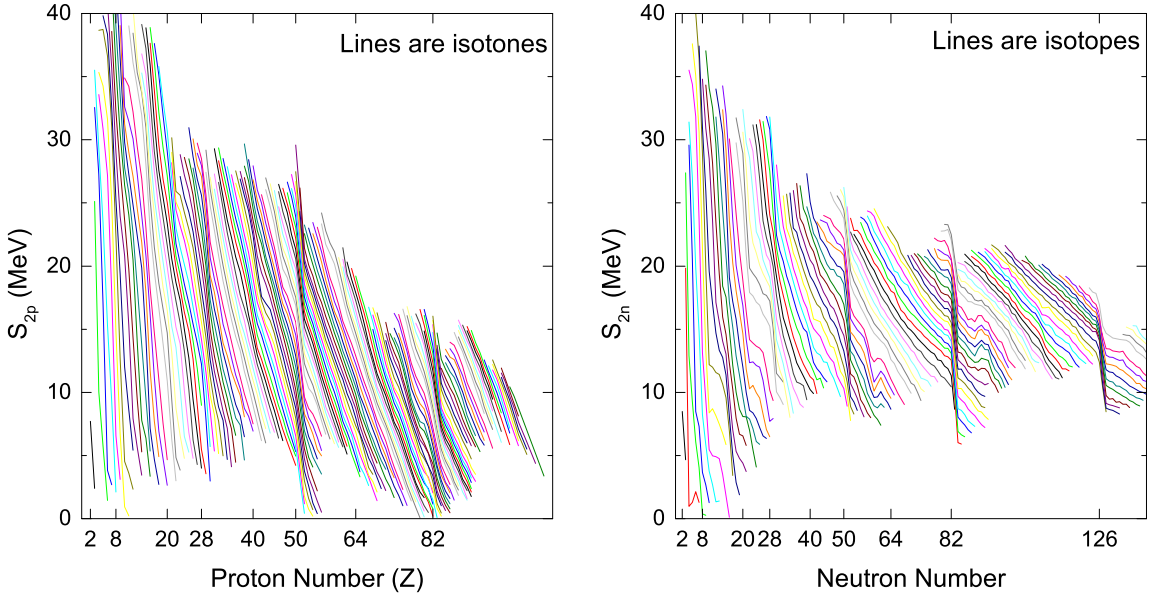


Figure 2.2. Left: Two proton separation energies plotted versus proton number. Each line is a set of isotones. Right: Two neutron separation energies plotted versus neutron number. Each line is a set of isotopes.

Values calculated from Ref. [3, 118].

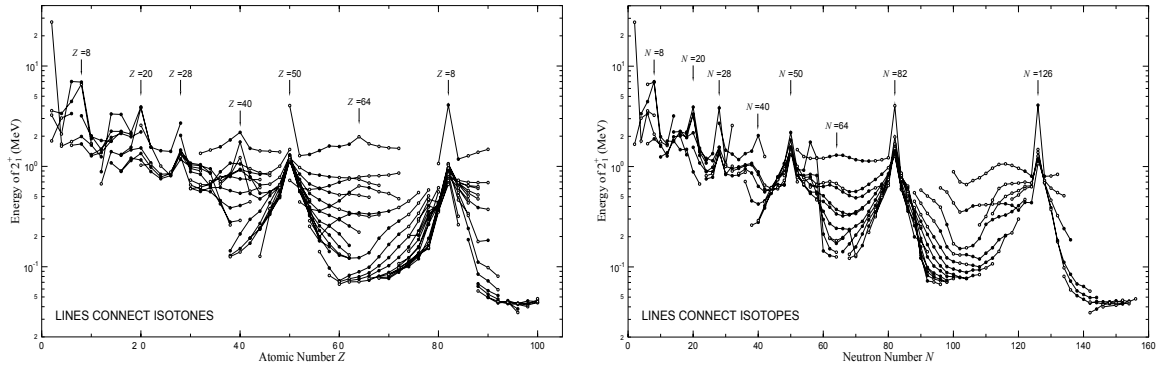


Figure 2.3. Left: First excited 2^+ energies of nuclei with even Z and N , plotted versus proton number. Each line is a set of isotones. Right: First excited 2^+ energies of nuclei with even Z and N , plotted versus neutron number. Each line is a set of isotopes. Figures adapted from Ref. [97].

nucleus has two types of particles, protons and neutrons, occupying its shells.. With this, certain shell occupations can lead to the “single particle behavior” exhibited around closed shells, while different occupations can yield collective phenomena.

2.2 The Shell Model

The nuclear shell model, in its simplest form, seeks to explain the shell structure observed in nuclei by describing the nucleons as independent particles in the mean field potential produced by the other nucleons. While the short range nature of the nuclear force might lead to the use of a square well potential or similar as the mean field, the Simple Harmonic Oscillator (SHO) potential is a reasonable first order approximation (seen in Figure 2.4), which happens to be much simpler to solve. Placing a single particle in the SHO potential gives the first few magic numbers observed; however, to reproduce all the magic numbers it is necessary to add an \vec{l}^2 potential and a strong spin-orbit ($(\vec{l} \cdot \vec{s})$) potential. The Hamiltonian for such a potential, called the modified oscillator potential, is as follows:

$$H = \frac{-\hbar^2}{2m} \nabla^2 + \frac{1}{2} m(\omega r)^2 + B \hat{\mathbf{l}}^2 + A \hat{\mathbf{l}} \cdot \hat{\mathbf{s}} \quad (2.1)$$

The progression of shell gaps from *SHO* to *SHO + \vec{l}^2* to *SHO + $\hat{\mathbf{l}}^2 + \hat{\mathbf{l}} \cdot \hat{\mathbf{s}}$* is shown in Figure 2.5.

In more realistic shell model calculations a Woods-Saxon potential is adopted. Here the Hamiltonian becomes:

$$H = \frac{-\hbar^2}{2m} \nabla^2 + \frac{V}{1 + e^{(r-R)/a}} - \alpha(r) \hat{\mathbf{l}} \cdot \hat{\mathbf{s}} \quad (2.2)$$

where $R = r_0 A^{1/3}$, $r_0 \sim 1.2\text{fm}$, $a \sim 0.5\text{fm}$, and $V \sim 50\text{MeV}$. In addition to the central term, a spin orbit term is necessary to reproduce the observed shell gaps. The

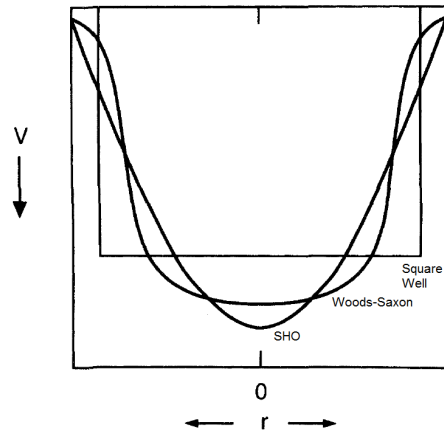


Figure 2.4. Schematic of a square well, SHO potential, and a realistic Woods-Saxon potential. Figure adapted from Ref. [26].

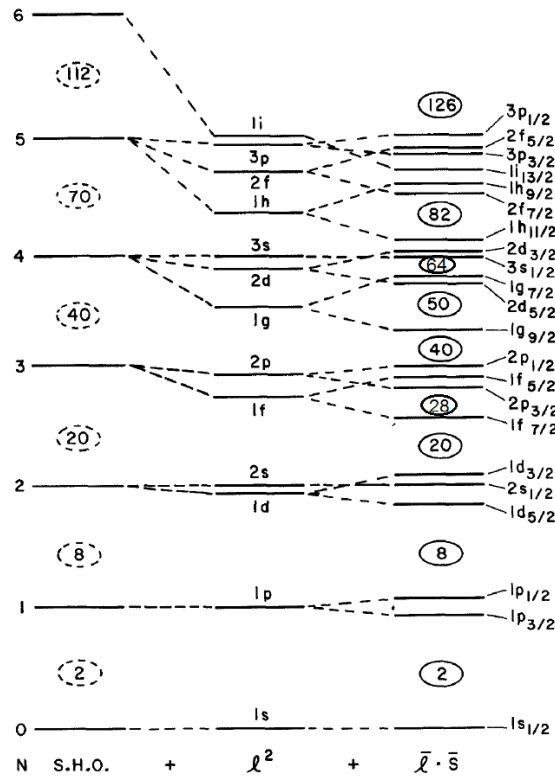


Figure 2.5. Spectrum of a single nucleon in an SHO potential, SHO + l^2 , and, SHO + l^2 + spin-orbit. Figure adapted from Ref. [26].

central flatness of the Woods-Saxon potential reflects the saturation of the nuclear force better than an SHO potential. This increased realism comes at the cost of increased difficulty in calculations—with this Hamiltonian the Schrödinger equation is no longer analytically solvable and must instead be solved with numerical methods.

Up to now in this chapter, the nucleons were considered as independent particles within a mean field which was the average potential produced by the other particles. This description, while powerful, is not accurate, especially for nuclei away from the closed shells. The missing piece is the interactions between nuclei that are not accounted for in the mean field, often called “residual interactions.” Residual interactions must be accounted for to produce an accurate description of the nucleus.

2.3 The Deformed Shell Model

2.3.1 Parameterization of Deformation

In the standard shell model the potentials are spherically symmetric, depending only on the radius. While this is a successful approach near the shell gaps where nuclei are spherical, or nearly spherical, it breaks down in the deformed regions farther from shell closures. In such nuclei, the long-range correlations experienced by the valence nucleons can lead to deformation as the valence nucleons are arranged into deformed shells with lower energy levels. When the nuclear shape is deformed the surface of the nucleus is described with a parametric function defining the radius as follows:

$$R(\theta, \phi) = R_0 \left(1 + \sum_{\lambda=2}^{\infty} \sum_{\mu=-\lambda}^{\lambda} \alpha_{\lambda\mu} Y_{\lambda\mu}(\theta, \phi) \right) \quad (2.3)$$

Here R_0 is the radius of a sphere with the same volume as the deformed nucleus, $Y_{\lambda\mu}(\theta, \phi)$ are the spherical harmonic functions, and $\alpha_{\lambda\mu}$ are the coefficients of the expansion. The expansion starts at $\lambda = 2$ because the $\lambda = 1$ corresponds to the translation of the center of mass, a term easily eliminated by requiring the nuclear

center of mass to coincide with the coordinate's origin. The first of the non-trivial terms, $\lambda = 2$, corresponds to the components of quadrupole deformation, $\lambda = 3$ gives octupole deformation, $\lambda = 4$ gives hexadecapole deformation, and so on. As $\lambda = 2$ is the most important component in this work, only quadrupole deformation terms will be considered henceforth.

The quadrupole shapes cover oblate spheroids (two semi-major axes, like a door-knob), prolate spheroids (two semi-minor axes, like an American football), and triaxial ellipsoids (all three axes are different lengths, like a potato). Because the rotation of the nucleus is not fixed, *i.e.* the nucleus can be rotated such that its principal axes coincide with the axes of the coordinate system, the five quadrupole shape parameters are reduced to two independent parameters a_{20} and a_{22} , with the conditions: $a_{2-2} = a_{22}$ and $a_{21} = a_{2-1} = 0$. Further, it is common to parameterize the remaining expansion coefficients using the Hill-Wheeler variables, β and γ , as follows [120]:

$$a_{20} = \beta \cos(\gamma) \quad a_{22} = a_{2-2} = \frac{1}{\sqrt{2}} \beta \sin(\gamma) \quad (2.4)$$

Expanding the spherical harmonics as:

$$Y_{20}(\theta, \phi) = \frac{1}{4} \sqrt{\frac{5}{\pi}} (-1 + 3 \cos(\theta)^2) \quad (2.5)$$

$$Y_{22}(\theta, \phi) = \frac{1}{4} e^{2i\phi} \sqrt{\frac{15}{2\pi}} \sin(\theta)^2 \quad (2.6)$$

$$Y_{2-2}(\theta, \phi) = \frac{1}{4} e^{-2i\phi} \sqrt{\frac{15}{2\pi}} \sin(\theta)^2 \quad (2.7)$$

and inserting all this into Equation 2.3 yields:

$$R(\theta, \phi) = R_o \left(1 + \sqrt{\frac{5}{16\pi}} \beta \left(\cos(\gamma) (3 \cos(\theta)^2 - 1) + \sqrt{3} \sin(\gamma) \sin(\theta)^2 \cos(2\phi) \right) \right) \quad (2.8)$$

The Hiller-Wheeler variables have some redundancy: for $\beta > 0$ the nucleus is prolate

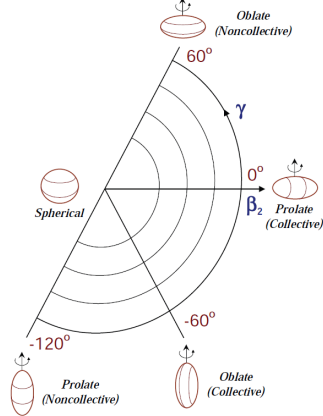


Figure 2.6. Schematic of the Lund convention. Figure adapted from Ref. [4].

for $\gamma = 0^\circ, 120^\circ, 240^\circ$ and oblate for $\gamma = 180^\circ, 300^\circ, 60^\circ$. However, for $\gamma = 0^\circ$ and $\gamma = 180^\circ$ the symmetry axis is the \hat{z} -axis of the intrinsic frame, for $\gamma = 120^\circ$ and $\gamma = 300^\circ$ the symmetry axis is the \hat{x} -axis, and for $\gamma = 240^\circ$, and $\gamma = 60^\circ$ the symmetry axis is the \hat{y} -axis. The Lund convention makes use of this redundancy by selecting a rotational axis according to the following rules [120]:

1. $\beta \geq 0$
2. For rotation about the smallest axis $0^\circ \leq \gamma \leq 60^\circ$
3. For rotation about the longest axis $-120^\circ \leq \gamma \leq -60^\circ$
4. For rotation about the intermediate axis $-60^\circ \leq \gamma \leq 0^\circ$

A graphical schematic of the Lund convention is in Figure 2.6

2.3.2 The Nilsson Model

In 1955, to treat deformed nuclei, S.G. Nilsson introduced a modified version of the shell model in Ref. [82]. This modified shell model, known as the Nilsson model, allows deformation to be taken into account using an anisotropic harmonic oscillator

potential as follows:

$$H_{nil} = -\frac{\hbar^2}{2m}\nabla^2 + \frac{m}{2}(\omega_x^2x^2 + \omega_y^2y^2 + \omega_z^2z^2) + 2\kappa\hbar\omega_o[\vec{l} \cdot \vec{s} - \mu(l^2 - \langle l^2 \rangle_N)] \quad (2.9)$$

Here $\omega_{x,y,z}$ are the oscillator frequencies in each of the three dimensions, κ controls the strength of the spin orbit part of the potential, and μ controls the strength of the correction term. The correction term, $l^2 - \langle l^2 \rangle_N$, originally had the form of μl^2 [82]. It served the purpose of suppressing the energy of the higher lying shells; however, it was noted in Ref. [47] that this shift was too large for large N quantum numbers. Thus the correction term was modified to its current form to compensate. The three oscillator frequencies are chosen to be inversely proportional to the axis lengths of the ellipsoid a_x , a_y , and a_z as follows:

$$\omega_i = \omega_0 \frac{R_0}{a_i} \quad i = x, y, z \quad (2.10)$$

Here ω_0 is the oscillator frequency for the spherical case, defined as $\hbar\omega_0 = (\omega_x\omega_y\omega_z)^{1/3}$.

In the case of axial symmetry the oscillator frequencies are defined in terms of the deformation parameter ϵ_2 as follows.

$$\omega_x = \omega_y = \omega_{\perp} = \omega(\epsilon_2) \left(1 + \frac{1}{3}\epsilon_2\right) \quad (2.11)$$

$$\omega_z = \omega_{\parallel} = \omega(\epsilon_2) \left(1 - \frac{1}{3}\epsilon_2\right) \quad (2.12)$$

$$\omega(\epsilon_2) = \omega_0 \left(1 - \frac{1}{3}\epsilon_2^2 - \frac{2}{27}\epsilon_2^3\right)^{-1/6} \quad (2.13)$$

Here the deformation β is defined with respect to ϵ_2 using the following series:

$$\beta = \sqrt{\frac{16\pi}{5}} \left(\frac{1}{3}\epsilon_2 + \frac{1}{9}\epsilon_2^2 + \frac{1}{27}\epsilon_2^3 + \frac{1}{81}\epsilon_2^4 \dots \right) \quad (2.14)$$

With these definitions and the Nilsson Hamiltonian, the energy eigenstates ($\epsilon_{\Omega[Nn_z\Lambda]}$),

sometimes called Nilsson orbitals, can be extracted from solving the Schrödinger equation.

$$H_{nil}\psi_i = \epsilon_i\psi_i \quad (2.15)$$

Here i represents the complete set of asymptotic quantum numbers used to specify Nilsson orbitals:

$$\Omega^\pi[Nn_z\Lambda] \quad (2.16)$$

Ω is projection of the particle's total angular momentum onto the symmetry axis, π is the parity defined as $\pi = (-1)^l = (-1)^N$, N is the oscillator quantum number, n_z is the number of oscillator quanta (number of nodes in the wave function), and Λ is the projection of the particle's orbital angular momentum onto the symmetry axis. Some of these quantum numbers are shown schematically in Fig. 2.7.

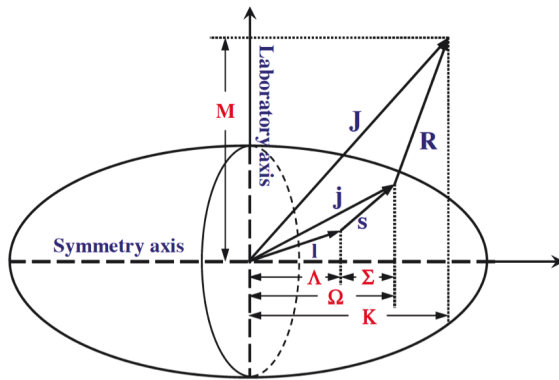


Figure 2.7. Schematic of an axially symmetric nucleus and the various quantum numbers that are used in the description of the system. Here R is the angular momentum of collective rotation, J is the total nuclear angular momentum, j is the total angular momentum of the particle, l is the orbital angular momentum of the particle, s is the spin of the particle, M is the projection of J onto the non-symmetry axis, K is the projection of J onto the symmetry axis, Ω is the projection of j onto the symmetry axis, Λ is the projection of l onto the symmetry axis, and Σ is the projection of s onto the symmetry axis. Figure adapted from Ref. [4].

The deformation dependence of Nilsson orbitals is usually summarized in a Nilsson diagram. In these diagrams energy levels for various sets of asymptotic quantum numbers are plotted versus the deformation parameter ϵ . A Nilsson diagram for protons in the $40 \leq Z \leq 82$ region is shown in Fig. 2.8. A diagram for neutrons in the $40 \leq Z \leq 82$ region is shown in Fig. 2.9. Together these diagrams cover the $A \sim 130$ region where ^{135}Pr lies.

2.4 Collective Rotation

A model of collective nuclear motion was developed by Bohr and Mottleson [16, 17] due to several observations that could not be explained with single particle motion. Among these are: 1. Fission, many of the features are successfully explained with the liquid drop model [20, 74]. 2. Deformation of the nuclear surface by particle structure [96] giving rise to quadrupole moments which exceed single particle estimates in many nuclei [25, 114]. 3. The occurrence of electric quadrupole gamma ray transitions with lifetimes much shorter than single particle estimates [45] which is a characteristic feature of the excitation spectra of strong deformed nuclei and most importantly: rotational bands [15].

2.4.1 Rigid Triaxial Rotor Model (TRM)

One of the simplest forms of excitation a nucleus can experience is rotation. However, in quantum mechanics rotation can only occur about axes that are not symmetry axes (where the symmetry axis is denoted the $\hat{\mathbf{z}}$ -axis). This is because the wave function that describes this system is an eigenfunction of $\hat{\mathbf{J}}_z$, and thus, is symmetrical about the $\hat{\mathbf{z}}$ -axis. Due to this symmetry any rotation of this wave function about the symmetry axis generates only phase shift and has a wave function identical to that of the ground state. A system cannot collectively rotate about symmetry axes. Since spherical nuclei are symmetric about all axes, they cannot

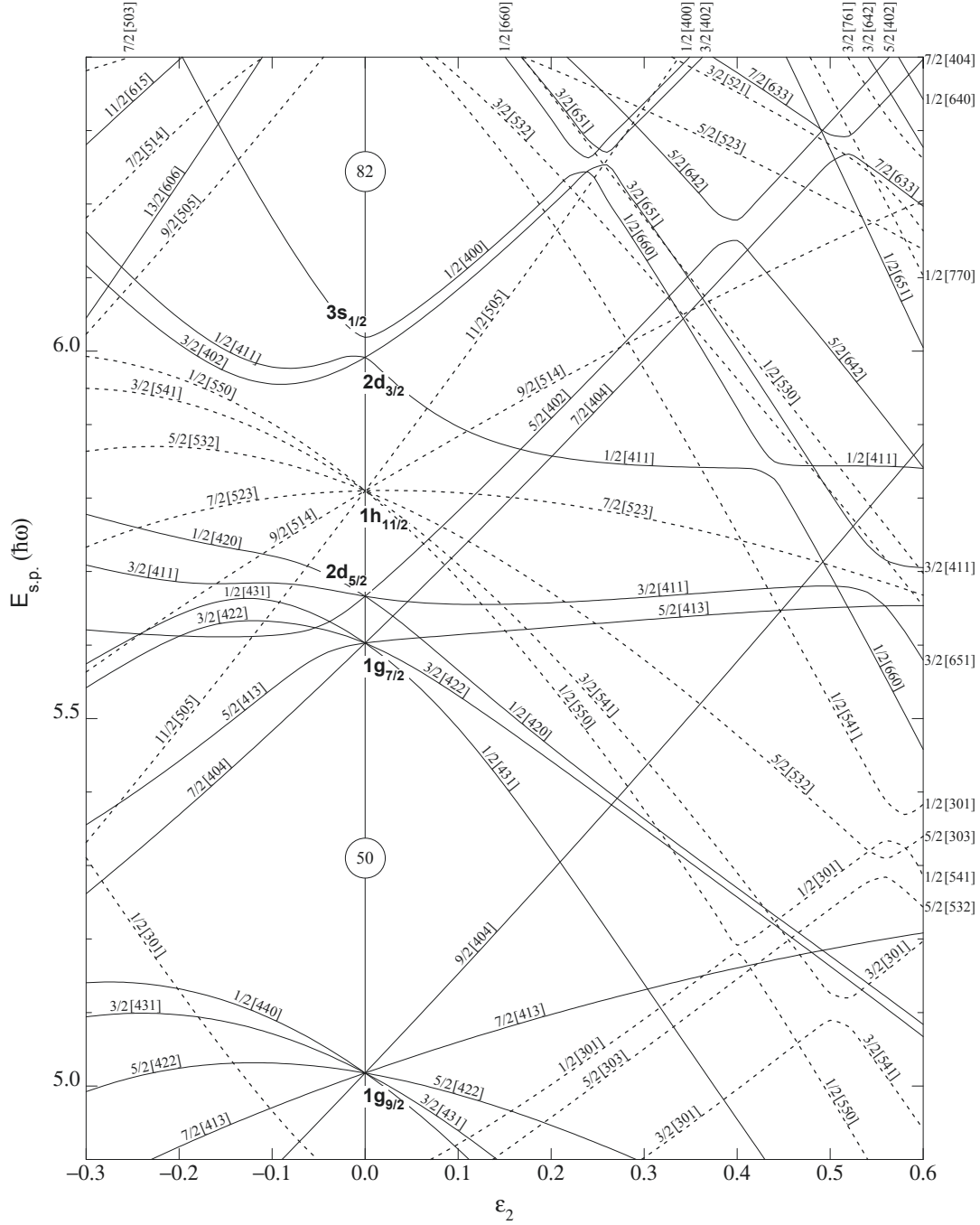


Figure 11. Nilsson diagram for protons, $50 \leq Z \leq 82$ ($\varepsilon_4 = \varepsilon_2^2/6$).

Figure 2.8. Nilsson diagram for protons in the $50 \leq Z \leq 82$ region with $\epsilon_4 = \epsilon_2/6$. Solid lines represent positive parity orbitals and dashed lines represent negative parity orbitals. Labels follow the $\Omega[N\ n_z\ \Lambda]$ convention.

Figure adapted from Ref. [93].

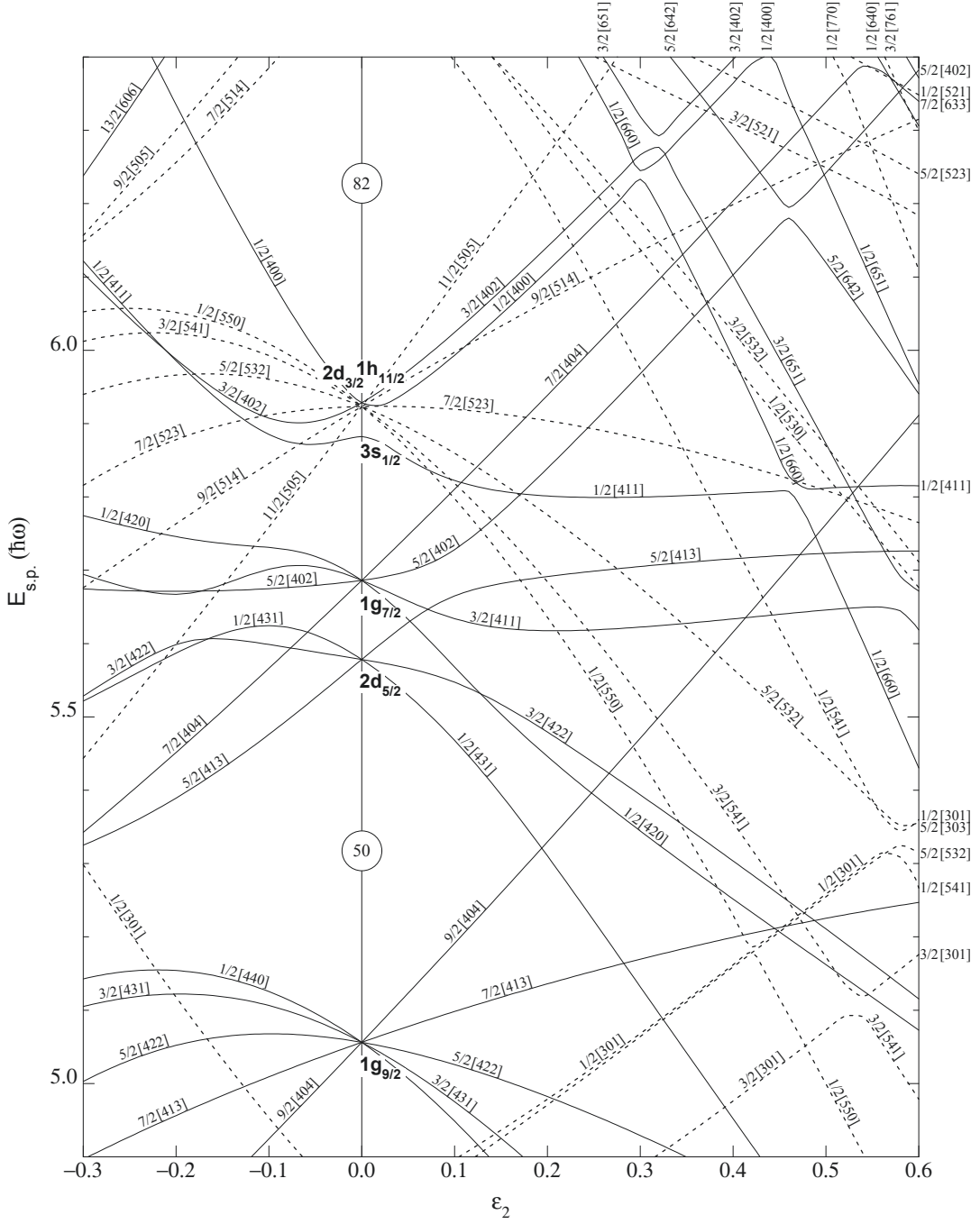


Figure 5. Nilsson diagram for neutrons, $50 \leq N \leq 82$ ($\epsilon_4 = \epsilon_2^2/6$).

Figure 2.9. Nilsson diagram for neutrons in the $50 \leq N \leq 82$ region with $\epsilon_4 = \epsilon_2/6$. Solid lines represent positive parity orbitals and dashed lines represent negative parity orbitals. Labels follow the $\Omega[N\ n_z\ \Lambda]$ convention.

Figure adapted from Ref. [93].

exhibit collective rotation.

In rotating nuclei there are two primary components of the angular momentum. The first is the rotational angular momentum, \vec{R} , generated by the collective motion of many nucleons about some axis. The second component is found when there are unpaired valence nucleons. In these cases their angular momentum, \vec{j} , must be accounted for as well. This presents a situation like that in Figure 2.7 which schematically illustrates the total angular momentum of the nucleus, \vec{J} , as the sum of \vec{R} and \vec{j} .

While it is often the case that the shape (and thus the moments of inertia (MOI)) of a nucleus changes somewhat as spin increases. By approximating the system as a rigid rotor with unchanging MOI the problem can be simplified while maintaining descriptive power. Here each axis has a fixed MOI and the rotational component of the Hamiltonian depends only on the MOIs and the components of the spin along each axis. In the case of a triaxial nucleus with no unpaired valence particles, (thus $\vec{J} = \vec{R}$) the Hamiltonian can be written as follows [32, 119]:

$$H = H_{rot} + H_{intr} \quad (2.17)$$

$$H_{rot} = A_3 \hat{\mathbf{J}}_3^2 + A_1 \hat{\mathbf{J}}_1^2 + A_2 \hat{\mathbf{J}}_2^2 \quad (2.18)$$

Here H_{intr} is the intrinsic component of the Hamiltonian accounting for the internal state of the nucleus, $A_i = \frac{\hbar^2}{2\mathcal{J}_i}$ where \mathcal{J}_i is the MOI of rotation about the i^{th} axis, and $\hat{\mathbf{J}}_i$ is the operator for the component of the angular momentum along the i^{th} axis. Rewriting the rotational Hamiltonian to a form that uses the operators $\hat{\mathbf{J}}^2$, $\hat{\mathbf{J}}_3^2$, and

$\hat{\mathbf{J}}_{\pm}^2$ yields:

$$\begin{aligned} H_{rot} &= H_r^{Diag} + H_r^{OffDiag} & (2.19) \\ H_r^{Diag} &= \left[\frac{1}{2} (A_1 + A_2) \hat{\mathbf{J}}^2 + \left(A_3 - \frac{1}{2} (A_1 + A_2) \right) \hat{\mathbf{J}}_3^2 \right] \\ H_r^{OffDiag} &= \frac{1}{4} (A_1 - A_2) (\hat{\mathbf{J}}_+^2 + \hat{\mathbf{J}}_-^2) \end{aligned}$$

Here H_r^{Diag} is the diagonal component of the Hamiltonian, $H_r^{OffDiag}$ is the off diagonal component, $\hat{\mathbf{J}}^2$ is the total angular momentum operator, and $\hat{\mathbf{J}}_{\pm}^2$ are the angular momentum raising and lowering operators $\hat{\mathbf{J}}_{\pm} = \hat{\mathbf{J}}_1 \pm i\hat{\mathbf{J}}_2$. Taking the basis states of the wave function to be [32]:

$$|IMK\rangle = \sqrt{\frac{2I+1}{16\pi^2(1+\delta_{K0})}} [\mathcal{D}_{MK}^J + (-1)^J \mathcal{D}_{-KM}^J] \quad (2.20)$$

where δ_{K0} is the Kronecker delta function and \mathcal{D}_{MK}^J are the Wigner D-functions which are functions of the three Euler angles that determine the orientation of the nucleus's principal axes in space. With these basis states the Hamiltonian matrix can be calculated and the energy eigenvalues and eigenstates for a given spin I is a matter of diagonalizing the matrix. The reduced transition probabilities for $E2$ transitions of the triaxial rotor model are given by [119]:

$$\begin{aligned} B(E2, I \rightarrow I') &= \sum_{\mu, K, K'} |\langle I' M' K' | \mathcal{M}_{2\mu}^E | IMK \rangle|^2 & (2.21) \\ \mathcal{M}_{2\mu}^E &= \sqrt{\frac{5}{16\pi}} \left[\mathcal{D}_{\mu 0}^{2*} \hat{\mathbf{Q}}'_{20} + (\mathcal{D}_{\mu 2}^{2*} + \mathcal{D}_{\mu -2}^{2*}) \hat{\mathbf{Q}}'_{22} \right] \\ Q'_{20} &= Q \cos(\gamma) & Q'_{22} &= \frac{1}{\sqrt{2}} Q \sin(\gamma) \end{aligned}$$

2.4.2 Quasiparticle + Triaxial Rotor (QTR)

The QTR model is an extension of the particle + rotor model which was put forth in its earliest form in 1952 by Aage Bohr in Ref. [14]. This model allows the calculation of the effect of coupling the odd quasiparticle to the triaxial even-even core. The lab frame Hamiltonian of this model is given in Ref. [41] to be:

$$H = H_{sqp} + H_{rot} - H_{int} \quad (2.22)$$

$$H_{rot} = A_3 \hat{\mathbf{R}}_3^2 + A_1 \hat{\mathbf{R}}_1^2 + A_2 \hat{\mathbf{R}}_2^2 \quad (2.23)$$

$$H_{int} = \kappa \sum_{\mu} q_{\mu}^* Q_{\mu} = \kappa f r^2 \left(\epsilon \cos(\gamma) \bar{Y}_0^2 + \frac{\epsilon \cos(\gamma)}{\sqrt{2}} (\bar{Y}_2^2 + \bar{Y}_{-2}^2) \right) \quad (2.24)$$

Here H_{sqp} is the single quasiparticle Hamiltonian accounting for the presence of the central potential and the pairing interaction, H_{rot} is the rotor model Hamiltonian, H_{int} is the interaction of the quasiparticle to the triaxial core, $\hat{\mathbf{J}}_k$ is the total angular momentum of the system along the k^{th} axis, $\hat{\mathbf{j}}_k$ is the angular momentum of the quasiparticle along the k^{th} axis, \bar{Y}_m^l is the result of applying the spherical harmonic operator Y_m^l to the basis state, f is the scaling factor obtained from the following:

$$\kappa f = \frac{2}{3} \sqrt{\frac{4\pi}{5}} \hbar \omega_{\circ} \quad (2.25)$$

$$(2.26)$$

and κ is the coupling strength, which is related to the deformation of the system by:

$$\kappa \langle 0 | |Q| |2 \rangle = \hbar \omega_{\circ} \epsilon \cos(\gamma) \quad (2.27)$$

Here $\langle 0 | |Q| |2 \rangle$ is the reduced matrix element of the core quadrupole operator between the 0^+ ground state and the first 2^+ state. This is related to the reduced quadrupole

transition probability as follows:

$$B(E2, J_I \rightarrow J_F) = \frac{|\langle J_F | |Q| |J_I \rangle|^2}{2J_I + 1} \quad (2.28)$$

Qualitatively, the H_{int} works as follows. A high j quasiparticle with predominantly particle nature will align its \vec{j} to the short axis of the core. This orientation results in the maximum overlap of the torus like density distribution of the quasiparticle and the triaxial core which minimizes the energy of the attractive interaction between the two. For a high j quasiparticle with hole nature, the \vec{j} aligns to the long axis which minimizes the overlap of the torus with the triaxial core and minimizes the energy of the repulsive interaction between the two. Finally a quasiparticle from the middle of the shell, possessing particle and hole nature in roughly equal measure, would align the medium axis of the triaxial core.

The reduced transition probabilities of this system can be extracted similarly to those of the triaxial rotor model (equation 2.21); however the operator $\mathcal{M}_{2\mu}^E$ will change to account for the quadrupole moment of both the core (Q) and the quasiparticle (q).

2.4.3 Pairing

The pairing interaction is the force that couples two identical nucleons in time reversed orbits (opposite spin projections). Evidence for this force can be seen in a variety of experimental results, among them: 1) The staggering seen in the single neutron (or proton) separation energies between even and odd neutron (or proton) number (see Fig. 2.10); 2) The ground state of *every* even-even nucleus has $J^\pi = 0^+$; and 3) The ground states of the odd-A nuclei always have J^π determined by the orbital of the last unpaired nucleon.

In 1950, M. Goeppert suggested describing the pairing force as a delta function

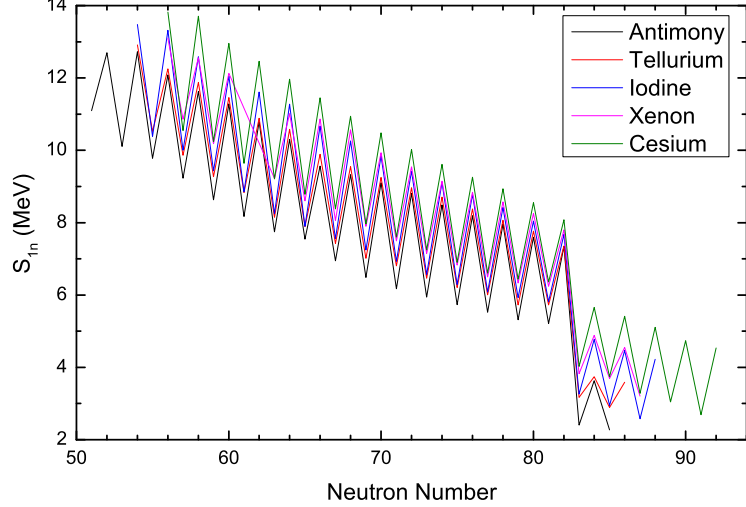


Figure 2.10. One neutron separation energies vs neutron number for the five isotopes from $Z = 51$ to $Z = 55$. The staggering between even and odd masses gives strong evidence for the pairing interaction. Additionally the $N = 82$ shell gap can be seen. Figure adapted from Ref. [93].

multiplied by some interaction strength [73]. Calculations were performed using this interaction to explore its effects [10] and then later analogies between nuclear pairing and BCS superconductivity theory [7] were discovered and examined [18, 75]. The Hamiltonian to describe this interaction is usually written as:

$$H_{pair} = -GP^+P - \lambda\hat{\mathbf{N}} \quad (2.29)$$

Here, λ is the chemical potential, $\hat{\mathbf{N}}$ is the particle number operator, together these give particle number conservation, and G is the pairing interaction strength, which has been determined to have different values for the protons and neutron. For protons the pairing strength is approximately $G_p = \frac{17}{A}$ MeV and for neutrons the pairing strength is approximately $G_n = \frac{23}{A}$ MeV. Finally, P^+ is the monopole pair field, expressed by:

$$P^+ = \sum_{k>0} c_k^+ c_{\bar{k}}^+ \quad (2.30)$$

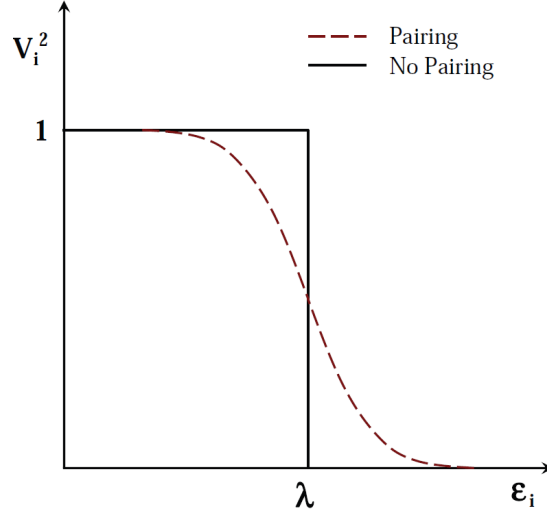


Figure 2.11. Schematic of the occupancy of single particle states with and without pairing. Figure adapted from Ref. [117].

Here \bar{k} represents the time reversed state of k , *i.e.* spin-up \rightarrow spin-down.

If the spacing between levels near the Fermi surface is small relative to G then the pairing interaction scatters pairs of nucleons with $J^\pi = 0^+$ from occupied levels to empty levels above the Fermi level. This results in the “smeared” nucleon distribution shown in the dashed line of Fig. 2.11. If the level spacing is large near the Fermi surface then the pairing interaction cannot scatter pairs into unoccupied levels and the Fermi surface has a sharp cutoff as seen in the solid line of Fig. 2.11.

The energy range that this “smearing” of level occupancies covers is equal to the gap parameter (Δ) which can be defined as follows:

$$\Delta = G \sum_{ij} U_i V_j \quad (2.31)$$

where U is the emptiness factor (the probability that a state will be occupied by a hole) and V is the fullness factor (the probability that a state will be occupied by a

particle). U and V are defined as follows

$$V_i = \sqrt{\frac{1}{2} \left(1 + \frac{\epsilon_i - \lambda}{\sqrt{(\epsilon_1 - \lambda)^2 + \Delta^2}} \right)} \quad (2.32)$$

$$U_i = \sqrt{\frac{1}{2} \left(1 - \frac{\epsilon_i - \lambda}{\sqrt{(\epsilon_1 - \lambda)^2 + \Delta^2}} \right)} \quad (2.33)$$

Here ϵ_i represents the single particle energies, and λ is the chemical potential for a given number of particles. The probabilities are normalized such that $U_i^2 + V_i^2 = 1$. Far below the Fermi surface the probability that an orbit will be occupied is $V_i = 1$, while the probability that the orbit is unoccupied $U_i = 0$. This situation reverses itself far above the Fermi surface. Close to the Fermi surface both probabilities will have a finite value. In BCS theory [7] the quasiparticle energy is expressed as:

$$E_{qp}(n, p) = \sqrt{(\epsilon_i - \lambda)^2 + \Delta^2} \quad (2.34)$$

As the nucleus rotates the induced Coriolis force competes with the pairing interaction. The competition attempts to break the pairs and align the individual angular momenta of the nucleons with the rotation axis. In general rotational motion weakens the pairing strength in the nucleus. While some pairs break and align at specific rotational frequencies, all pairs experience the effects. This phenomenon is called the Coriolis anti-pairing effect (CAP) [78].

2.4.4 Tilted Axis Cranking

The tilted axis cranking (TAC) model [38] is a generalization of the cranked shell model introduced by R. Bengtsson and S. Frauendorf in [11]. In this model, nucleons are individual particles independently moving in an average potential, which in turn rotates about some axis. As expected of a rotating frame, the Coriolis and centrifugal

forces play an important role in the TAC model with consequences for shape, pairing correlations, and quasiparticle orbitals. The Hamiltonian for this model has two terms, the cranking component $-\omega \hat{\mathbf{J}}_x$ which represents the centrifugal and Coriolis forces from the rotating reference frame and a component in the rotating frame, H_0 .

$$H' = H_0 - \omega \hat{\mathbf{J}}_x \quad (2.35)$$

Ref. [38] starts with the pairing plus quadrupole Hamiltonian given by:

$$H_0 = H_{sph} - \frac{\chi}{2} \sum_{\mu=-2}^2 Q_\mu^+ Q_\mu - GP^+P - \lambda \hat{N} \quad (2.36)$$

Here the spherical potential is simply parameterized as by the energy ϵ_k for a state labeled k and then constructed in second quantization as:

$$H_{sph} = \sum_k \epsilon_k c_k^+ c_k \quad (2.37)$$

The short range pair correlations are accounted for using the monopole pair operator defined in Eqn. 2.30. The quadrupole interaction operator accounts for the long range particle-hole interaction:

$$Q_\mu = \sum_{k,k'} \sqrt{\frac{4\pi}{5}} \langle k | r^2 Y_{2\mu} | k' \rangle c_k^+ c_{k'} \quad (2.38)$$

Finally, the term $\lambda \hat{N}$ accounts for the number of particles (N) using the chemical potential λ . As written the Hamiltonian of equation 2.35 only accounts for one type of particles, protons or neutrons; thus all the expressions should be understood as sums across neutron and proton parts.

To determine the system wave functions, $| \rangle$, the eigenstates of the Hartree-Fock-

Bogoliubov (HFB) mean field Routhian are found. The HFB Routhian is:

$$h' = h - \sum_{\mu=-2}^2 (q_{mu} Q_\mu^+ + q_{mu}^* Q_\mu^-) - \Delta(P^+ + P^-) - \lambda N - \omega \hat{\mathbf{J}}_z \quad (2.39)$$

Applying the self-consistency conditions: $q_\mu = \chi \langle Q_\mu \rangle$, $\Delta = G \langle P \rangle$, and conservation of particle number $N = \langle \hat{\mathbf{N}} \rangle$ gives the deformed potential h . Further information regarding operator definitions and procedures for self-consistent solutions can be found in References: [38, 39, 99]

As stated in Refs. [39, 61], self consistent solutions must have their angular frequency and angular momentum vectors parallel *i.e.* $\vec{\omega} \parallel \vec{J}$. Additionally, self consistent solutions to the total Routhian ($E' = \langle H' \rangle$) satisfy the extremum conditions of:

$$\frac{\partial E'}{\partial q_\mu} \Big|_\omega = 0 \quad \frac{\partial E'}{\partial \Delta} \Big|_\omega = 0 \quad (2.40)$$

and have total energy and angular momentum:

$$E(J) = E'(\omega) + \omega J(\omega) \quad J(\omega) = \langle \hat{\mathbf{J}}_z \rangle \quad (2.41)$$

The orientation intrinsic frame is chosen such that the components of the quadrupole tensor satisfy $q'_{-1} = q'_1 = 0$ and $q'_{-2} = q'_2$. With this, the principal axes of the intrinsic frame coincide with the principal axes of the quadrupole tensor and both are related to the lab frame by the three Euler angles ψ , θ , and ϕ shown in Fig. 2.12. The component quadrupole moments of the lab frame, q_μ , are related to the quadrupole moments of the intrinsic frame, q'_μ , as follows:

$$q_\mu = \mathcal{D}_{\mu 0}^2(\psi, \theta, \phi) q'_0 + [\mathcal{D}_{\mu 2}^2 + \mathcal{D}_{\mu -2}^2(\psi, \theta, \phi)(\psi, \theta, \phi)] q'_2 \quad (2.42)$$

With the intrinsic quadrupole moments expressed using the standard deformation

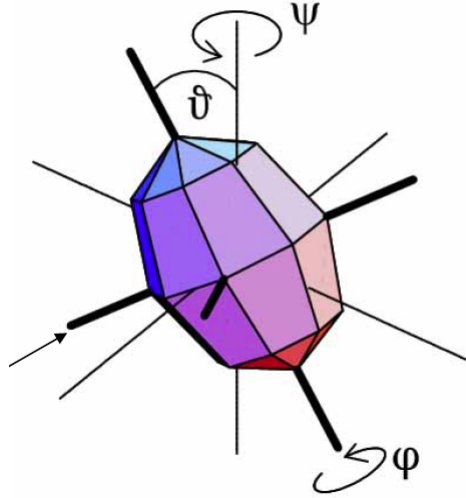


Figure 2.12. Orientation of the rotational axis with respect to the principal axes of the deformed density distribution. Figure taken from Ref. [4].

parameters of the Lund convention:

$$q'_0 = K\beta * \cos(\gamma) \quad q'_2 = -K \frac{\beta \sin(\gamma)}{\sqrt{2}} \quad (2.43)$$

where K sets the energy scale for the deformed potential [38].

As the rotation angle ψ is about the cranking axis, the intrinsic states are invariant with respect to it and it is set to zero. With this, in the intrinsic frame, the mean field Routhian is fixed by β , γ , θ , and ϕ , the two parameters of the deformation and the two parameters of the orientation of $\vec{\omega}$ relative to the principal axes. If we take the angular velocity as:

$$\vec{\omega} = (\omega_1, \omega_2, \omega_3) = \omega(\sin(\theta) \sin(\phi), \sin(\theta) \cos(\phi), \cos(\theta)) \quad (2.44)$$

then the HFB Routhian becomes:

$$h' = h - q'_0 Q'_0 - q'_2 (Q'_2 + Q'_{-2}) - \Delta(P^+ + P) - \lambda \hat{N} \\ - \omega(J_1 \sin(\theta) \sin(\phi) + J_2 \sin(\theta) \cos(\phi) + J_3 \cos(\theta)) \quad (2.45)$$

With this β and γ are determined from the self-consistency equations

$$q'_0 = \kappa \langle Q'_0 \rangle \quad q'_2 = \kappa \langle Q'_2 \rangle \quad (2.46)$$

The remaining Euler angles θ and ϕ are determined from the self-consistency requirement of $\vec{J} \parallel \vec{\omega}$. These parameter sets correspond to extrema of the total Routhian:

$$\frac{\partial E'}{\partial q'_0} \Big|_{\omega} = 0 \quad \frac{\partial E'}{\partial q'_2} \Big|_{\omega} = 0 \quad \frac{\partial E'}{\partial \theta} \Big|_{\omega} = 0 \quad \frac{\partial E'}{\partial \phi} \Big|_{\omega} = 0 \quad (2.47)$$

Of these extrema, only the minima are interpreted as bands.

We can see that there are three possible TAC solutions. They are: the principal axis solution shown in top panel of Fig. 2.13, the planar solution found in the middle panel of Fig. 2.13, and the aplanar solution in the bottom panel of Fig. 2.13. The axial and planar solutions of the TAC model will be discussed further in the subsequent sections. The aplanar solution is of no consequence in this work beyond it giving rise to one of the two unique signatures of nuclear triaxiality *viz.* chirality. Ref. [38] and Ref. [42] have good discussions of this solution and its implications.

2.4.4.1 Rotation About A Principal Axis

If the axis of rotation, (z), coincides with one of the principal axes of the self consistent solution, then the solution is called Principal Axis Cranking (PAC) and

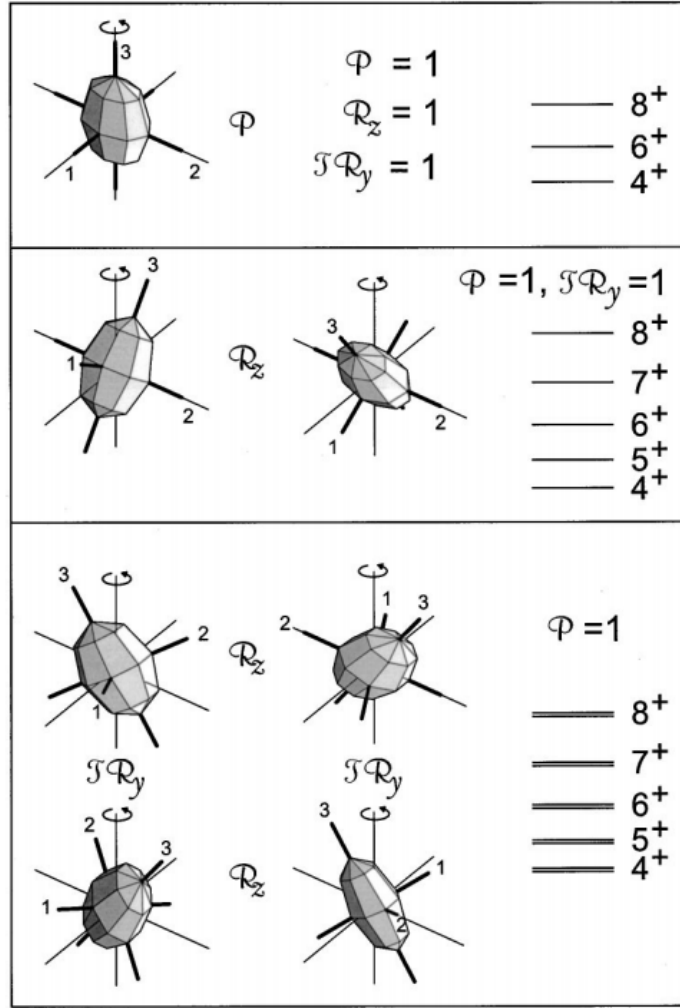


Figure 2.13. Discrete symmetries of the mean field of a rotating triaxial nucleus for each of the TAC solutions along with schematics of the band structures that arise from each solution. The axis of rotation (z), which coincides with the \vec{J} , is marked with a circular arrow. The operators are: \mathcal{P} : Parity inversion, $\mathcal{R}_{y,z}$ Rotation by π about the y or z axis, and \mathcal{T} : Time reversal. Figure adapted from Ref. [38].

the orientation angles satisfy:

$$\theta = 0, \pi/2 \quad \phi = 0, \pi/2 \quad (2.48)$$

The upper panel of Fig. 2.13 shows the PAC case where \vec{J} has the direction of the principal axis 3. In this case the solution has the following properties:

$$\mathcal{R}_z(\pi) |\rangle = e^{-i\alpha\pi} |\rangle \quad (2.49)$$

Here α is the quantum number called signature. In this situation α is a good quantum number and in even-A nuclei taking on values of 0 or 1, while odd-A nuclei have values of $\pm 1/2$. Signature gives the selection rule that the total spin can only take on the following values:

$$I = \alpha + 2n \quad n \in \mathbb{Z} \quad (2.50)$$

here, \mathbb{Z} represents the set of integers. This selection rule shows that the PAC solution represents a single $\Delta I = 2$ band, as illustrated on the right side of the upper panel of Fig. 2.13.

2.4.4.2 Rotation About A Tilted Axis

If the axis of rotation does not coincide with one of the principal axes but still lies within the planes defined by them, then the solution is called the Planar Tilted Axis Cranking (TAC) solution. In this case the orientation angles satisfy:

$$\theta \neq 0, \pi/2 \quad \phi = 0, \pi/2 \quad (2.51)$$

$$\theta = 0, \pi/2 \quad \phi \neq 0, \pi/2 \quad (2.52)$$

The middle panel of Fig. 2.13 shows a case in which the axis of rotation lies in the principal planes spanned by axes 1 and 3. Invariance with respect to rotation about the z-axis by π is lost, yielding:

$$\mathcal{R}_z(\pi) |\rangle \neq e^{-i\alpha\pi} |\rangle \quad (2.53)$$

With the breaking of this symmetry, α ceases to be a good quantum number and there is no longer a selection rule on the total spin. This can be seen schematically on the right side of the middle panel of Fig. 2.13.

Since 1993, when Frauendorf found a set of self-consistent Hartree-Fock mean-field solutions for uniform rotation about a tilted axis [40], TAC has turned out to be a reliable approximation to calculate and investigate the properties of the various types of rotational bands. Details of TAC not covered in this section can be found in Refs. [38–40, 42]

2.5 The Wobbling Mode in Nuclei

2.5.1 Models of the Wobbling Mode

The wobbling mode in nuclei was first predicted by Bohr and Mottelson in the second volume of their textbook on nuclear structure [16]. Their formulation of wobbling was for even-even nuclei using only the triaxial rotor model. Following the nomenclature of Ref. [41], this form of wobbling is called simple wobbling. More recent investigations [41] in wobbling for odd-A nuclei have yielded two more forms of wobbling using the QTR model. These forms are named for the coupling of the quasiparticle. The mode is called “transverse” wobbling if the odd quasiparticle is coupled to an axis perpendicular to the axis of maximum moment of inertia (the intermediate length axis). Contrariwise if the quasiparticle couples to the intermediate axis it is called “longitudinal” wobbling.

2.5.1.1 Simple Wobbling

Simple wobbling, the mode predicted by Bohr and Mottelson in Ref. [16] for even-even nuclei, can be examined entirely within the framework of the TRM, though a semiclassical analysis elucidates the structure of the mode [41]. The rotational kinetic

energy of the system can be written as:

$$E_{rot} = A_3 J_3^2 + A_1 J_1^2 + A_2 J_2^2 \quad (2.54)$$

Additionally the condition that the squares of the components of the angular momentum sum to the square of the total angular momentum must be met:

$$J^2 = J_1^2 + J_2^2 + J_3^2 = I(I+1) \quad (2.55)$$

Together these surfaces give the classical orbits of \vec{J} at the intersection of the angular momentum sphere and energy ellipsoid. Assuming the axes are chosen such that $A_1 > A_2 > A_3$ ($\mathcal{J}_1 < \mathcal{J}_2 < \mathcal{J}_3$), the surface equations can be plotted for 3 different situations as in Fig. 2.14. Here the classic angular momentum orbits can be seen directly in the intersection between the two surfaces. For Fig. 2.14 the rotor parameters were chosen so that $A_1 = 6 * A_3$ and $A_2 = 3A_3$ and A_3 was used to adjust the energy scale of the ellipsoid between the various panels of the plot. The yrast line then corresponds to the two surfaces touching at $J_3 = J$ with rotational energy $E(J) = A_3 J^2$. This is not plotted in any of the panels of Fig. 2.14 as the energy ellipsoid would be contained within the angular momentum sphere, except for an invisible point of contact at $J_3 = J$. In Fig. 2.14 the top panel is an orbit slightly above the yrast line which is the harmonic wobbling motion described by Bohr and Mottelson [16]. The middle panel is the separatrix, representing the unstable rotation about the axis with intermediate MOI. This orbit is the boundary between rotation about the axis with the maximum MOI (axis 3) and the axis with minimum MOI (axis 1) and has a classical frequency of zero. The bottom panel gives an example of an orbit corresponding to rotation about axis 1.

Simple wobbling excitations are small amplitude oscillations of \vec{J} about the axis with the largest MOI (axis 3 in this coordinate system). Their Hamiltonian can be

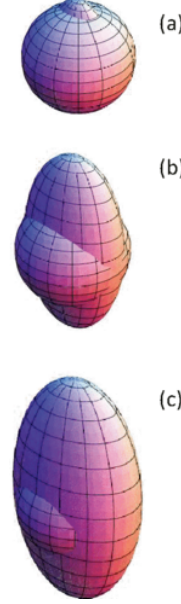


Figure 2.14. Intersections of the angular momentum and energy surfaces for a simple wobbling system with $A_1 = 6 * A_3$ and $A_2 = 3A_3$ for $J = 2$ taken at progressively larger energies from a to c. Figure adapted from Ref. [41].

taken to be [41]:

$$H = A_3 I(I + 1) + \left(n + \frac{1}{2}\right) \hbar\omega_w \quad (2.56)$$

where n is the number of wobbling phonons and the wobbling frequency is:

$$\hbar\omega_w = 2I\sqrt{(A_1 - A_3)(A_2 - A_3)} \quad (2.57)$$

Within the Harmonic Approximation (HA) the intraband reduced transition probabilities $B(E2)$ [119] are:

$$B(E2; (I, n) \rightarrow (I - 2, n)) \approx \frac{5}{16\pi} e^2 Q'_{22}^2 \quad (2.58)$$

Here $Q'_{22} = Q \cos(\gamma)$ where Q is the intrinsic quadrupole moment. The interband

$B(E2)$ s [119] become:

$$B(E2; (I, n) \rightarrow (I - 1, n + 1)) \approx \frac{5}{16\pi} e^2 \frac{n+1}{J} \left(\sqrt{3} Q'_{20} y + \sqrt{2} Q'_{22} x \right)^2 \quad (2.59)$$

$$B(E2; (I, n) \rightarrow (I - 1, n - 1)) \approx \frac{5}{16\pi} e^2 \frac{n}{J} \left(\sqrt{3} Q'_{20} x + \sqrt{2} Q'_{22} y \right)^2 \quad (2.60)$$

Where $Q'_{22} = \frac{1}{\sqrt{2}} Q \sin(\gamma)$ and x and y are defined as follows:

$$x = \sqrt{\frac{1}{2} \left(\frac{A_2 + A_1 - 2A_3}{2\sqrt{(A_1 - A_3)(A_2 - A_3)}} + 1 \right)} \quad (2.61)$$

$$y = \sqrt{\frac{1}{2} \left(\frac{A_2 + A_1 - 2A_3}{2\sqrt{(A_1 - A_3)(A_2 - A_3)}} - 1 \right)}$$

A final note about the simple wobbler is that the wobbling bands have alternating signature. Wobbling bands with an odd number of phonons have signature opposite to that of the yrast band. Contrariwise, wobbling bands with even numbers of phonons have the same signature as the yrast band.

2.5.1.2 Transverse Wobbling

Transverse wobbling, the first of the two new wobbling modes defined by Frauendorf and Dönau in Ref. [41], occurs when the quasiparticle aligns itself perpendicular to the intermediate length axis. The energy ellipsoid for such a system is:

$$E = A_3(J_3 - j)^2 + A_1 J_1^2 + A_2 J_2^2 \quad (2.62)$$

Here the axes are chosen so that axis 3 is the short axis, *i.e.* the axis with intermediate MOI, and axis 2 is the intermediate axis with maximum MOI, yielding: $A_1 > A_3 > A_2$ ($\mathcal{J}_1 < \mathcal{J}_3 < \mathcal{J}_2$). Taking the same angular momentum sphere in equation 2.55 the classical orbits of angular momentum are found in the intersections of the two surfaces

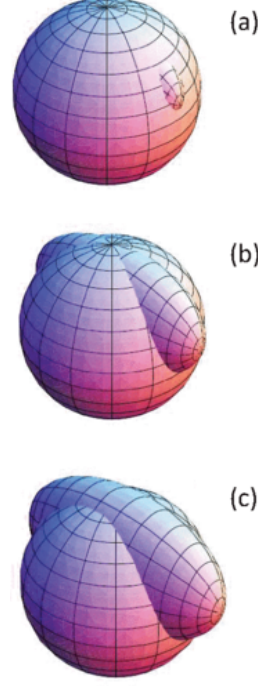


Figure 2.15. Intersections of the angular momentum and energy surfaces for a transverse wobbling system with $A_1 = 6 * A_2$ and $A_3 = 3A_2$ for $J = 3$ taken at progressively larger various energies from a to c. Figure adapted from Ref. [41].

in Fig. 2.15. As with Fig. 2.14, the top panel represents a wobbling state lying a little above the yrast line, the middle panel shows the separatrix, and the bottom panel shows orbits that revolve around axis 3.

Unlike the simple wobbler, in the transverse wobbling case, the separatrix will be encountered here simply with increasing angular momentum. In the simple wobbler increasing J is not enough to encounter the separatrix; the system's stability continues indefinitely. However with transverse wobbling, the offset of the energy ellipsoid causes the separatrix to be encountered at a critical angular momentum $J_c = j A_3 / (A_3 - A_2)$. At this angular momentum the rotational axis of the yrast line changes to point at $j_1 = 0, J_2 = \sqrt{J^2 - J_c^2}, J_3 = J_c$ where the energy ellipsoid touches the angular momentum sphere from the inside.

For $J > J_c$ the rotation is about a tilted axis and as discussed in section 2.4.4.2 this causes signature to cease to be a good quantum number. With this the yrast band collapses into a $\Delta I = 1$ band, destroying the wobbling. Leading up to this collapse is a decrease of the angular frequency.

Applying the frozen alignment approximation (in which it is assumed the particle is firmly coupled to an axis and can be taken simply as a number) and then applying the second order expansion of

$$\hat{\mathbf{J}}_3 = \sqrt{J^2 - \hat{\mathbf{J}}_1^2 - \hat{\mathbf{J}}_2^2} \approx J - \frac{1}{2} \left(\frac{\hat{\mathbf{J}}_1^2}{J} + \hat{\mathbf{J}}_2^2 J \right) \quad (2.63)$$

the QTR Hamiltonian becomes

$$H = A_3(J-j)^2 + (A_1 - \bar{A}_3)\hat{\mathbf{J}}_1^2 + (A_2 - \bar{A}_3)\hat{\mathbf{J}}_2^2 \quad (2.64)$$

$$\bar{A}_3 = A_3(J) = A_3 \left(1 - \frac{j}{J} \right) \quad (2.65)$$

With this the Hamiltonian is in the same form as the TRM Hamiltonian and the same expressions can be used by substituting according to the following pattern $A_3 \rightarrow \bar{A}_3$. This gives Equations 2.59 and 2.58 with the following modified expression for the x and y coefficients.

$$x = \sqrt{\frac{1}{2} \left(\frac{A_2 + A_1 - 2\bar{A}_3}{2\sqrt{(A_1 - \bar{A}_3)(A_2 - \bar{A}_3)}} + 1 \right)} \quad (2.66)$$

$$y = -\text{sign}((A_1 - A_2)J) \sqrt{\frac{1}{2} \left(\frac{A_2 + A_1 - 2\bar{A}_3}{2\sqrt{(A_1 - \bar{A}_3)(A_2 - \bar{A}_3)}} - 1 \right)}$$

Additionally, Frauendorf and Dönau [41] extracted reduced transition probabili-

ties for the $M1$ components of the interband transitions. They are as follows:

$$B(M1; (I, n) \rightarrow (I - 1, n + 1)) \approx \frac{3}{4\pi} \frac{n+1}{J} (j(g_j - g_R)x)^2 \quad (2.67)$$

$$B(M1; (I, n) \rightarrow (I - 1, n - 1)) \approx \frac{3}{4\pi} \frac{n}{J} (j(g_j - g_R)y)^2 \quad (2.68)$$

These semiclassical analyses and expressions are intended to clarify the physics of wobbling. While useful in assisting understanding of these systems, the calculations performed to compare theory with experiment in section 4.2 are done with the full QTR model. Neither the semiclassical approximation nor assumption of frozen alignment are used in the calculations.

2.5.1.3 Longitudinal Wobbling

Longitudinal wobbling is the other possible wobbling mode of an odd- A nucleus. In this case the quasiparticle has aligned itself with the axis of maximum MOI. Using the energy ellipsoid equation of 2.62 but choosing axes such that $A_1 > A_2 > A_3$ ($\mathcal{J}_1 < \mathcal{J}_2 < \mathcal{J}_3$) and finding the classical orbits of the angular momentum gives us the conclusion that, similar to the simple wobbler, this system will remain stable with increasing angular momentum indefinitely. The orbits will not shift with increasing angular momentum preventing the separatrix from being encountered by increasing angular momentum.

Except for a lack of collapse of the wobbling band and the increasing wobbling frequency, longitudinal wobblers behave very similarly to transverse wobblers. Equations 2.59, 2.58, and 2.66 apply to them as well; the only difference is the exact assignment of the axes.

2.5.2 Signatures of Wobbling

There are several signatures of wobbling. These signatures can be broken into two broad categories: Signatures that require lifetime information and those that do not.

There are two observables that do not require a lifetime measurement. The first observable is the measurement of the experimental wobbling frequency which is defined as:

$$\hbar\omega_w = E(I, n = 1) - (E(I + 1, n = 0) - E(I - 1, n = 0))/2 \quad (2.69)$$

These wobbling frequencies, while not a unique observable of wobbling, will allow differentiation between longitudinal and transverse wobbling modes in odd-A nuclei. The second observable is unique to wobbling bands. This signature is that $n_w = x \rightarrow n_w = x - 1$ interband transitions must be of $\Delta I = 1, E2$ nature. This is measurable using angular distributions.

In the lifetime measurement category there are two observables. Measuring the lifetime of a state allows the $B(E2)$ values to be extracted. As seen in equation 2.59 the $B(E2, (I, n) \rightarrow (I - 1, n - 1)) \propto n_w/I$. Coupled with the mixing ratio, this gives us two observables. Observing the $B(E2, (I, n) \rightarrow (I - 1, n - 1))$ of a wobbling band as spin increases allows the $1/I$ proportionality to be verified. If a two phonon band is identified, the n dependance of the proportionality can be verified as well.

CHAPTER 3

EXPERIMENTAL METHODS

Across experimental physics there is a common theme in the design of experiments. One part of this theme is finding a way to produce the system for study. Another part is designing the equipment to collect the signals required to interpret what the system is doing. In nuclear physics, the appropriate choice of reaction will create the desired system and the equipment for signal collection will depend on what is to be measured. This chapter will discuss the reaction, detectors, and techniques used in the examination of transverse wobbling in ^{135}Pr .

3.1 Heavy-ion Fusion-evaporation Reaction

Nuclear physics uses a vast array of reactions. Restricting the focus to in-beam gamma-ray spectroscopy, there are common “workhorse” reactions. Of these workhorse reactions the heavy-ion fusion-evaporation reaction is frequently chosen for its selectivity in final products, its production of relatively few species with large cross-section, and its creation of states with a large amount of angular momentum [9].

3.1.1 Creation and Decay of the Compound Nucleus

The fusion-evaporation reaction proceeds by the formation of a highly excited compound nucleus, a mechanism first proposed by N. Bohr[19]. It is possible for a compound nucleus to be formed for beam energies below the Coulomb barrier; however, the probability is dramatically lower as the beam must quantum mechanically

tunnel through the Coulomb barrier. Therefore for heavy ion fusion to be experimentally feasible the center of momentum energy must exceed the height of the Coulomb barrier. The Coulomb barrier height can be estimated with:

$$E_{CB} = \frac{\alpha \hbar c Z_p Z_t}{1.16 fm (A_p^{1/3} + A_t^{1/3} + 2)} \quad (3.1)$$

and the non-relativistic center of momentum energy is:

$$E_{cm} = \frac{\mu}{A_p} E_p \quad (3.2)$$

here the subscripts p and t denote projectile and target respectively, A is the mass number, Z represents the nuclear charge, α is the fine structure constant, and $\mu = A_p A_t / (A_p + A_t)$ is the system's reduced mass. After its formation the compound nucleus will have an excitation energy of

$$E_{ex} = Q + E_{cm} \quad (3.3)$$

where Q is the reaction's Q -value which is

$$Q = (M_t + M_p - M_{CN})c^2 \quad (3.4)$$

The compound nucleus will also carry an angular momentum ranging between $0\hbar$ and $l_{max}\hbar$, corresponding to head on and peripheral collisions, respectively. l_{max} can be estimated classically as

$$l_{max} = \frac{\sqrt{2\mu(E_{cm} - E_{CB})}}{4} (A_p^{1/3} + A_t^{1/3})\hbar \quad (3.5)$$

Following its formation, a compound nucleus will be left in a state with high excitation energy. The two primary ways the compound nucleus rids itself of this

excess energy are fission[21] or particle evaporation followed by gamma-ray emission. A schematic of of a fusion-evaporation reaction is in Fig. 3.1.

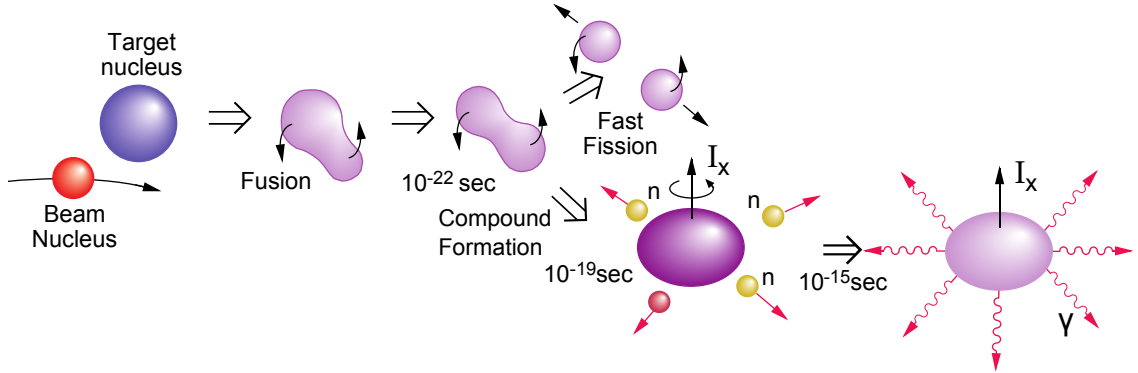


Figure 3.1. Schematic illustration of heavy-ion fusion-evaporation, adapted from Ref. [69].

The probability of the compound nucleus fissioning is governed by the height of the fission barrier relative to the nucleus's excitation energy. The height of the fission barrier is a function of the A of the nucleus and is inversely proportional to the compound nucleus's angular momentum, as can be seen in Fig. 3.2. However, even the complete disappearance of the fission barrier does not guarantee fission as there are a few observed cases of spins above those required to reduce the barrier to zero[43, 56].

If the compound nucleus does not fission, then it will evaporate particles. Particle evaporation is the emission of protons, neutrons, or alpha particles over or through an emission barrier. For charged particles, this emission barrier is composed both of a centrifugal term which grows with increasing angular momentum and a Coulomb

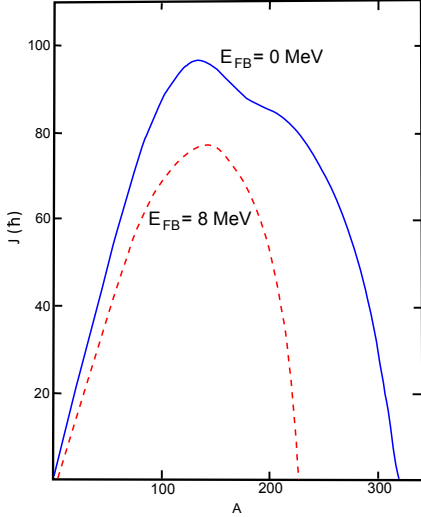


Figure 3.2. Isocontours of angular momenta that yield fission barriers of 8 MeV and 0 MeV at various masses. Note that the 0 MeV height barrier occurs at higher spins for a given mass, showing the inverse dependence of fission barrier height on angular momentum. Adapted from Ref. [29].

term. For neutrons the emission barrier is solely the centrifugal barrier. In most cases neutron evaporation will be more probable, because charged particles encounter a higher barrier due to the Coulomb term. The exception occurs for very neutron deficient nuclei where the reduction of proton separation energies make it possible for charged particle emission to compete with, or even dominate, neutron emission. Each successive evaporated particle carries energy, but little angular momentum away from the nucleus until there is insufficient excitation energy for particles to penetrate the emission barrier and the nucleus is left in a state that is stable against particle emission. From this point on, the nucleus must dissipate its excess angular momentum and excitation energy via gamma ray emission. A schematic of this is in Fig. 3.3.

Initially, the nucleus is in a state with such high level density that it decays by the emission of statistical gamma rays [13]. These statistical gamma rays are almost purely dipole in nature and form a quasi-continuum as the very high level densities make discrete states impossible to distinguish. As the nucleus approaches the yrast

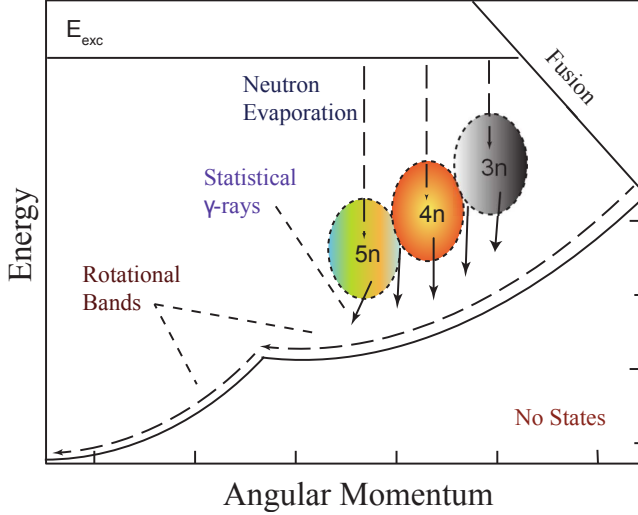


Figure 3.3. Schematic of the compound nuclear decay assuming that a rotational nucleus is being formed. Adapted from Ref. [4].

line (the states with the minimum excitation energy for a given angular momentum), the level density drops. This allows the emission sequences of discrete gamma rays which feed the yrast line.

3.1.2 Choice of Beam and Target

When choosing the beam and target for a fusion-evaporation, several factors must be considered: What is the production cross-section of the desired residual nucleus? How clean is the production of the desired residual nucleus relative to the other residuals? What is the spin range to be studied? What is the availability of the isotopes to be used as targets? What is the suitability of the material for beam production? While beam target combinations are usually chosen to maximize the cross-section for the desired residual, in some cases there are other channels open which will have large cross-sections themselves. In these cases the beam-target combination might be chosen to drastically lower the relative yield in competing channels at the cost of lowering the cross-section for the desired residual. For lower spins, lighter pro-

jectiles are a more likely choice. Eqn. 3.5 shows that it is possible to increase the angular momentum transfer with higher beam energies; however this also increases the excitation energy of the compound nucleus, causing particle evaporation to be more probable. In the end the decision is based on which combination yields the nucleus to be studied at the spins to be studied with the highest absolute and relative cross-sections possible.

Ref [27] gives the empirical estimate for $A_{CN} > 100$ for obtaining the optimum beam energy for producing a specific residual nucleus in a (HI,xn) reaction, found below in Eqn. 3.6.

$$E_{pk}(x) = (-Q_x + \alpha x)(1 + \frac{A_p}{A_t}) \quad (3.6)$$

Here Q_x is the Q-value for the production of the residual nucleus given by:

$$Q = (M_t + M_p - M_{res} - xM_n)c^2 \quad (3.7)$$

and α is ~ 6 MeV. The reaction will only have a reasonable cross-section if $E_{pk}(x)$ is greater than E_{CB} , which is the height of the Coulomb barrier, given in Eqn. 3.1. Computer codes that employ statistical models such as PACE4[44, 112] can now be used to calculate the cross-sections of products from these reactions allowing estimation of peak beam energies and optimal beam-target combinations. A plot of cross-sections yielded by calculations such as these can be found in Fig. 3.4.

3.2 Gamma-ray Spectroscopy

3.2.1 Gamma-ray Interaction with Matter

As noted the choice of equipment will vary with the signals to be collected to understand the system. One of the obvious signal choices for a residual nucleus at high spins is the gamma rays it emits. Detection of gamma rays is dependent on the gamma

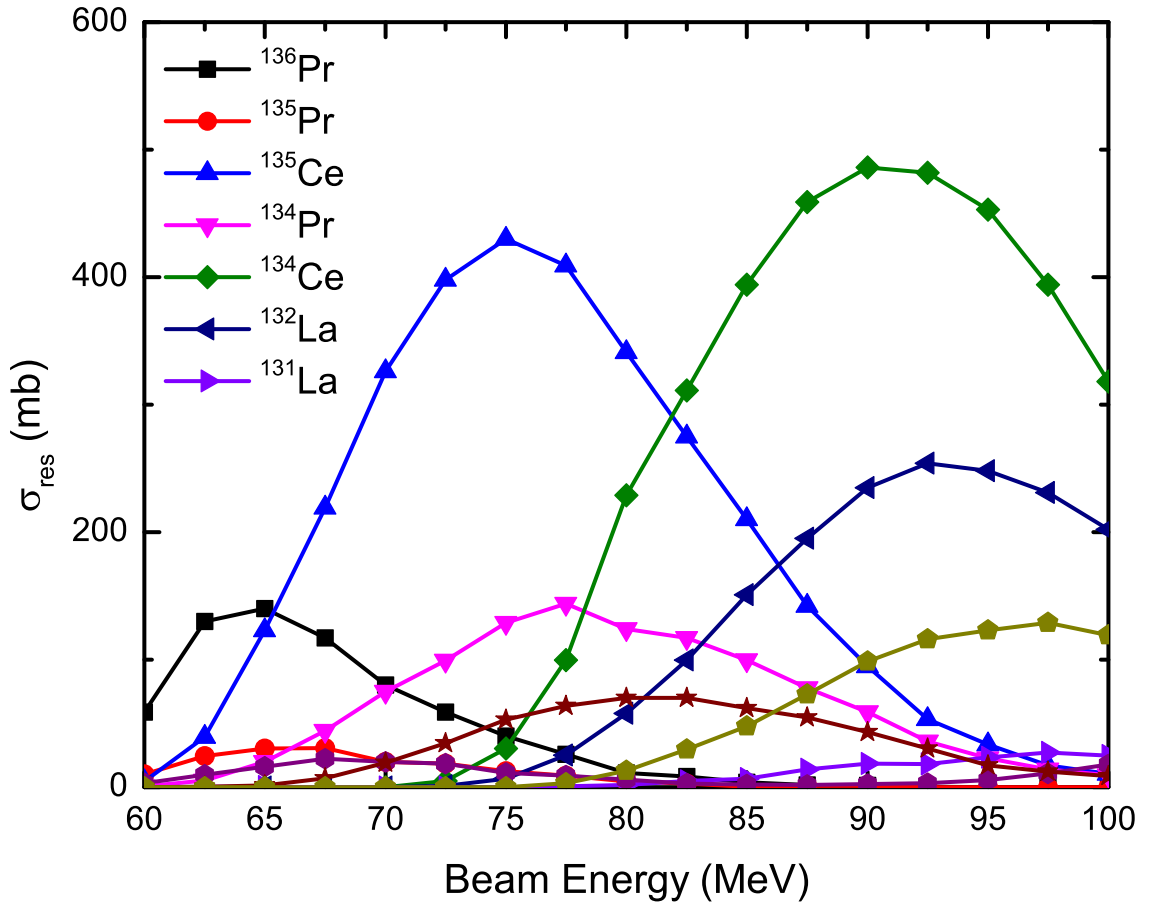


Figure 3.4. Cross-sections of various residual nuclei for a ^{16}O beam on ^{123}Sb at a variety of beam energies as calculated by PACE4. As ^{139}Pr is the compound nucleus produced all products that are not isotopes of Pr require the evaporation of a charged particle.

ray depositing energy in a detector which in turn depends on the interactions of electromagnetic radiation with matter. At the energies relevant to nuclear physics, $10 \text{ keV} < E_\gamma < 15 \text{ MeV}$, there are three primary processes to be considered, photoelectric absorption, Compton scattering, and pair production. These three processes compete with each dominating in a different energy range.

In *photoelectric absorption*, the photon interacts with a bound electron in the detector material and is fully absorbed[37]. The total energy of the photon is then used to overcome the binding energy of the electron and to provide the electron with

kinetic energy, giving $E_{e^-} = E_\gamma - E_b$. The electron then proceeds to lose energy as it passes through the detector material. In gamma-ray spectra the full energy peak corresponds to the complete deposition of the primary photon's energy in the detector medium. For that to occur, either the primary photon, or all the secondary photons (generated by the processes below), must undergo photoelectric absorption. As seen in Fig. 3.5, the photoelectric effect is dominant at low energies and the energy at which the photoelectric effect ceases to dominate increases with the Z of the material.

In *Compton scattering* a gamma-ray photon scatters from an electron in the material at some angle θ to its original direction[30]. Due to conservation of momentum and energy, the energy transferred to the electron is precisely determined by θ and so the energy of the secondary photon can be written as: $E_s = E_p(1 + \frac{E_p}{m_e c^2}(1 - \cos \theta))^{-1}$. As above the electron then deposits its kinetic energy in the medium as it slows. However, unlike in the photoelectric effect, not all of the energy is deposited in the electron. After scattering the secondary photon travels in its new direction and is free to interact again with probabilities dictated by its energy. Fig. 3.5 shows Compton scattering is the dominant effect at intermediate energies.

The final process to be considered is pair production. In pair production, the photon enters the region of very strong electric field near the nucleus and its energy is converted into the mass and kinetic energy of an electron-positron pair [2, 86]. Since energy is conserved, the photon must have energy of at least twice the rest mass of the electron, giving a threshold of $E_\gamma \geq 1.022$ MeV for this interaction; any energy above this threshold is converted into kinetic energy shared between the two particles. After their production the electron and positron will both travel through the detector medium loosing energy as they travel. Once at rest the positron will annihilate with an electron, emitting two anti-parallel 511 keV secondary photons. Fig. 3.5 shows the dominance of this interaction at high gamma energies; the energy

at which pair production supersedes Compton scattering decreases with increasing Z of the material.

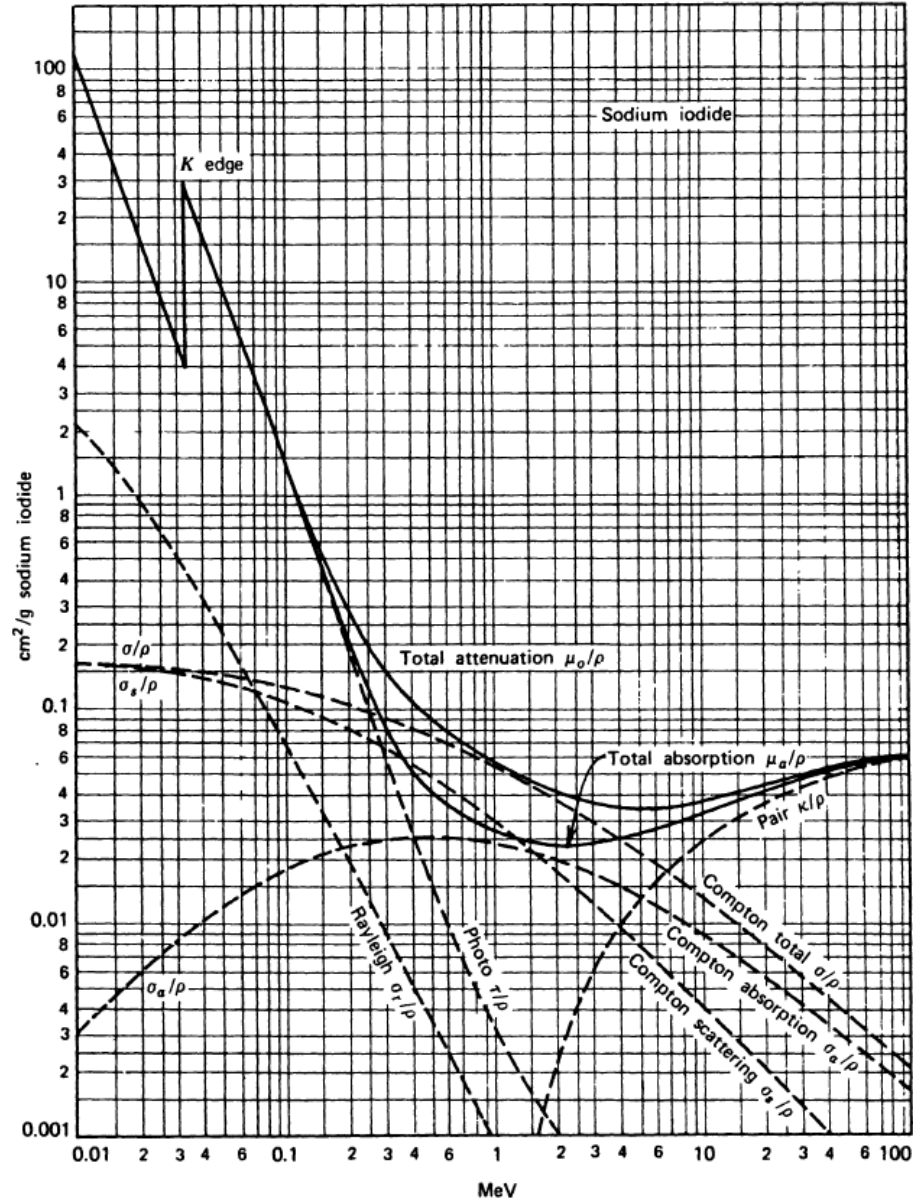


Figure 3.5. Gamma-ray attenuation coefficients for various processes in NaI, adapted from Ref. [63]. Note the dominance of photoelectric absorption at lower energies, Compton scattering at intermediate energies, and pair production at high energies. While the slopes of these processes change from material to material, the trends remain the same.

3.2.2 High Purity Germanium (HPGe) Detectors

In detecting gamma rays there are essentially 3 major classes of detector: scintillator, gas, and semiconductor detectors. In all cases, the gamma ray enters the active volume of the detector and deposits energy by at least one of the processes mentioned above. The primary energetic electrons, produced directly by the interactions of the gamma ray, proceed to ionize or excite other electrons in the material. The secondary electrons are then detected in some manner. In scintillators, the secondary electrons cause UV or visible light to be emitted and this is collected via photomultiplier tube, or similar device, to produce a voltage pulse. In gas and semiconductor detectors, the charge of the secondary electrons (and their corresponding ions or holes) is collected directly, albeit via different mechanisms, to produce the voltage pulse.

It is desirable that gamma-ray detectors have both good detection efficiency and energy resolution. Current gamma-ray detectors are unable to satisfy both goals. It is necessary to decide which parameter is more important. For high spin experiments where the spectrum is dense with peaks, the energy resolution is the top priority since broad peaks would be indistinguishable from each other. Of the available detectors semiconductor detectors, particularly High Purity Germanium (HPGe) detectors, offer the best energy resolution.

Semiconductor detectors are either p-n or p-i-n junction diodes with a reverse bias voltage applied. Here, p means semiconductor material doped with electron acceptors (positive), n means semiconductor material doped with electron donors (negative), and i means intrinsic (undoped) semiconductor material. At the boundary between the types of materials, there is a so called contact potential. This potential gives rise to an electric field which causes the migration of charges between the two materials until there is an area bridging the boundary called the depletion zone. In this zone, there is an electric field which gives rise to a potential that counters the contact potential. By applying reverse bias to the diode, the contact potential is effectively

increased causing the depletion zone to expand (schematic in Fig. 3.6). This is desirable because the depletion zone is the only region of the semiconductor where an electric field will exist. This means that electron-hole pairs formed within it are swept away from each other for collection before they can recombine. In contrast, electron-hole pairs formed outside the depletion zone are not pulled away from each other and thus recombine, preventing their collection. Due to this, the depletion zone of the detector is the region that is active. That is to say that the passage of ionizing radiation through that region is detectable because the electron-hole pairs produced are collected.

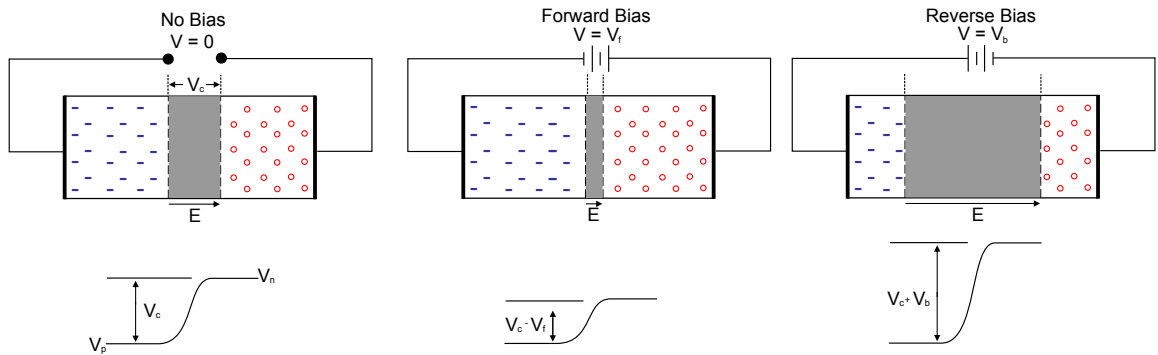


Figure 3.6. Above: Diagrammatic view of the depletion zone's with varying bias voltage. Below: Voltage difference across the depletion zone for each bias voltage shown above.

The higher the purity of the semiconductor, the higher the reverse bias voltage that can be applied without reaching the breakdown of the semiconductor (usually a catastrophic event). In HPGe detectors the purity is sufficiently high that almost the whole crystal of Ge can be depleted yielding a very large active region, an advantage for gamma rays given their low interaction probabilities compared to charged parti-

cles. When a gamma ray interacts in an HPGe detector, it produces at least one high energy secondary electron or positron (more if there are multiple interactions). These secondary electrons lose energy quickly as they pass through the detector, leaving a trail of electron-hole pairs in their wake. The electrons and holes are then swept to their respective contacts by the applied potential and collected.

A detector's resolution is defined as the FWHM for a given peak. The intrinsic resolution of a semiconductor detector stems from statistical fluctuations in how many electrons and holes are collected at the terminals. These fluctuations arise from simple counting statistics; their form can be described by:

$$\Delta E_{in} \propto \frac{E_\gamma}{\sqrt{N}} \quad (3.8)$$

Where N is the number of charge carriers produced and is approximately E_γ/ϵ where ϵ is the average energy to make an electron hole pair (2.96eV for Ge). In a more precise examination the intrinsic component of the FWHM is:

$$\begin{aligned} \Delta E_{in}(E) &= 2\sqrt{2\ln(2)} \frac{\sqrt{FE_\gamma/\epsilon}}{E_\gamma/\epsilon} E_\gamma \\ &= 2.355\sqrt{F\epsilon E_\gamma} \end{aligned} \quad (3.9)$$

Here F is the Fano factor. The value of F , intrinsic to the detector material, ranges across $(0, 1)$ and takes into account energy loss mechanisms available to the secondary electron(s) that do not generate electron-hole pairs. A more thorough explanation is available in Refs. [62, 63].

Unfortunately the detector's intrinsic resolution is not the only contributor to the detector's resolution. There are also contributions from such sources as electronic noise, charge carrier collection/trapping, and Doppler broadening. If it is assumed that these components are independent and normally distributed; the actual resolu-

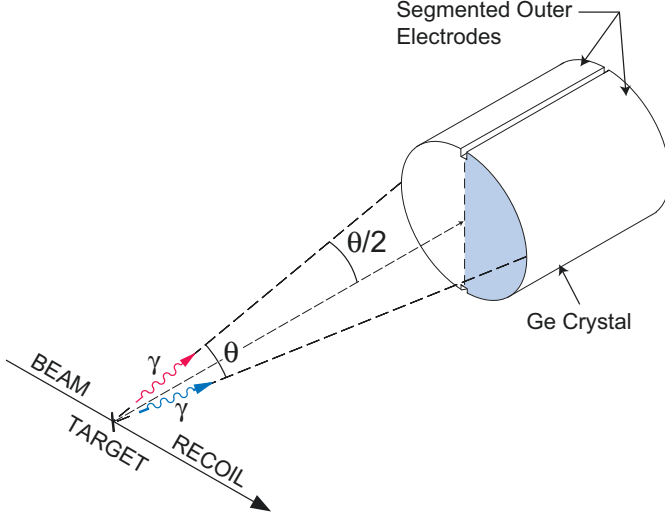


Figure 3.7. Diagram showing the uncertainty inherent in the gamma ray's angle of emission, and Gammasphere's segmented electrode scheme to reduce this.

tion is:

$$\Delta E_T^2 = \Delta E_{in}^2 + \Delta E_E^2 + \Delta E_{C/T}^2 + \Delta E_D^2 \quad (3.10)$$

Where ΔE_E is the electronic noise contribution, $\Delta E_{C/T}$ is the charge collection/trapping term, and ΔE_D is the Doppler broadening term. Ref. [98] gives the FWHM forms of the noise and collection/trapping terms as:

$$\Delta E_E = N_{1/2} \quad (3.11)$$

$$\Delta E_{C/T} = 2.355 \sqrt{\epsilon K E_\gamma [1 - \eta(\vec{r})]} \quad (3.12)$$

Where $N_{1/2}$ is the FWHM of the electronic noise, K is a constant of a given detector, and $\eta(\vec{r})$ is the total charge collection efficiency of electrons and holes of the detector as a function of the interaction site's position.

The final term, ΔE_D , of this equation comes from uncertainty in the angle at which the gamma ray was emitted from the recoiling nucleus due to the detectors

finite size (shown in Fig. 3.7). The shift in gamma energy due to the nuclear recoil is:

$$E_o = E_e \frac{\sqrt{1 + \beta \cos(\theta)}}{\sqrt{1 - \beta \cos(\theta)}} \quad (3.13)$$

Here, the subscripts o and e refer to observed and emitted, β is the speed of the recoiling nucleus divided by c and θ is the angle between the nucleus's line of a flight and the emitted gamma ray. If the detector has an angular acceptance of $\theta_0 - \delta\theta \leq \theta \leq \theta_0 + \delta\theta$ with θ_0 , the central angle of the detector then the leading order term of the Doppler broadening contribution to the resolution is:

$$\Delta E_D = 2\beta \sin(\theta) \sin(\delta\theta) E_\gamma \quad (3.14)$$

There are three strategies to combat this term. The first is geometrical. By increasing the granularity of the array, either by using more and smaller detectors or by using more detectors at a longer distance from the source. This in turn would shrink the opening angle of detectors and therefore reduce the Doppler broadening. The second method is electrical in nature, by segmenting the outer contact of the detector; even roughly, the location of the interaction within the detector can be determined. This effectively reduces the opening angle. Gammasphere uses this strategy as shown in Fig. 3.7. The split outer contact allows the reduction of the effective opening angle, $2\delta\theta$, from 14.9° to 7.45° [68]. The third method involves a physical segmentation of the detector by having multiple crystals in close proximity within the same cryostat. This combination produces a detector that has a volume equal to the sum of the individual crystal volumes. However despite this large volume, the opening angle of the individual crystals is the opening angle to consider for the Doppler broadening. Thus a physically segmented detector can give you a smaller Doppler broadening than an unsegmented detector of the same volume. INGA, a clover detector array, and cluster detectors[35, 36, 80] are examples of this strategy.

3.2.3 Escape Suppression with BGO Detectors

The primary contribution to the background in gamma-ray spectroscopy is the incomplete deposition of energy in the detector. Two of the mechanisms discussed in section 3.2.1 can lead to this. Compton scattering will result in incomplete energy deposition when the secondary photon yielded by the process escapes the HPGe crystal without depositing the rest of its energy. This mode results in a smooth background from the maximum energy transferable to an electron in the process down to zero energy. Pair production will yield incomplete energy deposition when one or both of the photons from the annihilation of the positron escape the detector. This mode results in 2 new peaks forming, the first 511 keV below the photopeak, corresponding to one annihilation photon escaping, and a second 1022 keV below the photopeak, corresponding to both escaping.

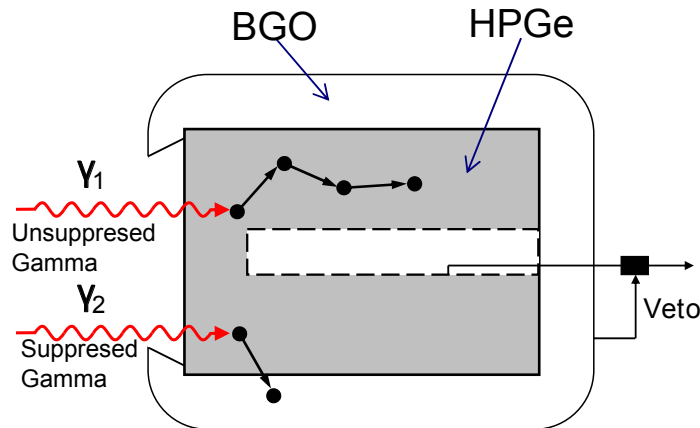


Figure 3.8. Schematic of BGO escape suppression around an HPGe crystal.

To ameliorate this, the principal detector is surrounded by a secondary detector

and the electronics are set to be in anti-coincidence (see Fig. 3.8 for a schematic). If both detectors have energy deposited, the event is discarded. In practical application, the second detector must be highly efficient at detecting gamma rays to minimize its size. Given this constraint, the scintillator Bismuth Germanate (BGO) is an excellent choice for escape suppression. While BGO's energy resolution is quite poor, it has excellent timing characteristics and quite high density and it is made of fairly high Z materials. The latter two facts give it the desired high detection efficiency (substantially higher than the HPGe it is shielding). Improvements up to a factor of 2.48 in the peak-to-total ratio (P/T) can be seen for some designs. A bare HPGe detector having a (P/T) of 0.270 ± 0.002 has been shown to improve to 0.669 ± 0.002 ^[8] with an escape suppression shield around the sides and part of the back (some space needs to be left for cables to exit the HPGe.) Example spectra showing this improvement can be seen in Fig. 3.9.

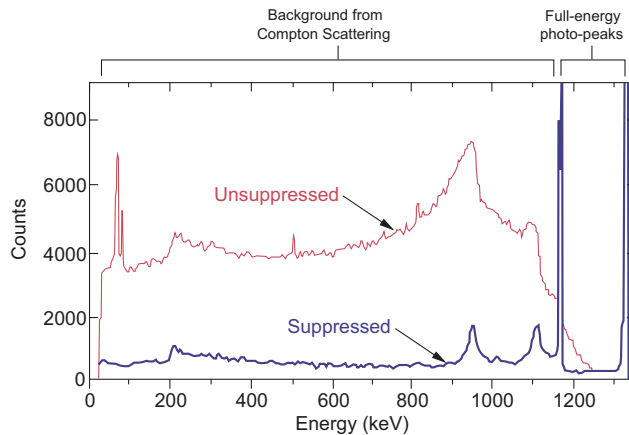


Figure 3.9. Superimposed spectra of an escape suppressed and unsuppressed detector. Adapted from Ref. [69].

3.2.4 The Gammasphere Detector Array

Gammasphere (partially pictured in Fig. 3.10) is an array of 110 escape suppressed HPGe detectors arranged in a sphere around a target. A cross sectional view of part of the array is found in Fig. 3.11. The BGO shields are arranged in hexagonal shapes around each detector plus a backplug covering the majority of the back of the detector. Gammasphere's spherical geometry is comprised of 17 rings of detectors, with each ring at a distinct angle to the beam axis. Using a scheme called honeycomb suppression, Gammasphere has a total efficiency of 0.09 at 1 MeV and a singles P/T of 0.69.

TABLE 3.1

GAMMASPHERE FEATURE SUMMARY

No. Detectors	110
No. Segmented Detectors	70
HPGe Detector Size	7.1cm (D) $\times 8.22\text{cm}$ (L)
Detector Volume	312.8cm^3
Target to HPGe Front	24.6cm
Total HPGE Solid Angle	$0.46 \times 4\pi$
Total Peak Efficiency	0.094 at 1.3 MeV
Singles P/T	0.6 at 1.3 MeV
Energy Resolution (MeV)	2.1 keV at 1.3 MeV

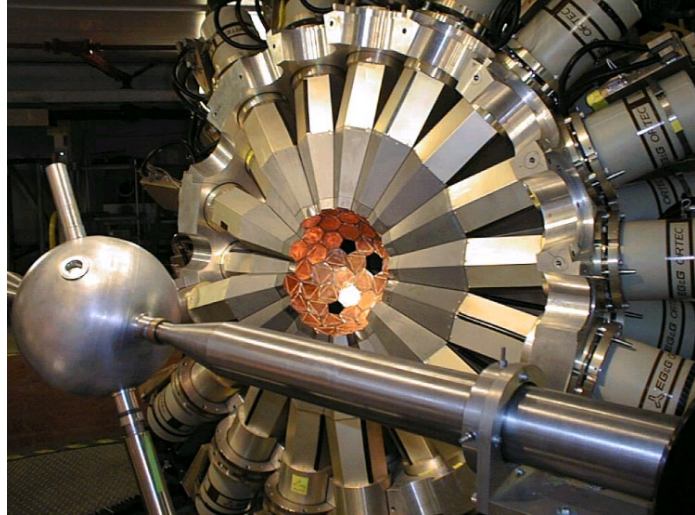


Figure 3.10. View of scattering chamber and interior of one of Gammasphere's hemispheres pulled back from the chamber. The hexagonal copper foils are x-ray absorbers.

Honeycomb suppression is an escape suppression scheme that uses the BGO shields of adjacent detector modules to effectively double the thickness of a detector's shields. As seen in Fig. 3.11, almost every module will have additional modules immediately adjacent to it. If the HPGe detector for a given module does not register energy deposition, the 6 side segments of its BGO shield are used to double the thickness of the shields to which they are adjacent. Without this measure the singles P/T is ~ 0.62 ; using honeycomb suppression improves this to ~ 0.69 though it reduces the total efficiency at 1.332 MeV from ~ 0.095 to ~ 0.089 [68]. Table 3.1 contains a brief summary of Gammasphere's features drawn from Refs. [8, 33, 68, 83].

As mentioned in section 3.2.2, some of Gammasphere's detectors have a split outer electrode to reduce the effective half angle. Detector positions can be found in table A.1 and table A.2 in appendix A. Gammasphere's high granularity, good energy resolution, and efficiency make it a boon for high gamma-ray multiplicity coincidence measurements.



Figure 3.11. Cross-section schematic of part of Gammasphere. Adapted from Ref.[69].

3.2.5 Indian National Gamma Array (INGA)

The Indian National Gamma Array (pictured in Fig. 3.12) is an array of 24 escape suppressed HPGe clover detectors[80]. Since INGA utilizes clover detectors, it is sensitive to the polarization of gamma rays emitted from nuclei in aligned states[35]. Additionally, the use of clover detectors make the array more efficient for high energy gamma ray when using add back mode to sum the energies deposited in each of the individual crystals.

INGA utilizes a digital data acquisition system (DAQ) that allows it to run in a triggerless mode, producing time-stamped data from a 10ns clock[87]. Digital data



Figure 3.12. Exterior view of INGA.

acquisition systems, because they digitize the preamp signal directly, can operate at higher counting rates than analog, because they do not require multiple microseconds of signal shaping time. The downside of this mode is that coincidences are not prebuilt by the DAQ and instead need to be constructed by moving a sliding window of the desired coincidence time across the timeline of events and selecting sets of gamma rays that occur within that window. A final advantage of the time-stamped events is that isomers can have their lifetime measured using time differences between gamma rays as seen in Fig. 3.13.

Using its digital DAQ and add-back on the clover crystals, INGA achieves a total efficiency of ~ 0.05 and P/T of 0.4 at ~ 1.33 MeV. Table 3.2 contains summary of INGA's features. INGA's sensitivity to polarization, efficiency, and granularity make it a good system for intermediate gamma-ray multiplicity coincidence measurements, reaching its best efficiency at 2- to 3-fold events.

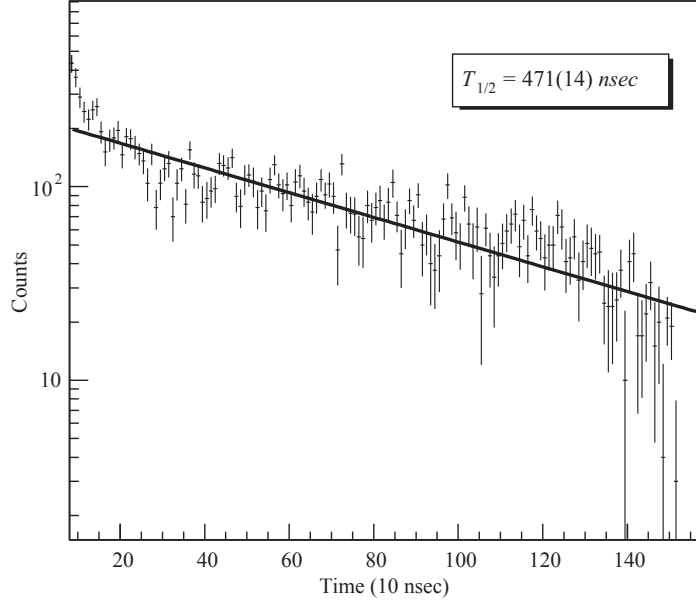


Figure 3.13. Example isomer timing spectrum for INGA. From Ref. [87].

3.3 Experimental Details

The work on ^{135}Pr presented in this dissertation was performed at two different facilities, the ATLAS (Argonne Tandem Linear Accelerator System) facility with the Gammasphere detector system and the TIFR-BARC Pelletron LINAC with the INGA detector system. At both facilities the $^{16}\text{O}(^{123}\text{Sb}, 4n)^{135}\text{Pr}$ reaction was used. As mentioned in section 3.1 the choice of beam and target affects both the most probable channel, the excitation energy, and the maximum angular momentum of the compound (and residual) nucleus. In previous in-beam gamma-ray spectroscopy literature the following heavy ion fusion-evaporation reactions have been used to yield the ^{135}Pr residual nucleus: $^{120}\text{Sn}(^{19}\text{F}@91 \text{ MeV}, 4n)^{135}\text{Pr}$ [103], $^{123}\text{Sb}(^{16}\text{O}@76 \text{ MeV}, 4n)^{135}\text{Pr}$ [22], and $^{116}\text{Cd}(^{23}\text{Na}@115 \text{ MeV}, 4n)^{135}\text{Pr}$ [90]. The ^{16}O and ^{123}Sb projectile-target combination was chosen for its lighter projectile to optimize for population of states away from the yrast line.

TABLE 3.2

INGA FEATURE SUMMARY

No. Clover Detectors	24
No. Single Crystals	96
Single Crystal Size	$5\text{cm (D)} \times 7\text{cm (L)}$
Single Crystal Volume	117.5cm^3
Target to HPGe Front	24cm
Total HPGE Solid Angle	$0.25 \times 4\pi$
Total Peak Efficiency	0.05 at ~ 1.0 MeV
Singles P/T	0.40 at 1.3 MeV
Energy Resolution (MeV)	2.2 keV at 1.3 MeV

3.3.1 ATLAS/Gammasphere

ATLAS is located at Argonne National Laboratory in Argonne, Illinois, USA. ATLAS is the world's first superconducting linear accelerator (linac) for projectiles heavier than an electron. It consists of 3 sections. The first of these sections is the injector accelerator an electron cyclotron resonance (ECR) ion source coupled to a 12 MV low velocity LINAC ("PII", Positive Ion Injector). The beam from the injector is sent to the 20 MV "booster" linac and finally to the 20 MV "ATLAS" linac. This system produces pulsed beams with spot diameter ≤ 1 mm, pulse length ≤ 500 ps, and interval 82 ns, which range across all elements from hydrogen to uranium with energies of 7 – 17 MeV per nucleon.

The Gammasphere detector system was used in the FMA (Fragment Mass Analyzer) position though the FMA itself was not used. This configuration requires that the first ring of detectors at $\theta = 17.27465^\circ$ be removed from the array due to a lack

of space. Additionally several other detectors were removed from the array due to various issues. A complete listing of the detector numbers missing from the array is presented in Table A.3 in Appendix A.

Multiple self supporting ^{123}Sb targets were prepared for the experiment using 98.28% enriched powder from ISOFLEX USA (PO Box 29475, San Francisco, CA 94129 USA)[46]. Due to the low thermal conductivity ($0.243\text{W}/\text{cm}/\text{K}$ at 300K [57]) and high vapor pressure[46, 92] of Sb, a thin layer ($14\mu\text{g}/\text{cm}^2$) of Al was deposited on the front surface of the targets created. This served the dual purpose of helping to dissipate the heat deposited in the target by the beam and of inhibiting sputtering of the target. Two foils, $630\mu\text{g}/\text{cm}^2$ and $634\mu\text{g}/\text{cm}^2$, were placed on the target ladder for Gammasphere. An oxygen beam of $3pnA$ at 81.2 MeV was then impinged on the $634\mu\text{g}/\text{cm}^2$ target (the other target served as backup in case of failure of the primary target.) To further reduce the risk of evaporating a hole in the target, the beam was wobbled by placing a sinusoidal voltage on vertically and horizontally positioned plates upstream of the target. The amplitudes were 1.0V for the $\hat{\mathbf{x}}$ -axis and 1.1V for the $\hat{\mathbf{y}}$ -axis.

3.3.2 TIFR - BARC Pelletron LINAC / INGA

The TIFR-BARC pelletron linac is located at the Tata Institute of Fundamental Research (TIFR), Mumbai, India. It is a collaborative project between TIFR and the Bhabha Atomic Research Centre (BARC) and is the first superconducting heavy ion accelerator in India. The first section of the system is a 14MV tandem Van de Graaf accelerator. The beam emitted from the pelletron is then bunched and injected into a linac yielding beam pulses with a width of $\sim 600ps$ ranging across most of the elements from hydrogen to chlorine at $5 - 10\text{ MeV/nucleon}$.

The INGA detector system was used in its standard position at the facility; however a few detectors were not present due to various problems. A summary of the

electronics connections and detectors is in Table B.2.

The two self supporting targets used in the Gammasphere experiment were given thick gold backings of $20.3\text{mg}/\text{cm}^2$ for the $630\mu\text{g}/\text{cm}^2$ target and $22.8\text{mg}/\text{cm}^2$ for the $634\mu\text{g}/\text{cm}^2$ [46]. This served two purposes: The backing would allow a doppler shift attenuation measurement to determine lifetimes (this unfortunately proved impossible) and the thick gold backing allowed heat deposited in the target by the beam to be easily dissipated, negating the need for a beam wobbling system.

3.4 Data Processing

As stated earlier, this work was performed at two facilities. In the experiment using Gammasphere $\sim 185\text{Gb}$ of data spread across 104 files were collected. The data set was comprised of 3.57×10^9 three- and higher-fold events with the distribution across folds shown in Fig. 3.14. While the system was set to not trigger for less than three-fold events, lower-fold events still sometimes pass through due to honeycomb suppression. Because honeycomb suppression is applied after the system has triggered, it effectively removes gamma rays from an event, reducing the fold, even to below the threshold set in the trigger system. The data from this experiment were used for the construction of the level scheme and extraction of angular distributions and DCO ratios.

In the experiment utilizing INGA, $\sim 550\text{Gb}$ of data spread across ~ 800 files were collected. As INGA was run in a triggerless mode, each module of electronics output time-stamped events in each detector to a file. Afterwards, the data are merged into an order according to their time-stamp, yielding $\sim 503\text{Gb}$ of data spread across 185 files. Construction of events then proceeds by setting a coincidence time window and “scanning” the window across the merged events looking for sets of events whose time stamps all fall within that window. This process yielded 3.52×10^9 two- and higher-fold events. These data were used for the extraction of polarizations using the

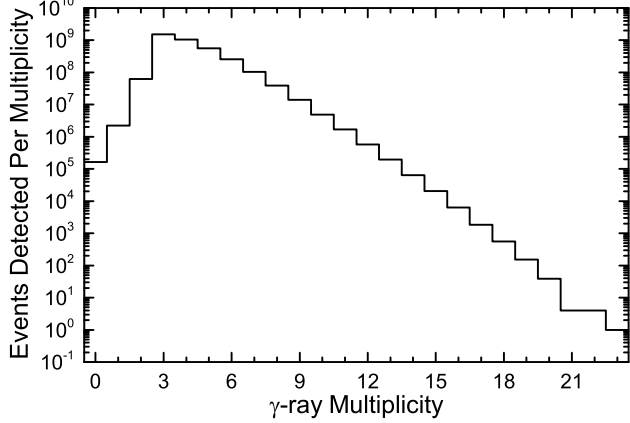


Figure 3.14. Histogram of the number of events in each multiplicity for the experiment at Gammasphere.

scattering asymmetry at 90° . This and requiring that the energy be seen in two and *only* two of the crystals of a 90° detector, reduced the number of eligible two- and higher-fold events to 3.47×10^8 .

These data were processed using both histogram mode (matrices, cubes, and hypercubes)[94] and list mode[24, 31] systems. The histograms mode analyses were used to extract level schemes with symmetric gates. List mode and asymmetric matrices were used when asymmetric gates were necessary, as is it is in the extraction of angular distributions and polarizations.

3.4.1 Calibration

Prior to working with the actual data from an experiment, it is necessary to perform energy and efficiency calibration of the detectors. For gamma-ray detection experiments of this kind, calibration involves placing a radioactive source with known lines in the same position that the beam would strike the target. If absolute efficiency is desired as opposed to relative efficiency, the activity of the source must be known. This allows determination of exactly how many gamma rays passed through the

detector. In this case, only relative efficiency was necessary; so this information was neglected.

TABLE 3.3

^{152}Eu PEAK DATA

Peak No.	Energy (keV)	Rel. Intensity.
1	121.783(2)	13620(160)
2	244.692(2)	3590(60)
3	344.276(4)	12750(90)
4	411.115(5)	1070(10)
5	443.976(5)	1480(20)
6	778.903(6)	6190(80)
7	867.388(8)	1990(40)
8	964.131(9)	6920(90)
9	1112.116(17)	6490(90)
10	1408.011(14)	10000(30)

At the Gammasphere experiment a ^{152}Eu source was used for calibration. ^{152}Eu has many peaks; the 10 strongest (non-overlapping) peaks were chosen for use. A representative spectrum from a typical detector with the chosen peaks numbered is found in Fig. 3.15. A listing of the energies and relative intensities of these peaks is found in Table 3.3. For the INGA experiment a ^{152}Eu and ^{133}Ba mixed source was

used for calibration purposes; a listing of the energies and relative intensities of the ^{133}Ba peaks is found in Table 3.4. An example of a single crystal spectrum for INGA can be found in 3.16. The peaks are labeled with both the index number of the peak and a superscript denoting which nuclide was its origin.

TABLE 3.4

^{133}Ba PEAK DATA

Peak No.	Energy (keV)	Rel. Intensity.
1	80.999(4)	5120(40)
2	276.404(7)	1130(10)
3	302.858(5)	2920(30)
4	356.014(9)	10000(30)
5	383.859(9)	1450(20)

For Gammasphere after extraction of the spectra, energy calibration of each detector was performed as follows. First, using the program *gf3* from the Radware tool suite[94], each of the 10 peaks was fit with a Gaussian peak shape plus linear background whose formula is:

$$Fit(x) = he^{-\frac{(x-\mu)^2}{2\sigma^2}} + a + b(x - \bar{x}) \quad (3.15)$$

Where x is the channel number, h is the peak height, μ is the peak centroid,

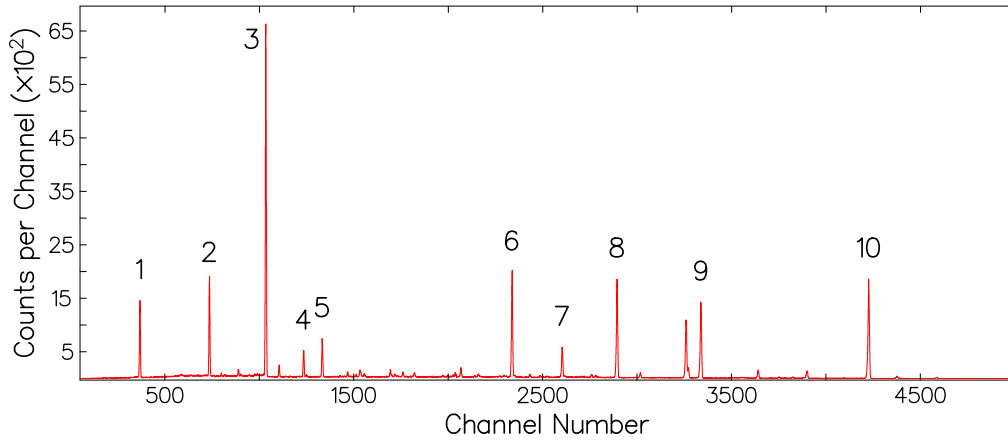


Figure 3.15. ^{152}Eu calibration spectrum from a typical Gammasphere detector.

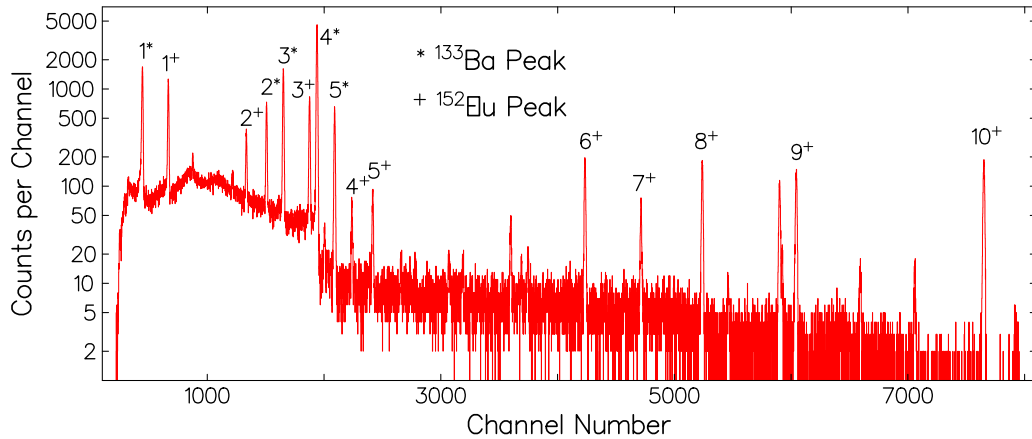


Figure 3.16. Typical ^{152}Eu and ^{133}Ba mixed source calibration spectrum from a single crystal of an INGA clover detector.

$2\sqrt{2\ln(2)}\sigma$ is the FWHM of the peak, a is the constant term of the background, b is the linear term of the background, and \bar{x} is the center of the region to be fitted. From these shapes the peak area ($\sqrt{2\pi}\sigma h$) and centroid were extracted. For energy calibration the centroids were combined with the corresponding energies and fitted with polynomials (as in Eqn. 3.16) from 2nd to 5th order.

$$E = a_0 + a_1x + a_2x^2 + a_3x^3 + a_4x^4 + a_5x^5 \quad (3.16)$$

The polynomial with the lowest reduced χ^2 was selected to be the energy calibration for that detector. A listing of the energy calibration parameters used for Gammasphere is found in Table A.4.

For INGA following the extraction of single crystal spectra, energy calibration was performed by using *gf3* to fit each of the peaks of interest and extract the positions of each peak. After gathering the peak positions and combining them with their respective energies, a 2nd order polynomial was fitted. No higher order polynomials were used due to both the enhanced linearity of a digital data acquisition system and limitations in the code used for further analysis. A listing of the energy calibration parameters used for INGA can be found in Table B.3.

For Gammasphere the peak areas were divided by the corresponding relative intensities in Table 3.3 to give the relative efficiency of each peak, following energy calibration. Then, using the program *effit* from the Radware suite, the energies and relative efficiencies of each peak were fitted with:

$$\ln(\epsilon) = [(A + Bx + Cx^2)^{-G} + (D + Ey + Fy^2)^{-G}]^{-1/G} \quad (3.17)$$

Here A , B , and C are parameters that control the low energy part of the efficiency, though C is usually set to 0.0. D , E , and F are the parameters that control the high energy component of the efficiency. G is the parameter that controls the “sharpness” of the intermediate energy turnover region where they play equal roles. The parameters x and y are related to the gamma-ray energy as follows:

$$x = \ln\left(\frac{E_\gamma}{100 \text{ keV}}\right) \qquad y = \ln\left(\frac{E_\gamma}{1000 \text{ keV}}\right)$$

A plot of extracted relative efficiencies and the fit to them for a Gammasphere detector can be found in Fig. 3.17. A listing of the relative efficiency calibration parameters used for Gammasphere is found in Table A.4.

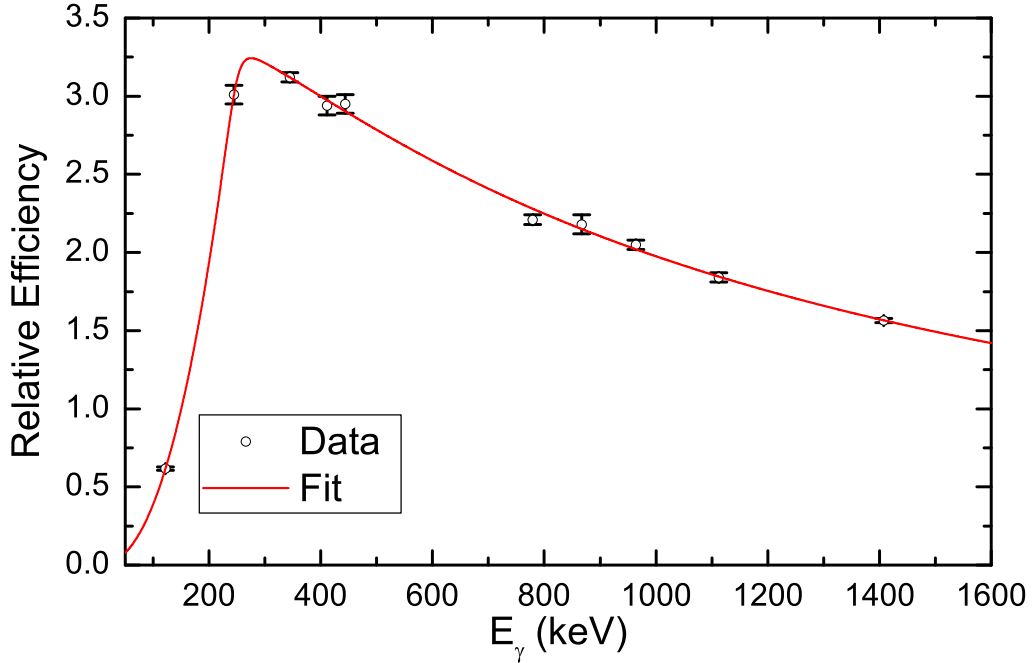


Figure 3.17. ^{152}Eu extracted relative efficiencies and fit.

As it was unnecessary for the asymmetry analysis performed on the INGA data, a relative efficiency calibration was not performed.

3.4.2 Level Scheme Scheme Determination

The analysis of the Gammasphere thin target data involved constructing the level scheme using the Radware software package[94]. Radware uses symmetrized multi-dimensional histograms to store high-fold events. In these multidimensional arrays,

each axis corresponds to a gamma-ray energy and each bin in the array corresponds to a event with that particular combination of gamma-ray energies seen within a $1\mu s$ window. The histograms are symmetrized by sorting the gamma-ray energies of each event such that $E_1 \leq \dots \leq E_d$. By this method, the number of bins in the histogram can be reduced from n^d (where n is the number of bins per axis and d is the number of axes) to:

$$Size = \frac{1}{d!} \prod_{i=1}^d (n + i) \quad (3.18)$$

While this still scales with n^d it reduces somewhat the large storage requirements. Events that are of lower dimensionality than the histogram are ignored and events that are of higher fold than the histogram, f , are “unfolded” into $\binom{f}{d}$ unique events.

Construction of a nucleus’s level scheme involves gating on one or more transitions and examining the resultant spectra which will show what transitions are in coincidence with the gates. A gate on a symmetrized histogram is a projection of the histogram along one of its axes with restrictions on the summation of the other axes. As an example, equation 3.19, shows an ungated projection of a matrix (2-d histogram). Equation 3.20 shows a single gate on a matrix.

$$S_i = \sum_{j=0}^{n-1} M_{ij} \quad (3.19)$$

$$S_i^{g_1} = \sum_{j=g_{lo}}^{g_{hi}} M_{ij} \quad (3.20)$$

Here S_i is the counts of bin i in the resultant spectrum, $S_i^{g_1}$ is the counts of bin i in the gated spectrum, M_{ij} is the counts at bin i, j in the matrix, g_{lo} and g_{hi} are the bounds of the gate, and n is the number of bins per axis of the matrix. Expressions for higher order gates and higher dimensional histograms follow logically from these expressions.

The peaks in the spectrum yielded by gating on one or more gamma rays corre-

spond to the gamma rays that are in coincidence with the gated gamma rays. If two transitions are in coincidence, they must all be part of the same cascade through the level scheme. Therefore at *least* individually, each of the peaks in the gated spectrum will be part of the same cascades as the gamma rays chosen for the gate. By varying which gamma rays are gated upon and observing the intensity of the gated transitions, it is possible to determine the placement of essentially all the gamma ray transitions in the level scheme.

3.4.3 Background Subtraction

A spectrum can be thought of as having two components, the background part and the peak part. Any given segment of this background is made from gamma rays that were in random/“accidental” coincidence and gamma rays that were in true coincidence and only deposited part of their energy in the detector. When a gate is placed on an energy range, the gate is on both peak and background components. In addition to this the gamma rays that are in coincidence with a gate are likewise composed of background and peak themselves. The removal of these backgrounds is vital in the analysis of gamma-ray coincidence data.

3.4.3.1 Symmetric Gates

For symmetric gates where all the axes can be taken to be equivalent, the background subtraction algorithm, developed by Radford in Ref. [95], is used. For a cube (3-*d* histogram), this background is:

$$B_{ijk} = \frac{1}{T} (M_{ij}b_k + M_{ik}b_j + M_{jk}b_i) + \frac{1}{T^2} (b_i b_j b_k - P_i b_j b_k - b_i P_j b_k - b_i b_j P_k) \quad (3.21)$$

Here M_{ij} is two dimensional projection of the cube, P_i is the projection of the cube, b_i is the smooth background component of the cube’s projection, and T is the total

counts in the cube.

$$M_{ij} = \sum_k C_{ijk} \quad (3.22)$$

$$P_i = p_i + b_i = \sum_{jk} C_{ijk} \quad (3.23)$$

$$T = \sum_{ijk} C_{ijk} \quad (3.24)$$

Similar expressions are derived for gates on matrices and hypercubes ($4-d$ histograms) in Ref [95]. The extraction of the smooth background component b_i from the total projection P_i can be seen in Fig. 3.18. An example of the background from this procedure and the results of the subtraction can be seen in Fig. 3.19.

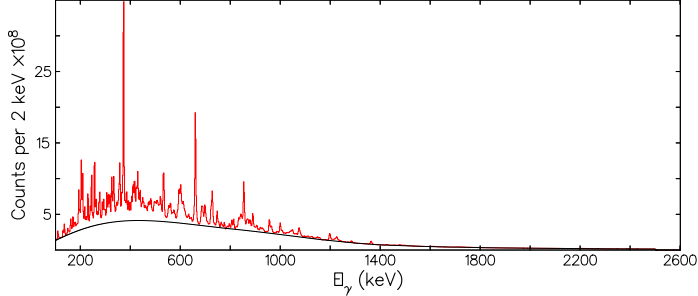


Figure 3.18. Total projection spectrum and its smooth background drawn below it.

3.4.3.2 Asymmetric Gates

Some types of data analysis, such as those examined in Section 3.5, require asymmetric gates where the \hat{x} -axis of the spectrum produced is not the same as the axes

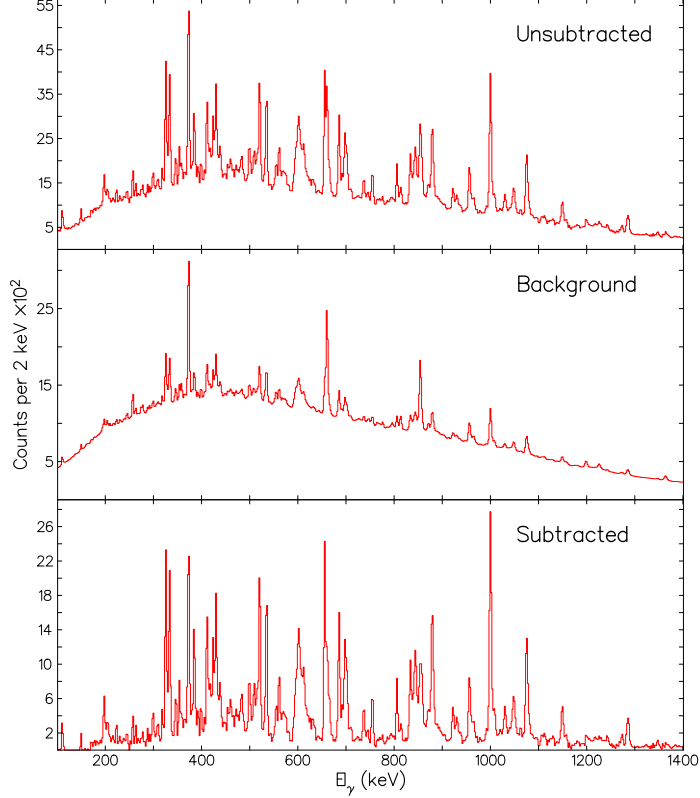


Figure 3.19. Spectra of a symmetric triple gate on a hypercube showing the components of the gates spectrum. Top: The unsubtracted gated spectrum. Middle: The background spectrum for the gate. Bottom: The final background subtracted spectrum.

that were gated on/summed across. For example the projection axis is gamma rays recorded in a specific ring of the array while the gate is placed on all the rings of the array. In such cases the background subtraction method developed by Starosta et al. in Ref [109] is desirable. If a double gate is considered on γ_1 and γ_2 , then events in that double gate will fall into four categories: 1) Peak-Peak (pp): both γ_1 and γ_2 are correctly identified. 2) Peak-Background(pb): γ_1 is correctly identified and γ_2 comes from background. 3) Background-Peak(bp): γ_1 is from background and γ_2 is correctly identified. 4) Background-Background (bb): both γ_1 and γ_2 are from background. Similar combinations apply to higher order and lower order gates. The

spectrum to be examined should be made up solely of events from the first category. To subtract events that fall into categories 2, 3, and 4 we first realize:

$$S_{pp}(j) = S_{tt}(j) - B_{\gamma\gamma}(j) \quad (3.25)$$

$$B_{\gamma\gamma}(j) = N_{bp}S_{bp}(j) + N_{pb}S_{pb}(j) + N_{bb}S_{bb}(j) \quad (3.26)$$

$$N = N_{pp} + N_{pb} + N_{bp} + N_{bb} \quad (3.27)$$

S_{pp} is the spectrum corresponding to events that are in the first category, S_{tt} is the spectrum of all events that satisfy the gate, N_x is the number of events in category $x \in \{pp, pb, bp, bb\}$, and S_x is the spectrum of events that falls into category x , normalized to have a total of 1 count.

With the assumption that the background is uncorrelated, it follows that for category bb , the corresponding spectrum will be proportional to the total projection spectrum. This assumption also gives that the spectra for categories pb and bp will be proportional to the background subtracted spectra of a single gate on those peaks. From this we have the following relations:

$$S_{bb}(j) = \frac{1}{T}P(j) \quad T = \sum_j P(j) \quad (3.28)$$

$$S_{pb} = \frac{1}{N_{BgSub}^{g_1}}S_{BgSub}^{g_1}(j) \quad N_{BgSub}^{g_1} = \sum_j S_{BgSub}^{g_1}(j) \quad (3.29)$$

$$S_{bp} = \frac{1}{N_{BgSub}^{g_2}}S_{BgSub}^{g_2}(j) \quad N_{BgSub}^{g_2} = \sum_j S_{BgSub}^{g_2}(j) \quad (3.30)$$

$$S_{BgSub}^{g_i}(j) = S^{g_i}(j) - b_i \frac{N_{g_i}}{T}P(j) \quad N_{g_i} = \sum_j S^{g_i}(j) \quad (3.31)$$

Where S^{g_i} are the unsubtracted, unnormalized spectra resulting from a single gate on a single transition, $P(j)$ is the total projection spectrum of all gamma multiplicities the gate is applied to, and b_i is the background to total ratios of peak i of the peaks that were gated on, extracted via the standard methods, *e.g.* Fig. 3.20. It is also

worth noting that $N_{B\gamma Sub}^{g_i} = N_{g_i}(1 - b_i)$, combining this with equations 3.25 through 3.31 yields the for $B_{\gamma\gamma}(j)$ given in 3.32.

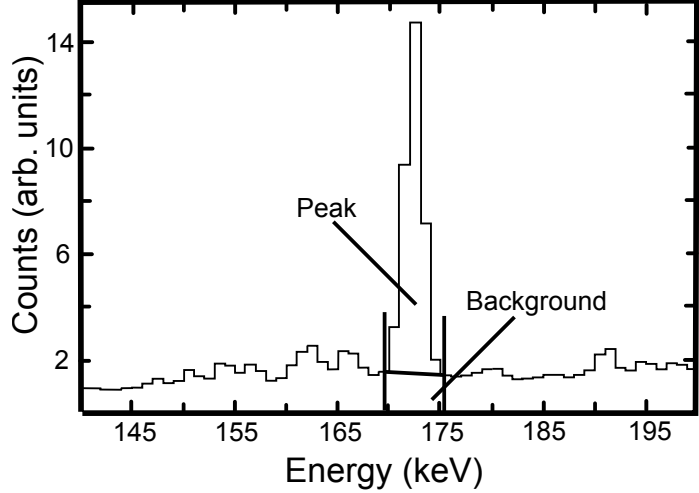


Figure 3.20. Extraction of the peak and background, where $p + b = 1$.
Adapted from Ref. [109].

$$B_{\gamma\gamma}(j) = N \left(\frac{b_2^{g_1}}{N^{g_1}} S^{g_1}(j) + \frac{b_1^{g_2}}{N^{g_2}} S^{g_2}(j) - \frac{b_1 b_2^{g_1} + b_2 b_1^{g_2}}{2T} P(j) \right) \quad (3.32)$$

Where $b_i^{g_k}$ is the background to total ratio of peak i in $S^{g_k}(j)$, extracted similarly to the b_i of Equation 3.31. This expression removes spurious correlations which arise from the background components of the gating transition(s). However, there is a further smooth background that results from the incomplete suppression of escapes. This smooth background can be accounted for in one of two ways. The first is to remove it via the prescription shown in Ref. [109], which uses a scaled smooth background of the total projection like that in Fig. 3.18. The second method is to account for it locally with a background term in during peak fitting. In this work

the latter method was chosen for simplicity.

3.5 Directional Correlation of Gamma-rays from Oriented Nuclei (DCO)

Angular distribution measurements, angular correlation measurements, and polarization measurements all rely on the radiation emitting nucleus being oriented in some fashion. There are three broad categories of methods for establishing the orientation of the nucleus. The first category involves using a beam to impose an orientation via nuclear reaction (such as fusion-evaporation) or Coulomb excitation [50, 66]. In the second category a sample of radioactive atoms that have non-zero spin are cryogenically cooled and an external magnetic field is applied [67]. The spins align in this field to the extent determined by their temperature and the field strength. The final category involves not forcing the nucleus into some orientation, but observing its orientation by taking the direction of a radiation preceding the gamma ray of interest to be the \hat{z} -axis [50, 66]. A diagrammatic scheme for the emission of two successive radiations X_1 and X_2 is found in Fig. 3.21.

The full correlation function describing the situation in Fig. 3.21 can be written as follows[50, 66]:

$$W(\theta_1, \theta_2, \phi) = \sum_{\lambda_1, \lambda, \lambda_2} B_{\lambda_1}(I_1) A_{\lambda}^{\lambda_2 \lambda_1}(X_1) A_{\lambda_2}(X_2) H_{\lambda_1 \lambda \lambda_2}(\theta_1, \theta_2, \phi) \quad (3.33)$$

Here λ_1 and λ_2 are the ranks of the statistical tensors that describe the orientation of states I_1 and I_2 , λ is the tensor rank of the radiation field, $B_{\lambda_1}(I_1)$ is the orientation coefficient, $A_{\lambda}^{\lambda_2 \lambda_1}(X_1)$ is the generalized directional distribution coefficient, $A_{\lambda_2}(X_2)$ is the directional distribution coefficient, and $H_{\lambda_1 \lambda \lambda_2}(\theta_1, \theta_2, \phi)$ is the angular function defined in Eqn. 3.36. The angles referenced in Eqns. 3.33 and 3.36 are defined in Fig. 3.22. Additionally, X_i corresponds to a listing of the pertinent information about the i^{th} radiation, namely $X_i = (\delta_i, L_i, L'_i, I_{i+1}, I_i)$. Here L_i is the low-order multipolarity

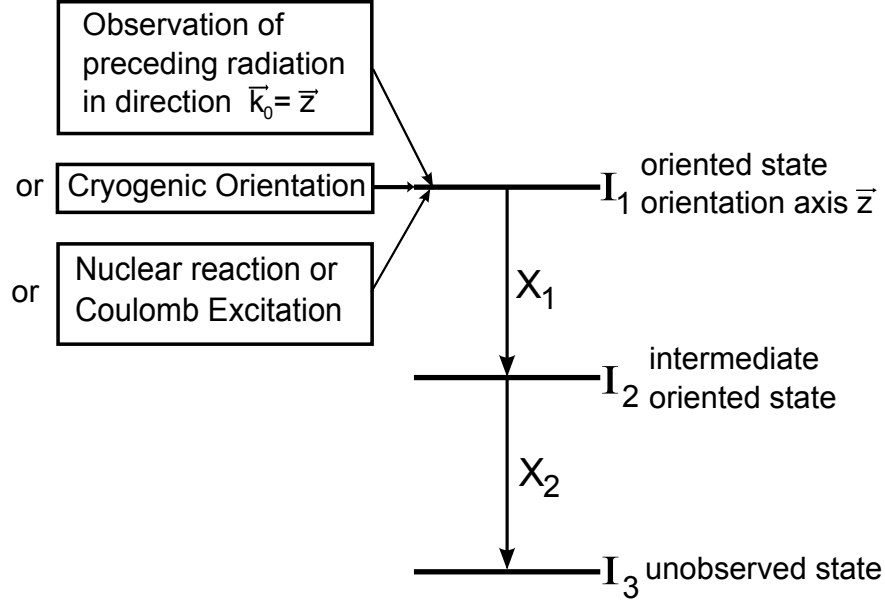


Figure 3.21. Emission of two successive radiations X_1 and X_2 from an oriented nuclear state, I_1 .

of radiation i , L'_i is the high-order multipolarity of radiation i , δ_i is the mixing ratio between the two multipolarities, I_i is the initial state for the radiation, and I_{i+1} is the final state for the radiation. The mixing ratio δ is defined as a ratio of matrix elements as in Eqn. 3.34 or as the square root of a ratio of intensities as in Eqn. 3.35. While it is possible to define formulae for $B_{\lambda_1}(I_1)$, $A_{\lambda}^{\lambda_2 \lambda_1}(X_1)$, and $A_{\lambda_2}(X_2)$ to accommodate three multipolarity components, a situation where the highest order component is strong enough to require accounting for is extremely unlikely and so henceforth only equations for two components will be given.

$$\delta = \frac{< I_2 || j_N A_{L'}^{\pi'} || I_1 >}{< I_2 || j_N A_L^{\pi} || I_1 >} \quad (3.34)$$

$$\delta = \sqrt{\frac{I_{\gamma}(L')}{I_{\gamma}(L)}} \quad (3.35)$$

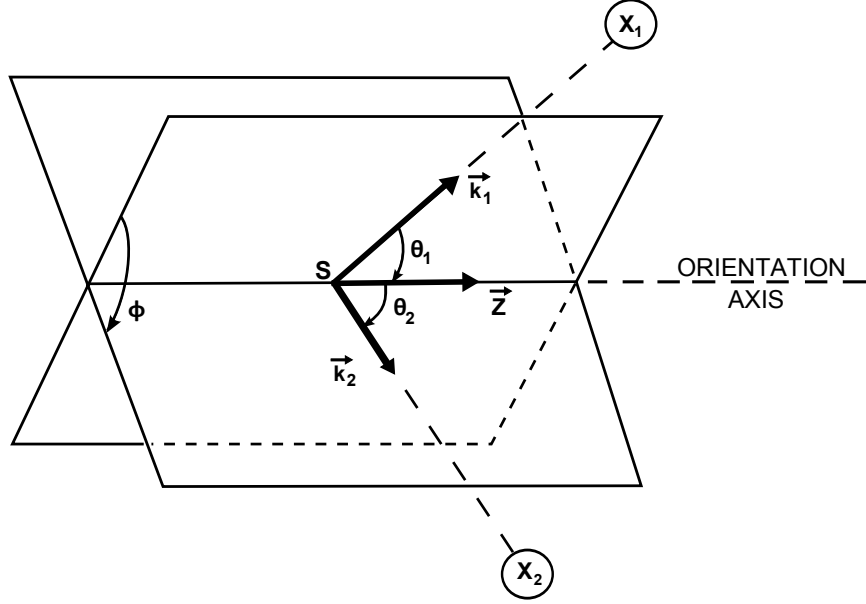


Figure 3.22. Diagram of the angles in a directional correlation of two successive radiations X_1 and X_2 emitted from an axial symmetric oriented source S .

$$H_{\lambda_1 \lambda_2} (\theta_1, \theta_2, \phi) = \sum_{q=-\lambda'}^{\lambda'} \frac{4\pi}{2\lambda_2 + 1} < \lambda_1 0 \lambda q | \lambda_2 q > Y_{\lambda q} (\theta_1, 0) Y_{\lambda_2 q}^* (\theta_2, \phi) \quad (3.36)$$

The orientation parameters $B_{\lambda_1} (I_1)$ take several different forms depending on the method used to orient the nucleus. For methods which result in an axially symmetric distribution where the nucleus has probability $P(m)$ to be in a given magnetic substate m , Eqn. 3.37 is used. For determining the orientation of the nucleus by observing a preceding gamma ray X_0 , Eqn. 3.38 is used.

$$B_{\lambda} (I_1) = \sqrt{2I_1 + 1} \sum_m (-1)^{I_1 + m} \times < I_1 - m I_1 m | \lambda 0 > P(m) \quad (3.37)$$

$$B_{\lambda} (I_1; X_0) = \frac{F_{\lambda}(L_0 L_0 I_0 I_1) + 2\delta F_{\lambda}(L_0 L'_0 I_0 I_1) + \delta^2 F_{\lambda}(L'_0 L'_0 I_0 I_1)}{1 + \delta^2} \quad (3.38)$$

In the case of a fusion-evaporation reaction, the probability function $P(m)$ is assumed to be of the form of a Gaussian distribution[121] which yields:

$$P(m, J, \sigma) = \frac{e^{-m^2/(2\sigma^2)}}{\sum_{m'=-J}^J e^{-m'^2/(2\sigma^2)}} \quad (3.39)$$

Here σ is the width of the distribution (thus $\sigma = 0$ corresponds to perfect alignment of the ensemble of nuclei), J is the spin of the initial state, and m is the substate index. σ is usually fit to be a function of the initial state's spin J in the form $\sigma = C * J$. The parameter C is usually in the range of 0.2 to 0.4 for typical fusion-evaporation reactions.

The directional distribution coefficients, generalized and otherwise, are defined as:

$$A_\lambda^{\lambda_2\lambda_1}(X_1) = \frac{F_\lambda^{\lambda_2\lambda_1}(L_1 L_1 I_2 I_1) + 2\delta F_\lambda^{\lambda_2\lambda_1}(L_1 L'_1 I_2 I_1) + \delta^2 F_\lambda^{\lambda_2\lambda_1}(L'_1 L'_1 I_2 I_1)}{1 + \delta^2} \quad (3.40)$$

$$A_{\lambda_2}(X_2) = \frac{F_\lambda(L_2 L_2 I_3 I_2) + 2\delta F_\lambda(L_2 L'_2 I_3 I_2) + \delta^2 F_\lambda(L'_2 L'_2 I_3 I_2)}{1 + \delta^2} \quad (3.41)$$

Here, the $F_\lambda^{\lambda_2\lambda_1}$ is the generalized F -coefficients and F_λ is the ordinary F -coefficients.

The F -coefficients are defined as:

$$\begin{aligned} F_\lambda^{\lambda_2\lambda_1}(LL'I_2I_1) &= [(2I_1+1)(2I_2+1)(2L+1)(2L'+1)(2\lambda+1) \\ &\times (2\lambda_1+1)(2\lambda_2+1)]^{1/2}(-1)^{L'+\lambda+\lambda_2+1} \\ &\times \left(\begin{array}{ccc} L & L' & \lambda \\ 1 & -1 & 0 \end{array} \right) \left\{ \begin{array}{ccc} I_2 & L & I_1 \\ I_2 & L' & I_1 \\ \lambda_2 & \lambda & \lambda_1 \end{array} \right\} \end{aligned} \quad (3.42)$$

$$F_\lambda(LL'I_2I_1) = F_\lambda^{0\lambda}(LL'I_2I_1) \quad (3.43)$$

Here (...) is the Wigner-3j symbol and {...} is the Wigner-9j symbol.

3.5.1 Angular Distributions

Angular distributions are the observation of the intensity distribution of single transitions relative to an orientation axis which has been set via a reaction or cryogenic methods. This is equivalent to saying that radiation X_2 was not observed which forces $\lambda_2 = 0$. Fortunately under this requirement, Eqn. 3.33 simplifies dramatically. The angular function $H_{\lambda_1 \lambda_2}(\theta_1, \theta_2, \phi)$ reduces to:

$$H_{\lambda_1 \lambda_0}(\theta_1, \theta_2, \phi) = P_\lambda(\cos[\theta_1]) \delta_{\lambda \lambda_1} \quad (3.44)$$

Here P_λ is the Legendre polynomial and $\delta_{\lambda \lambda_1}$ is the Kronecker delta function. Furthermore the directional coefficients reduce in complexity as well:

$$A_\lambda^{0\lambda_1}(X_1) = A_{\lambda_1}(X_1) \delta_{\lambda \lambda_1} \quad (3.45)$$

$$A_0(X_2) = 1 \quad (3.46)$$

Together this gives us the distribution function of [121], namely:

$$W(\theta) = \sum_{\lambda even} B_\lambda(I_1) A_\lambda(X_1) P_\lambda(\cos[\theta]) \quad (3.47)$$

With this the angular distribution of gamma ray relative to the beam axis is fitted with:

$$W(\theta) = A_0(1 + A_2 P_2(\cos[\theta]) + A_4 P_4(\cos[\theta]) \dots) \quad (3.48)$$

Here A_0 represents the normalized intensity obtained from peak areas in the gamma ray spectra. By analogy to Eqn. 3.47, the A_λ of the fit will depend on the orientation coefficient (and thus the degree of alignment), the spins of the original and final states, and the mixing ratio and multipolarity of the gamma ray. Typical ranges of values for various transitions can be seen in Table 3.5. For high efficiency

TABLE 3.5

TYPICAL VALUES OF ANGULAR DISTRIBUTION COEFFICIENTS
 A_2, A_4 FOR GAMMA-RAYS WITH DIPOLE (D), QUADRUPOLE (Q),
OR MIXED DIPOLE-QUADRUPOLE MULTIPOLARITY, L . TAKEN
FROM Ref. [106]

ΔI	L	Sign of A_2	Sign of A_4	A_2 Value	A_4 Value
2	Q	+	-	+0.3	-0.1
1	D	-		-0.2	0.0
1	D	-	+	-0.1	+0.2
1	D + Q	+/-	+	-0.8 to +0.5	0.0 to +0.2
0	D	+		+0.35	0.0
0	Q	-	-	-0.25	-0.25
0	D + Q	+/-	-	-0.25 to +0.35	-0.25 to 0.0

multi-detector arrays such as Gammsphere it is difficult, if not impossible, to extract gamma-ray intensities from singles spectra due to the high complexity of total measured spectra. However, Ref [58] gives a method by which spectra may be cleaned. By placing a quasi-isotropic gate on a transition(s) below the transition of interest the angular distributions information is preserved. Therefore it is possible to study angular distributions of gamma rays that are weak or contaminated in the singles spectra by gating on a gamma ray below them to increase the signal to noise ratio or to remove contamination.

3.5.2 DCO Ratios

In addition to angular distributions, ratios of the DCO function given in Eqn. 3.33 can be used to gather information about the nature of a transition[65]. A pair

of successive gamma-ray transitions is examined. These two gamma rays, γ_1 and γ_2 , are observed in detectors placed at θ_1 and θ_2 with respect to the beam axis. By examining the intensity of γ_2 in the detector at θ_1 from a gate on γ_1 in the detector at θ_2 and the intensity of γ_2 in the detector at θ_2 from a gate on γ_1 in the detector at θ_1 a ratio is determined which can be related to a ratio of the DCO function. It does not matter if the upper or lower transition of the pair of gamma rays is gated on, as long as the nature of the transition gated on is taken into account, the result will not change.

$$R_{DCO} = \frac{I_{\theta_1}^{\gamma_2}(Gate_{\theta_2}^{\gamma_1})}{I_{\theta_2}^{\gamma_2}(Gate_{\theta_1}^{\gamma_1})} \quad (3.49)$$

$$= \frac{W(\theta_2, \theta_1, \phi)}{W(\theta_1, \theta_2, \phi)} \quad (3.50)$$

In practice, these ratios are constructed for groups of detectors which requires integration of the numerator and denominators across the appropriate ranges of θ_1 , θ_2 , and ϕ . For Gammasphere the usual angle ranges for a DCO-ratio (R_{DCO}) are ($\theta \leq 50.1^\circ$ or $\theta \geq 129.9^\circ$), corresponding to the forward and backward ranges (“F/B”) (the DCO function is symmetric about 90°), and $69.8^\circ \leq \theta \leq 110.2^\circ$, corresponding to the approximately 90° range (“ $\sim 90^\circ$ ”). Another ratio that can be used is the so called “DCO-like” ratio (r). This ratio is constructed by examining the intensity of γ_2 in the detector at θ_1 from a gate on γ_1 in all detectors and the intensity of γ_2 in the detector at θ_2 from a gate on γ_1 in all detectors. These DCO-like ratios have a few benefits: the transition to be examined has greater intensity due to the more inclusive gate; the value is independent of the type of transition gated on; and they can distinguish between $\Delta I = 2$ pure quadrupole and $\Delta I = 0$ pure dipole transitions. Values of these ratios using the “F/B” range as θ_2 and the “ $\sim 90^\circ$ ” range as θ_1 can be found in Table 3.6.

TABLE 3.6

TYPICAL VALUES OF DCO RATIOS (R_{DCO}) AND DCO-LIKE RATIOS
(r) FOR THE GAMMASPHERE ARRAY. ADAPTED FROM REF. [28]

ΔI	L	$R_{DCO}, \Delta I = 1$ pure dipole gate	$R_{DCO}, \Delta I = 2$ quadrupole gate	$r(\text{any gate})$
2	Q	1.6	1.0	1.2
1	D	1.0	0.6	0.8
0	D	1.6	1.0	1.3
1	D + Q	$0.5 < R_{DCO} < 1.9$	$0.3 < R_{DCO} < 1.2$	$0.4 < r < 1.5$
0	D + Q	$1.1 < R_{DCO} < 1.7$	$0.6 < R_{DCO} < 1.1$	$0.8 < r < 1.3$

R_{DCO} and r are typically used to distinguish stretched quadrupole transitions from stretched dipole. For many pure or nearly pure transitions this is sufficient. However, in the case of transitions that are admixtures of two multipole components, the ratios can take on a broad range of values. This sometimes renders unambiguous determination of spins impossible without additional information.

3.5.3 Polarization

A transition can have a polarization of either electric or magnetic nature, giving rise to EL and ML transitions, if L is even electric transitions leave the parity of the nucleus unchanged and magnetic transitions change the parity. If L is odd, this is reversed. The polarization of a transition can be measured via the scattering asymmetry [107]:

$$A = \frac{a(E_\gamma)N_\perp - N_\parallel}{a(E_\gamma)N_\perp + N_\parallel} \quad (3.51)$$

Here N_{\perp} and N_{\parallel} are the number of coincidence counts between segments of a clover detector in the direction perpendicular and parallel to the emission plane, respectively (the emission plane defined by the beam axis and the gamma ray emission direction). The parameter $a(E_{\gamma})$ is the correction for any natural asymmetry in the response of the clover segments as a function of gamma-ray energy. This correction is defined as:

$$a(E_{\gamma}) = \frac{N_{\parallel}(\text{unpolarized})}{N_{\perp}(\text{unpolarized})} \quad (3.52)$$

As a radioactive source has no spin alignment, it can serve as a source of unpolarized gamma-rays for measuring this value. For the INGA experiment this natural asymmetry was measured using the energy calibration data; Fig. 3.23 has a plot of the extracted natural asymmetries and the linear fit to them (as in Ref. [107]. The

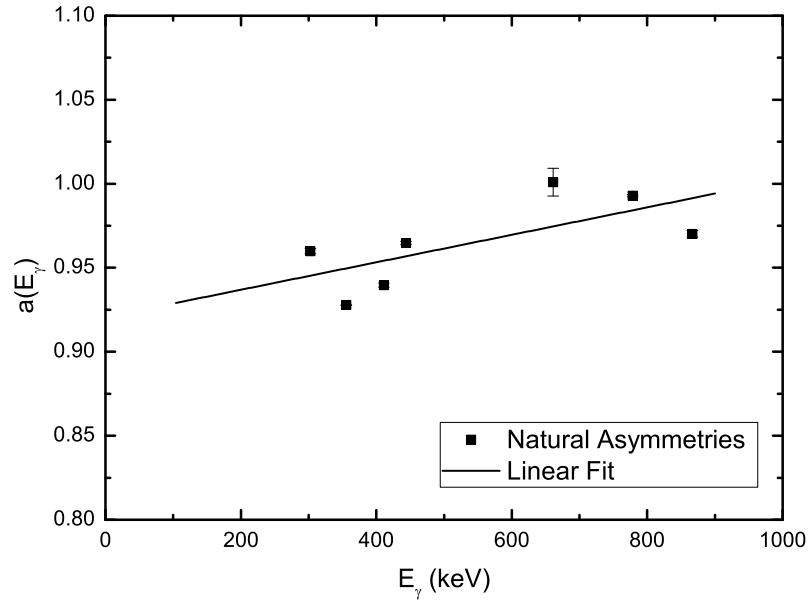


Figure 3.23. Natural asymmetries and the linear fit to them.

linear fit was:

$$a(E_\gamma(\text{keV})) = 0.92 \pm 0.02 + (8.2 \pm 3.7 \times 10^{-5}) E_\gamma \quad (3.53)$$

With the fit to the natural asymmetries, calculation of the polarization asymmetry A can proceed. If $A > 0$ the transition in question is predominantly electric in nature; if $A < 0$ the transition is predominantly magnetic in nature.

CHAPTER 4

TRANSVERSE WOBBLING IN ^{135}Pr

4.1 Level Scheme of ^{135}Pr

Previously T.M. Semkow *et al.* performed a spectroscopic study of ^{135}Pr [103] using an array consisting of four HPGe detectors with NaI escape suppression, two

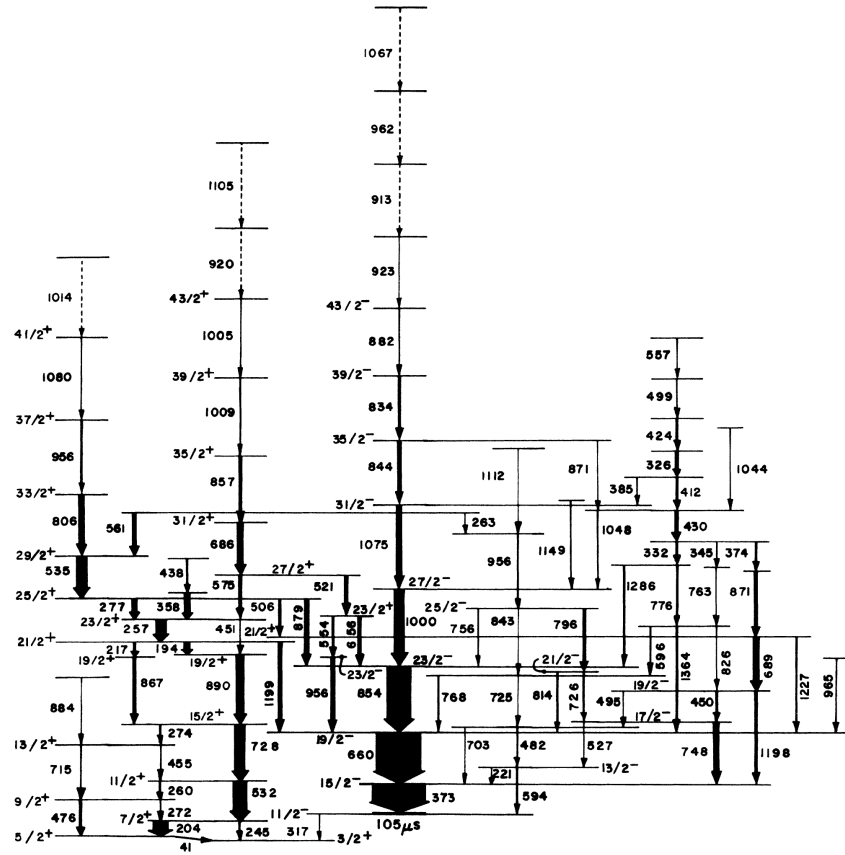


Figure 4.1. Previous level scheme for ^{135}Pr , from Ref. [103].

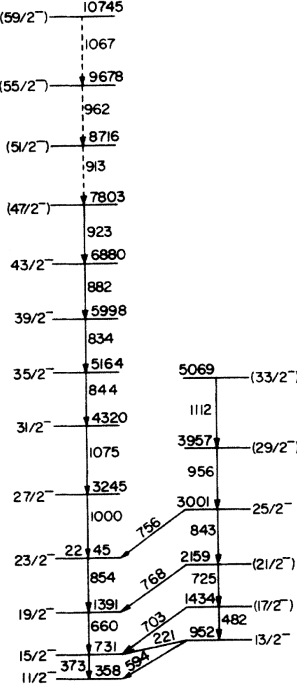


Figure 4.2. Negative parity rotational band structure proposed for ^{135}Pr in Ref. [103].

unsuppressed HPGe detectors, and eleven NaI counters (to provide gamma-ray multiplicity selection). In this experiment $1.66 \times 10^8 \gamma\text{-}\gamma$ coincidence events were collected. Using this data, the level scheme in Fig. 4.1, showing both positive and negative parity levels, was developed. As the positive parity portion of the level scheme is of little interest to the wobbling excitation in ^{135}Pr , it is neglected in the rest of the discussion in this work. In Ref. [103] rotational band structures for the positive and negative parity parts of the level scheme were proposed; Fig. 4.2 contains the proposed negative parity rotational band structure. Additional work, extending the yrast band to $^{91/2-}$, was performed by E.S. Paul *et al.* [90]. The data for the work in Ref. [90] was a byproduct of a high statistics measurement of ^{134}Pr done at Gammasphere. Fig. 4.3 contains the proposed yrast structure.

Data from the Gammasphere experiment, described in 3.3, were sorted into sym-

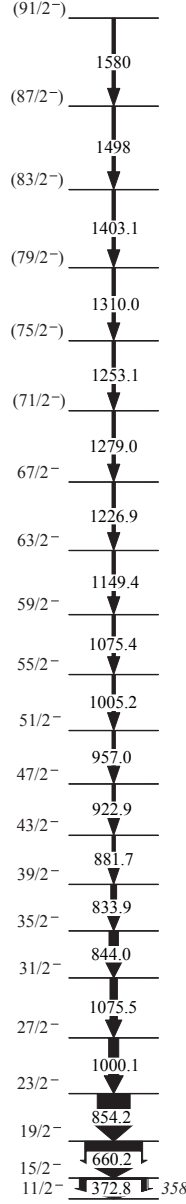


Figure 4.3. Yrast band for ^{135}Pr presented in Ref. [90].

metrized cubes (E_{γ} - E_{γ} - E_{γ}) and hypercubes (E_{γ} - E_{γ} - E_{γ} - E_{γ}) using the RADWARE suite of codes [94]. Background-subtracted, gated spectra were obtained using the RADWARE suite coupled with the background subtraction algorithm of Ref. [95]. The smooth backgrounds used for this algorithm are shown in Fig. 4.4. Coincidence relations from this data were used to construct the level scheme.

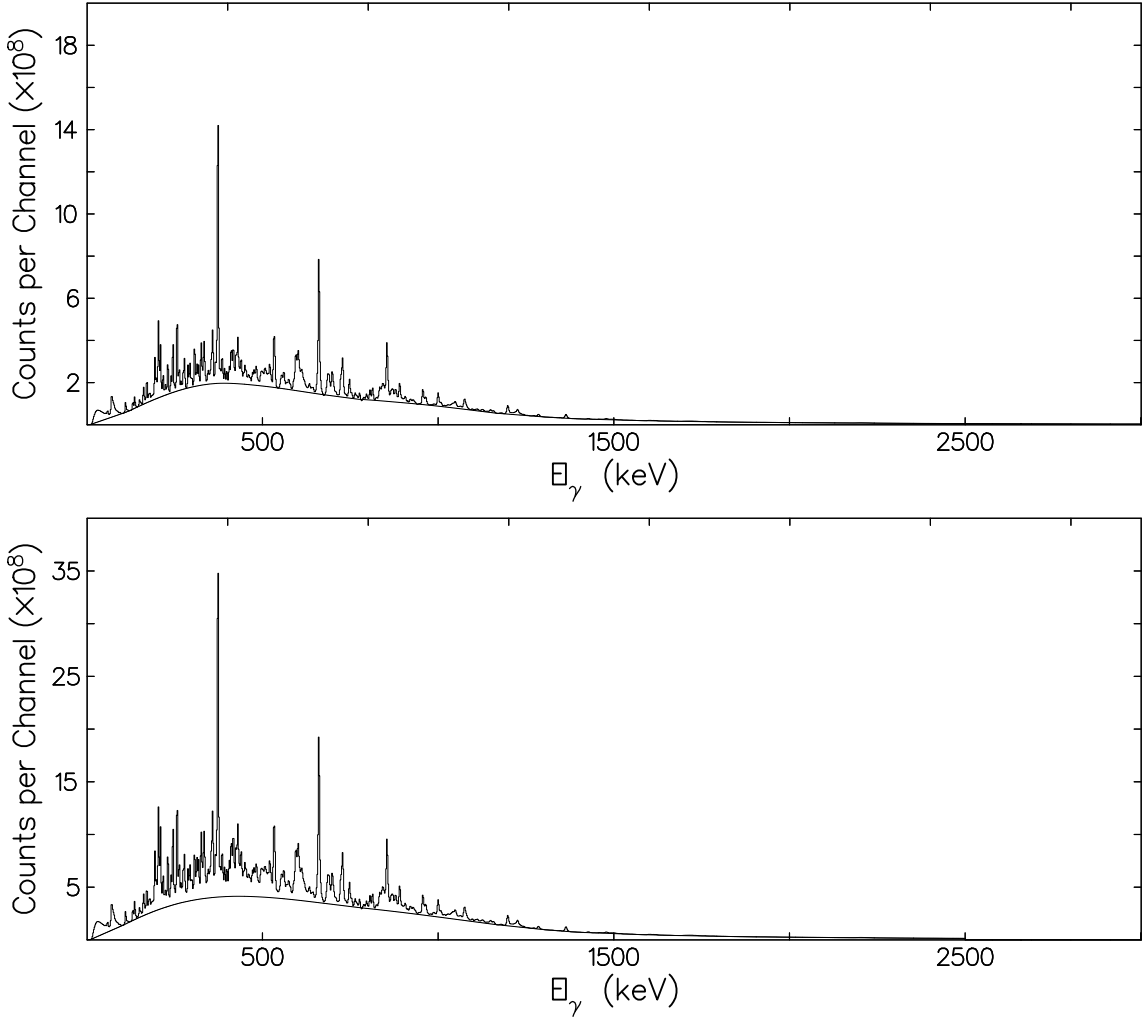


Figure 4.4. Top: Background spectrum for the symmetrized cube. Bottom: Background spectrum for the symmetrized hypercube.

The negative parity level scheme constructed from the Gammasphere data in this work is presented in Fig. 4.5. Tables of level and transition information are found in Appendix C. As the beam and target combination were tuned to preferentially excite non-yrast states, the yrast band was only measured to spin $^{51}/2$. The findings of this measurement were in agreement with Ref. [90]. However, the band structure proposed in Ref. [103] disagreed with the results found in this work. Notably, the signature partner transitions above the $^{25}/2$ level were found to belong to the $n_w = 1$

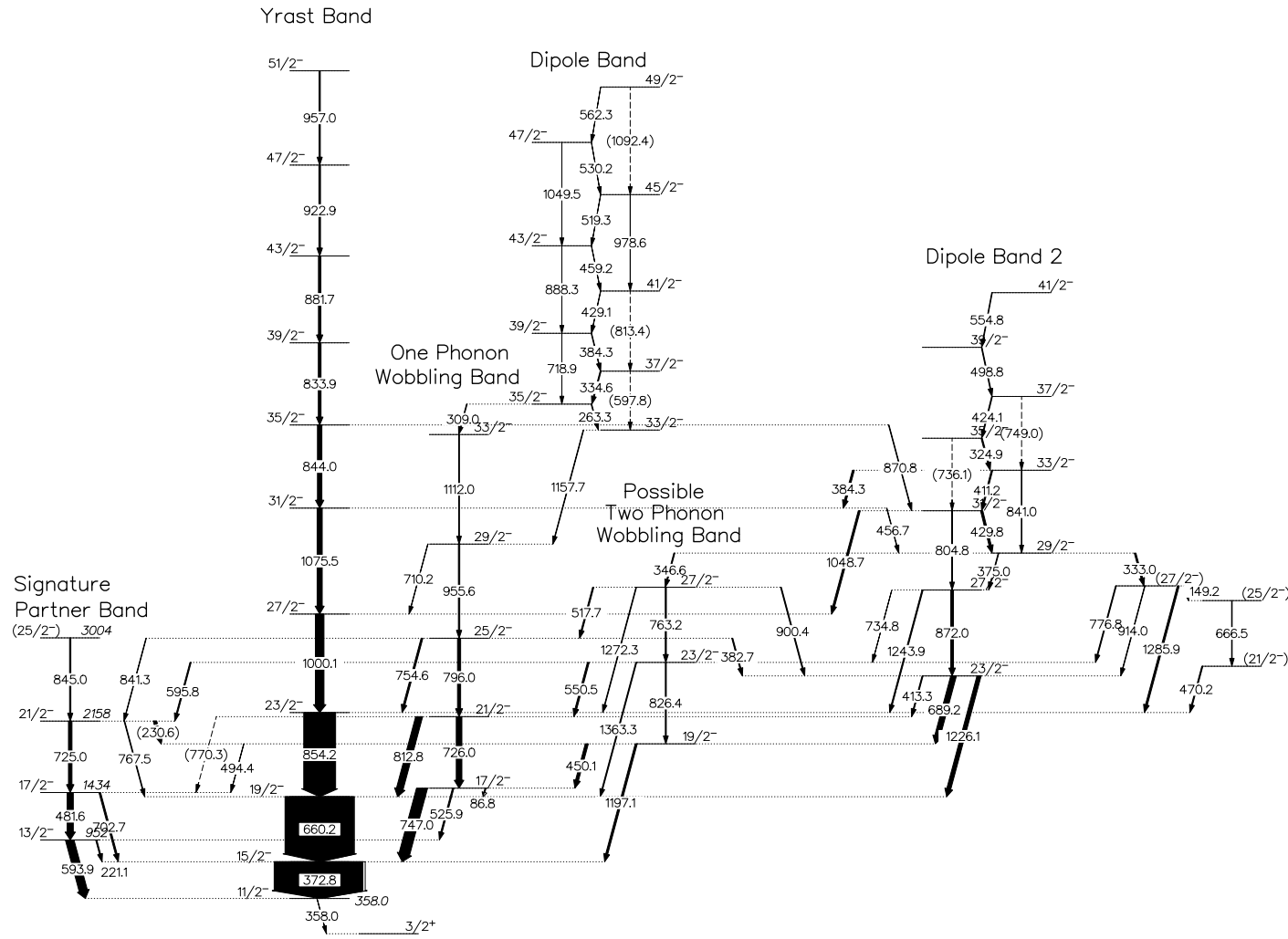


Figure 4.5. Negative parity level scheme developed for ^{135}Pr .

wobbling band. It seems that in the work presented in Ref. [103] it had not been possible to resolve the difference between the last 845.0 keV transition of the signature partner band and the 841.3 keV transition linking the $n_w = 1$ wobbling band to the signature partner band. Evidence for this is given in Figs. 4.6 and 4.7. Fig. 4.6 shows the sum of the spectra resulting from every possible double gate on the dipole band. This spectrum shows the dominance of decay through the wobbling band as opposed to the signature partner band. Fig. 4.7 shows a triple gate placed on the $n_w = 1$ band and the dipole band immediately above the weak linking transition from the wobbling band to the signature partner band. Here the difference in the 841.3 keV transition's strength and the strength of the 796.0 keV transition is plainly visible. This disparity in strength further highlights that the primary decay path from the $^{25}/2$ is through the 796.0 keV transition, in keeping with its being an intraband transition.

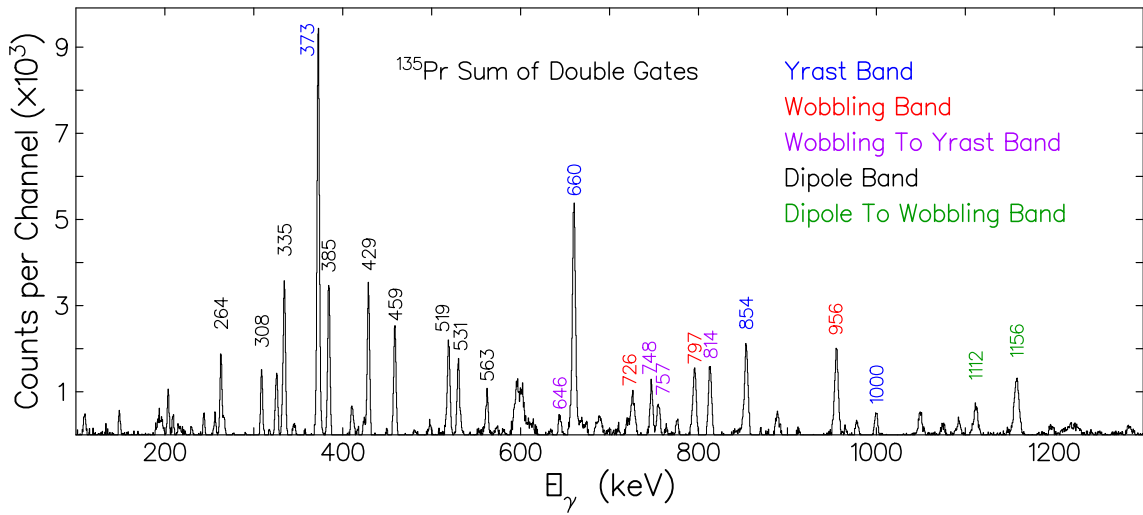


Figure 4.6. Sum of all possible double gates on M1 transitions in the dipole band. The labeling of the transitions is color coded according to the band the transition belongs to.

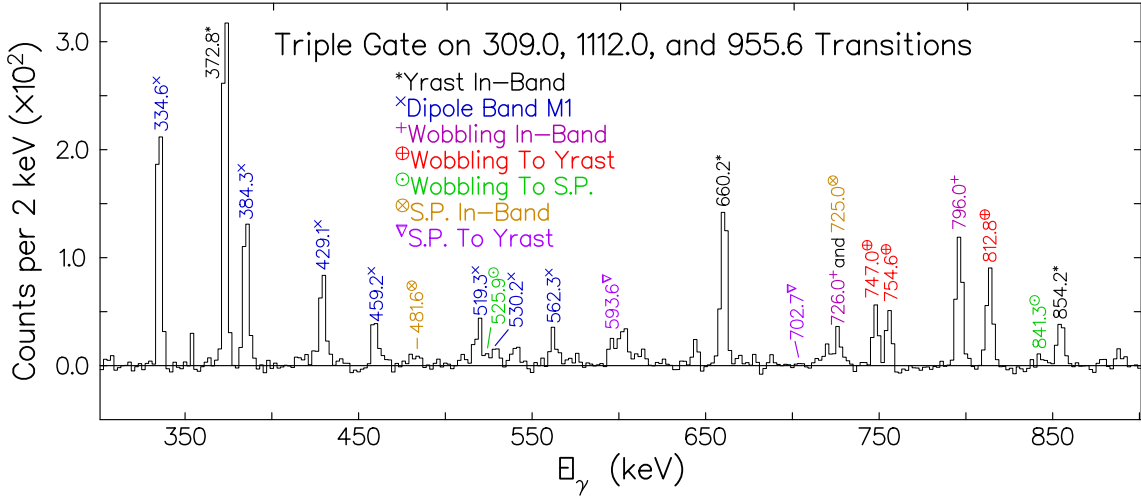


Figure 4.7. Triple gate on the specified transitions. The labeling of the transitions is color coded according to the band to which a transition belongs.

Spins were assigned with the following techniques: angular distributions (method discussed in section 3.5.2), DCO-like ratios (method discussed in section 3.5.2), and arguments from the deexcitation of the level to multiple levels. Assignments using the first two methods are discussed in section 4.1.1; however as the third method relies purely on coincidence data and previously known components of the level scheme, it will be addressed here.

The dipole and quadrupole transitions of Dipole Band 1 and Dipole Band 2 were assigned based on their placement. As each dipole transition (strong low energy transitions) had a cross-over transition the following reasoning was used. A cross-over transition must have a low-order multipolarity (L) equal to the sum of the low-order multipolarities of the two transitions it crosses. Therefore a crossover of $E2$ nature is only possible if the two crossed transitions are both dipole. If one or both of the crossed transitions is of higher order, then the crossing transition must be of higher

order as well. Given the very low probability (slow) nature of most transitions with $L > 2$, observation of the cross-over strongly implies that the cross-over must be $E2$ and the crossed transitions $M1$. It is possible for the crossed transitions to be $E1$ in nature; however if this were the case, then the dipole transitions would not be part of a single band but instead would be connecting two bands, one of positive parity and one of negative. It can be argued that this is not the case because: if half of each of the dipole bands was positive parity, then the dipole bands should have strong links to other positive parity states, which is not the case. The dipole bands have very few or no connections to the positive parity states and numerous strong connections to the negative parity states. Though the top of Dipole Band 2 had cross-over transitions that were too weak to measure, the observation of lower cross-over transitions and their rapidly fading strength gave confidence in the band continuing to be composed of $M1$ transitions.

The spin of dipole band 2 was fixed relative the yrast band using the four interband transitions that link the states around $^{31}/2$ of the two bands. The pattern of linking that occurred is typical of levels that happened to mix because they were very close in energy and had the same spin and parity. Additionally if the two apparently overlapped states were separated by one unit of angular momentum, then either the 870.8 keV transition or the 1048.7 keV transition would have $L = 3$, rendering it highly unlikely. Unfortunately this argument does not cover the $^{23}/2$ state of dipole band 2. This state's spin was fixed by the following arguments: if the state were instead $^{21}/2$ then the 872.0 keV transition would be an improbable $L = 3$; while if it were $^{25}/2$ then the 689.2 keV and 1226.1 keV transitions would both be $L = 3$, again unlikely. The spin of the signature partner band $^{21}/2$ level is fixed as follows. If the level were instead $^{19}/2$, the 841.3 keV transition into it would be $L = 3$ in nature. Alternatively if the level were $^{23}/2$, then the 725.0 keV transition out of it would be $L = 3$. Finally the spin of the possible $n_w = 2$ band, $^{27}/2$ state was fixed as follows:

If the level were $^{29}/2$, then 1272.3 keV transition would be $L = 3$. The impossibility of the level being $^{25}/2$ is supported by the fact that the 517.7 keV transition would be $L = 0$ which would be highly converted and difficult to see with gamma spectroscopy.

4.1.1 Angular Distributions and DCO-like Ratios

The first step in determining if a band is an $n_w = x$ wobbling band is to look at transitions from $n_w = x$ to $n_w = (x - 1)$. For the case studied in this work, $x = 1$. As stated earlier these transitions must have $\Delta I = 1, E2$ nature. To determine if this holds true, angular distributions of the transitions must be extracted and fitted.

Angular distributions for the first three transitions from $n_w = 1 \rightarrow n_w = 0$ are plotted in the top left, top right, and middle left panels of Fig. 4.8. Each panel contains the extracted angular distribution data, a plot of the fit to the data, and plots of the distributions for pure transitions of higher and lower order. As seen in the figures, the angular distributions for the $n_w = 1 \rightarrow n_w = 0$ transitions are strongly mixed with the higher order. This shows that the transitions are $\Delta I = 1, L = 2$. While it is highly probable that the polarization of the transition is E , to guarantee that the transition is $E2$, polarization measurements are necessary. The middle right panel of Fig. 4.8 holds the angular distribution of the first transition from the band identified as a possible $n_w = 2$ band to the $n_w = 1$ band. As seen in the figure, this distribution is also highly mixed. This is a hopeful sign that the band is in fact the $n_w = 2$ band.

To ensure that the signature partner to yrast transitions are of substantially different character, the angular distribution of the first signature partner to yrast transition was extracted, shown in the bottom left panel of Fig. 4.8. Examination of this transition shows that it is less than 3% $E2$, as expected of signature partner to yrast transition. As an additional check on the angular distribution extraction and fitting procedure, the angular distribution of the fifth yrast in-band transition

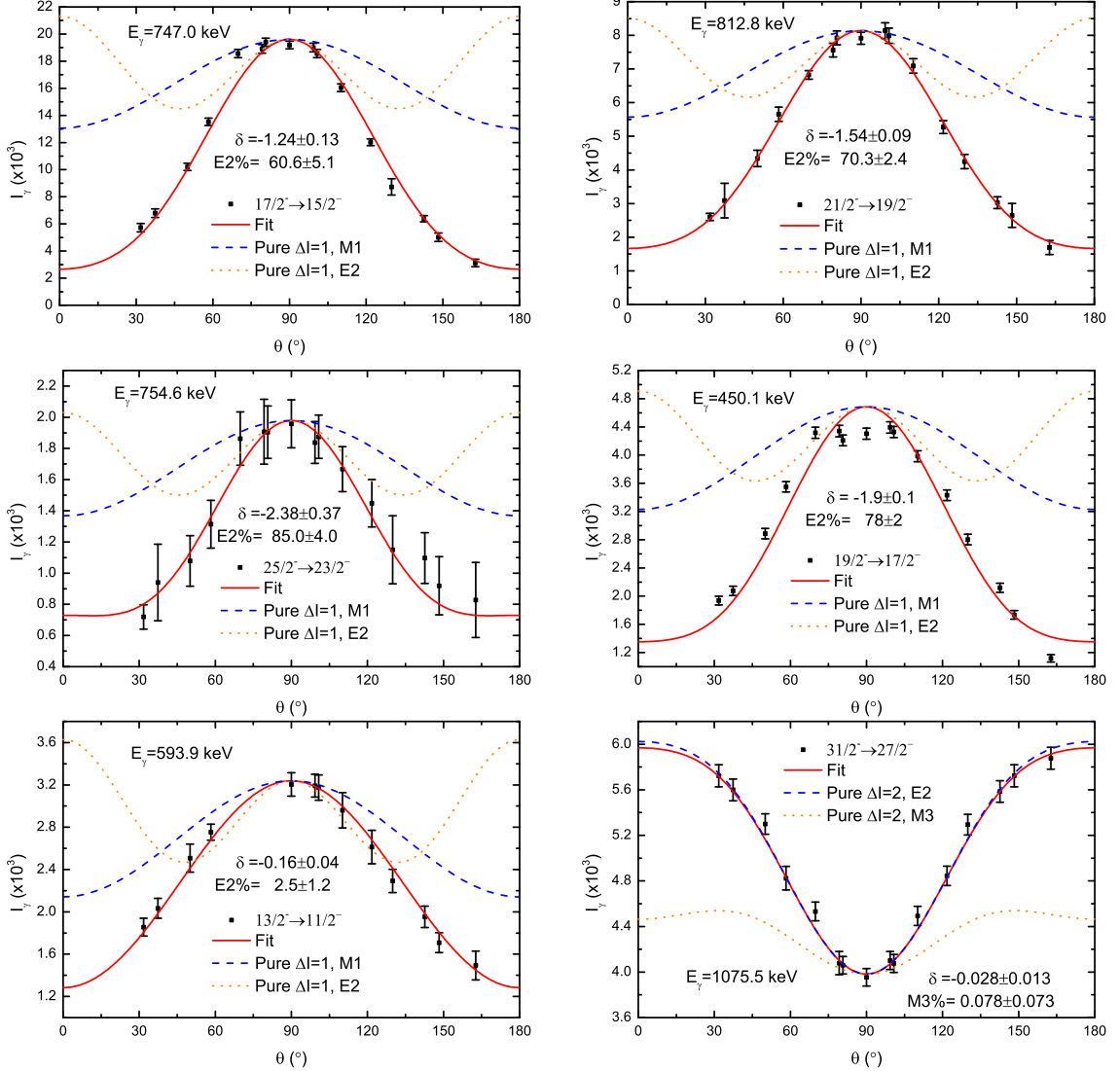


Figure 4.8. Important angular distributions fitted in this work. Top Left: The first $n_w = 1 \rightarrow n_w = 0$ transition (747.0 keV). Top Right: The second $n_w = 1 \rightarrow n_w = 0$ transition (812.8 keV). Mid Left: The third $n_w = 1 \rightarrow n_w = 0$ transition (754.6 keV). Mid Right: The first possible $n_w = 2 \rightarrow n_w = 1$ transition (450.1 keV). Bottom Left: The first signature partner to yrast transition (593.9 keV). Bottom Right: The fifth yrast in-band transition (1075.5 keV).

(1075.5 keV) is presented on the bottom right. As its nature is $\Delta I = 2, E2$, substantially different from the transitions fitted previously, flaws in the procedure that may be hidden for $\Delta I = 1$ transitions should be more easily visible. This check revealed

no issues, as shown in the bottom right panel of Fig. 4.8. As expected the transition was found to be pure $E2$ in nature.

Angular distributions provide a highly detailed examination of a transition's multipolarity; however because any gates used to clean the resultant spectra must be placed below the transition of interest and because the intensity of the transition is distributed across many rings, they can be difficult and time consuming to extract. As mentioned in section 3.5.2, DCO-like ratios are a convenient method for extracting the multipolarity of the distribution. It is much harder to get a good limit on the mixing ratio δ with this method; however, in cases where the mixing ratio is unnecessary, the higher intensity and fewer values to fit and extract make the DCO-like ratio a very useful method to extract transition multipolarity. Table 3.6 gives the values of the DCO-like ratio associated with each multipolarity.

Fig. 4.9 contains a plot of many of the DCO ratios measured for this nucleus. The 372.8 keV and 660.2 keV transitions of the yrast band, known to be very pure quadrupole transitions, have values slightly lower than expected for a combination of two reasons. The first is that these transitions are so intense that their peaks become very hard to fit due to strange contributions of width from detectors at different angles to the beam axis. The second reason is that the DCO-like ratios presented in Table 3.6 and illustrated in Fig. 4.9 were computed for a substate distribution width of $\sigma = 0.3J_i$. While this is quite close to true (and thus a reasonable approximation) for transitions above the 372.8 keV transition, this approximation breaks down somewhat at the lower spin where the substate distribution width drops to $\sigma = 0.23J_i$. Nevertheless the values are still in decent agreement with quadrupole transitions.

Examination of Fig. 4.9 reveals that the DCO-like ratios of the $n_w = 1 \rightarrow n_w = 0$ transitions are as expected of highly mixed transitions with negative mixing ratio. Further the DCO-like ratio for the 710.2 keV transition was extracted and shown to be highly mixed, confirming the trend established in the previous $n_w = 1 \rightarrow n_w = 0$

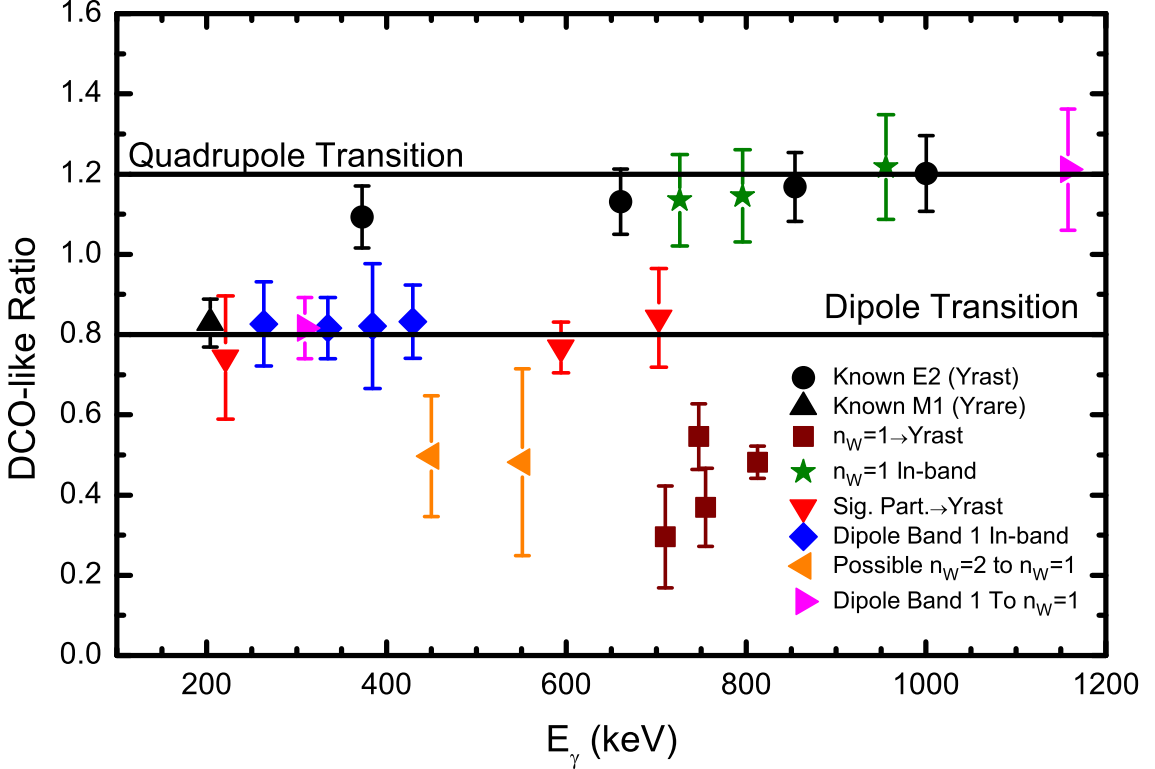


Figure 4.9. DCO-like ratios plotted versus transition energy for a wide variety of transitions in ^{135}Pr .

transitions. Additionally the DCO-like ratio of the first possible $n_w = 2 \rightarrow n_w = 1$ transition confirms the angular distribution and the ratio of the second possible $n_w = 2 \rightarrow n_w = 1$ transition shows the trend of highly mixed possible $n_w = 2 \rightarrow n_w = 1$ transitions continuing.

With the angular distributions and DCO-like ratios, the spins of the $n_w = 1$ band, $n_w = 2$ band, signature partner band, and dipole band 1 can be fixed relative to the yrast spins. The DCO ratios of the 309 keV transition and the 1157.7 keV transitions from dipole band 1 to the $n_w = 1$ band firmly lock its spin relative to the wobbling band. In turn the angular distributions and the DCO-like ratios of the $n_w = 1 \rightarrow n_w = 0$ transitions lock the wobbling band relative to the yrast band. The DCO-like ratios and angular distributions of the signature partner to

yrast band transitions lock the spins of the signature partner states relative to the yrast band. The final set of spins, of the possible $n_w = 2$ band, are fixed by the angular distribution of the bottom transition to the $n_w = 1$ band, by the DCO-like ratios of the bottom and middle transition to the $n_w = 1$ band, and finally by the arguments given in the last paragraph of section 4.1.

4.1.2 Polarizations

It is highly probable that the polarization of the $n_w = 1 \rightarrow n_w = 0$ transitions is electric in nature; however to guarantee this, it is necessary to measure polarizations. As described in section 3.5.3 polarizations of transitions can be extracted using arrays of clover-type HPGE detectors. To this end an experiment was performed at the INGA array [80, 81] located at the Tata Institute for Fundamental Research in Mumbai, India.

The data from this experiment were sorted into two asymmetric matrices (E_γ - E_γ) using the code MARCOS [87]. The first of these matrices consisted of all gamma-ray events where at least one of the gamma rays scattered perpendicular to the reaction plane on the y-axis and the other gamma energy (with no restrictions) on the x-axis. The second of these matrices consisted of all gamma-ray events where at least one of the gamma rays scattered parallel to the reaction plane on the y-axis. With these matrices and the correction to the asymmetry due to the geometry of the array (denoted a , see section 3.5.3 for details), asymmetries for transitions can be extracted. If the asymmetry is positive, then the transition had electric nature; contrariwise if the transition has magnetic nature, then the asymmetry is negative.

Due to the thick target and poorer statistics of the INGA experiment relative to the Gammasphere experiment, it was possible to extract polarization asymmetries for only the bottom two $n_w = 1 \rightarrow n_w = 0$ transitions. Despite this, these asymmetries show that the transitions are definitely electric in nature, confirming the $\Delta I = 1, E2$

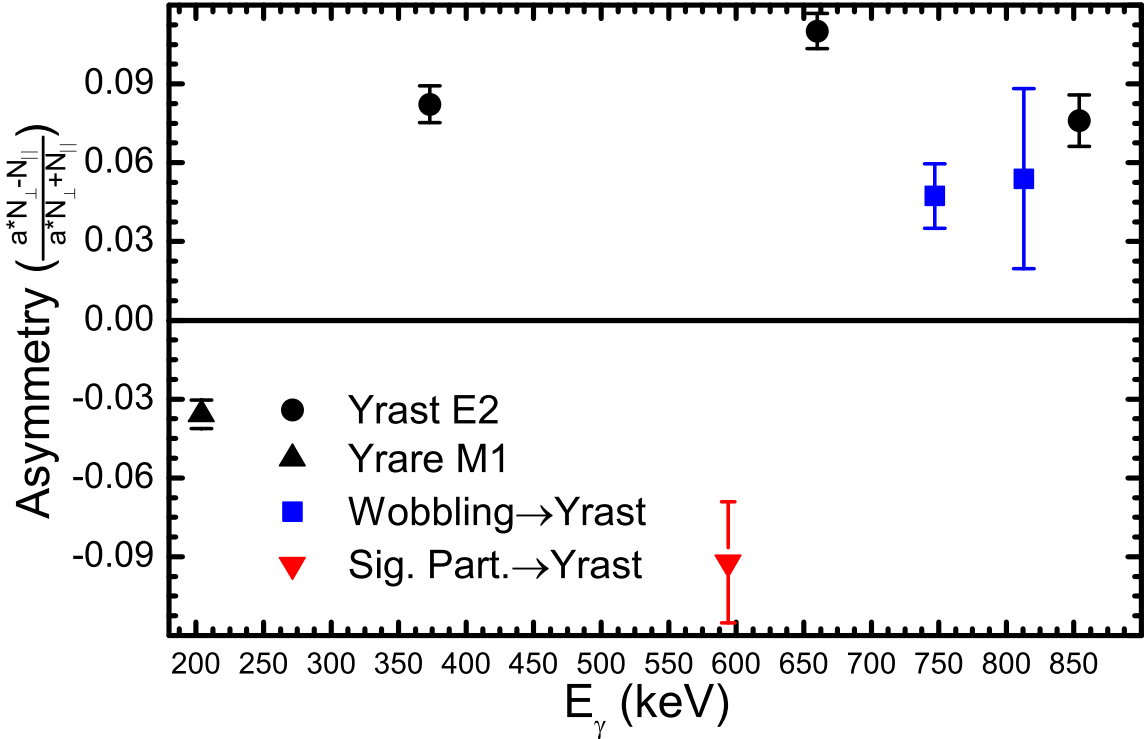


Figure 4.10. Polarization asymmetries versus transition energy for several transitions in ^{135}Pr .

nature of the transitions. Given this the $n_w = 1$ wobbling band is confirmed and the case is strong for the possible $n_w = 2$ wobbling band. The angular distribution and polarization asymmetry results for the $n_w = 1$, possible $n_w = 2$, and signature partner bands are summarized in Table 4.1. This table contains the polarization asymmetries, mixing ratios, and $E2$ percentages for the wobbling transitions and the bottom most signature partner to yrast band transitions.

4.2 Description by Theory

Theoretical calculations within the framework of the QTR and TAC models to describe the $n_w = 1$ band, the signature partner band, dipole band 1, and the yrast band in ^{135}Pr were performed by S. Frauendorf and F. Dönau in Ref. [41]. Updated

TABLE 4.1

TABLE OF EXTRACTED MIXING RATIOS, POLARIZATION ASYMMETRIES, AND $E2$ PERCENTAGES FOR THE $n_w = 1$, POSSIBLE $n_w = 2$, AND SIGNATURE PARTNER BANDS.

Initial I^π	E_γ (keV)	δ	Asymmetry	% E2	DCO-like
$\frac{17}{2}^-$	747.0	-1.24 ± 0.13	0.047 ± 0.012	60.6 ± 5.1	0.546 ± 0.082
$\frac{21}{2}^-$	812.8	-1.54 ± 0.09	0.054 ± 0.034	70.3 ± 2.4	0.482 ± 0.040
$\frac{25}{2}^-$	754.6	-2.38 ± 0.37	—	85.0 ± 4.0	0.369 ± 0.098
$\frac{29}{2}^-$	710.2	—	—	—	0.296 ± 0.127
$\frac{19}{2}^-$	450.1	-1.54 ± 0.09	—	78 ± 2	0.50 ± 0.15
$\frac{23}{2}^-$	550.5	—	—	—	0.48 ± 0.23
$\frac{13}{2}^-$	593.9	-1.90 ± 0.1	-0.092 ± 0.023	2.5 ± 1.2	0.77 ± 0.06
$\frac{13}{2}^-$	221.1	0.23 ± 0.03	—	5.0 ± 1.2	0.74 ± 0.15
$\frac{17}{2}^-$	702.7	—	—	—	0.84 ± 0.12

calculations were performed by S. Frauendorf and W. Li in Ref. [72]. Experimental level energies, wobbling energies, and reduced transition probability ratios were compared against these calculations.

For the QTR calculations the triaxial rotor is parameterized by three angular momentum dependent moments of inertia (MOI) with the form $\mathcal{J}_i = \Theta_i(1 + cI)$ with $i = m, s, l$, denoting the medium, short, and long axes, respectively. Adjusting the QTR energies to the experimental energies of the yrast and $n_w = 1$ bands, the parameters used were $\mathcal{J}_m, \mathcal{J}_s, \mathcal{J}_l = 7.4, 5.6, 1.8\hbar/MeV$ and $c = 0.116$. The QTR model was then used to calculate state energies, wobbling energies, and reduced transition probability ratios. Fig. 4.11 contains a plot of the wobbling energy calculated from

the QTR model compared against the experimental wobbling energy. Fig 4.12 contains a plot of QTR and experimental level energies with a $0.02 \times I(I+2)$ rigid rotor component subtracted. A list of experimental and QTR reduced transition probability ratios is found in Table 4.2. A plot of the experimental and theoretical values of $B(M1_{out})/B(E2_{in})$ is found in the left panel of Fig. 4.13; the corresponding plot for $B(E2_{out})/B(E2_{in})$ is found in the right panel. Experimental reduced transition probability ratios are calculated using the formula from Ref. [88]:

$$\frac{B(M1_{out})}{B(E2_{in})} = 0.697 \frac{E_\gamma(E2_{in})^5}{E_\gamma(M1_{out})^3} \frac{1}{(1+\delta^2)\lambda_{E2_{in}/M1_{out}}} \quad (4.1)$$

$$\frac{B(E2_{out})}{B(E2_{in})} = \frac{E_\gamma(E2_{in})^5}{E_\gamma(E2_{out})^5} \frac{\delta^2}{(1+\delta^2)\lambda_{E2_{in}/E2_{out}}} \quad (4.2)$$

Here $\lambda_{X1/X2}$ is the branching ratio, or intensity ratio of the transition ($X1$) to the transition ($X2$) and δ is the mixing ratio extracted from an angular distribution measurement.

As shown in Fig. 4.11, the QTR model reproduces the experimental data well showing the minimum in E_{wobb} at $I^\pi = {}^{29/2} -$ and the subsequent upturn. This upturn is due to the Coriolis force detaching the quasiproton from the short axis and aligning it to the intermediate axis, switching the system from transverse to longitudinal wobbling. Regrettably QTR does not reproduce the size of the upturn seen in experiment; because simultaneous to the realignment in the wobbling band, the yrast band is undergoing a transition from a $\pi h_{11/2}$ configuration to a $\pi(h_{11/2})^3\nu(h_{11/2})^2$ configuration (in agreement with Ref. [90]). The level energies in Fig. 4.12 for the yrast and wobbling bands are in good agreement with experiment, but the theory predicted signature partner band $\sim 0.5\text{MeV}$ above its experimental counterpart. TAC calculations, discussed in more detail shortly, reproduce the signature partner band well.

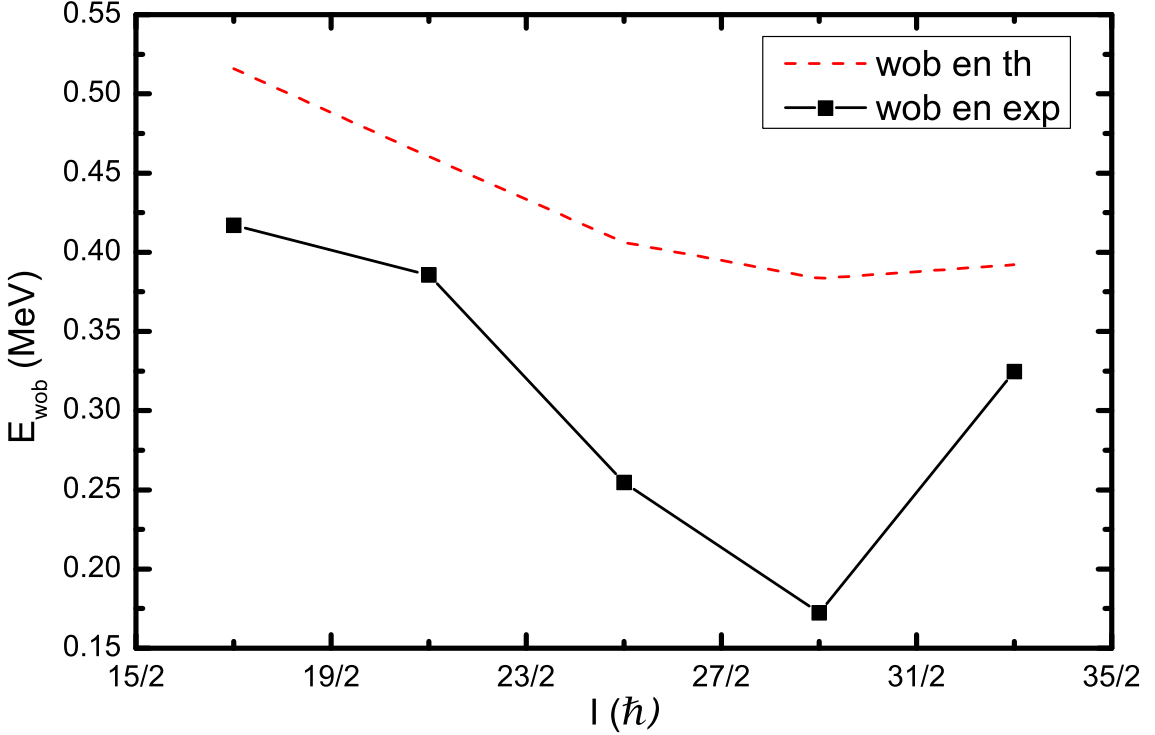


Figure 4.11. Wobbling energies from experiment and QTR theory of the $n_w = 1$ band. Error bars for energies are not plotted as they are smaller than the plotted points.

TAC calculations were carried out for the one quasiparticle $\pi h_{11/2}$ yrast band, the five quasiparticle $\pi(h_{11/2})^3\nu(h_{11/2})^2$ yrast band, and the three quasiparticle $\pi(h_{11/2})\nu(h_{11/2})^2$ dipole band 1. For the one quasiparticle yrast band, pair gaps of $\Delta_p = 1.1$ MeV and $\Delta_n = 1.0$ MeV were used and the equilibrium deformation parameters obtained were $\epsilon = 0.16$ and $\gamma = 26^\circ$. For the three quasiparticle dipole band 1 and the five quasiparticle yrast band, pair gaps of $\Delta_p = 0$ MeV and $\Delta_n = 0.8$ MeV were used and the equilibrium deformation parameters obtained were $\epsilon = 0.20$ and $\gamma = 28^\circ$. The corresponding MOI of the $\pi(h_{11/2})$ yrast band are then $\mathcal{J}_m, \mathcal{J}_s, \mathcal{J}_l = 19, 8, 3\hbar/\text{MeV}$. A QTR calculation using these MOI shows the early collapse of the wobbling band; this is avoided using the fitted MOI for the QTR model. A plot of the energy levels calculated through the TAC model and those from experiment is in

Fig. 4.14.

4.3 Discussion

TAC and QTR calculations were performed to describe the behavior of the yrast band, $n_w = 1$ band, the signature partner band, and dipole band 1 of the nucleus ^{135}Pr . As seen in Table 4.2 and the right panel of Fig. 4.13, the QTR model predicts a strong unstretched $E2$ component, dominating the $M1$ part, for $n_w = 1 \rightarrow n_w = 0$ transitions. But the calculations under-predict the $B(E2_{out})$ transition probabilities and somewhat overestimate the $B(M1_{out})$ transition probabilities. Additionally QTR predicts the signature partner band which exhibits

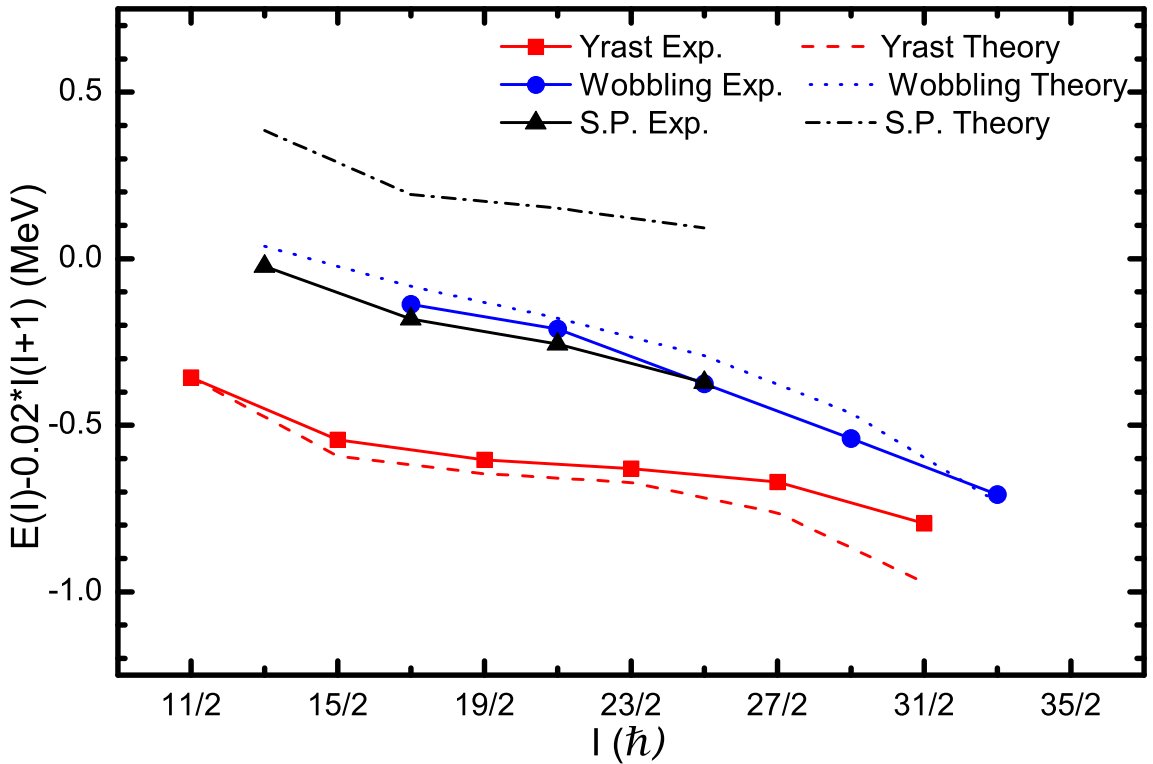


Figure 4.12. Level energy minus a rigid rotor component from experiment and QTR theory for the yrast, wobbling, and signature partner bands. Error bars for energies are not plotted as they are smaller than the plotted points.

TABLE 4.2

TABLE OF REDUCED TRANSITION PROBABILITIES CALCULATED
FROM DATA AND FROM QTR THEORY FOR THE $n_w = 1 \rightarrow n_w = 0$
TRANSITIONS.

Initial I^π	E_γ (keV)	$\frac{B(M1_{out})}{B(E2_{in})} \left(\frac{\mu_N^2}{e^2 b^2} \right)$		$\frac{B(E2_{out})}{B(E2_{in})}$	
		Experiment	QTR	Experiment	QTR
$\frac{17}{2}^-$	747.0	—	0.213	—	0.908
$\frac{21}{2}^-$	812.8	0.164 ± 0.014	0.107	0.843 ± 0.032	0.488
$\frac{25}{2}^-$	754.6	0.035 ± 0.009	0.070	0.500 ± 0.025	0.290
$\frac{29}{2}^-$	710.2	$\leq 0.016 \pm 0.004$	0.056	$\geq 0.261 \pm 0.014$	0.191
$\frac{33}{2}^-$	—	—	0.048	—	0.131

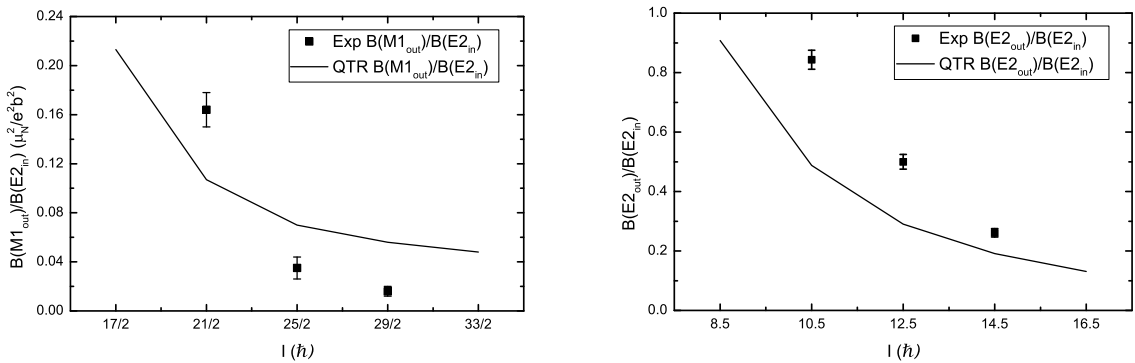


Figure 4.13. Left: Plot of $B(M1_{out})/B(E2_{in})$ ratios for experiment and theory. Right: Plot of $B(E2_{out})/B(E2_{in})$ ratios for experiment and theory.

very weak transition probabilities to the yrast band ($B(E2_{out})/B(E2_{in}) < 0.01$ and $B(E2_{out})/B(M1_{in}) < 0.02\mu_N^2/e^2 b^2$). The experimentally estimated values for the $^{17/2}^- \rightarrow ^{15/2}^-$ transition, 0.0002 and 0.004, respectively, confirm this. The QTR cal-

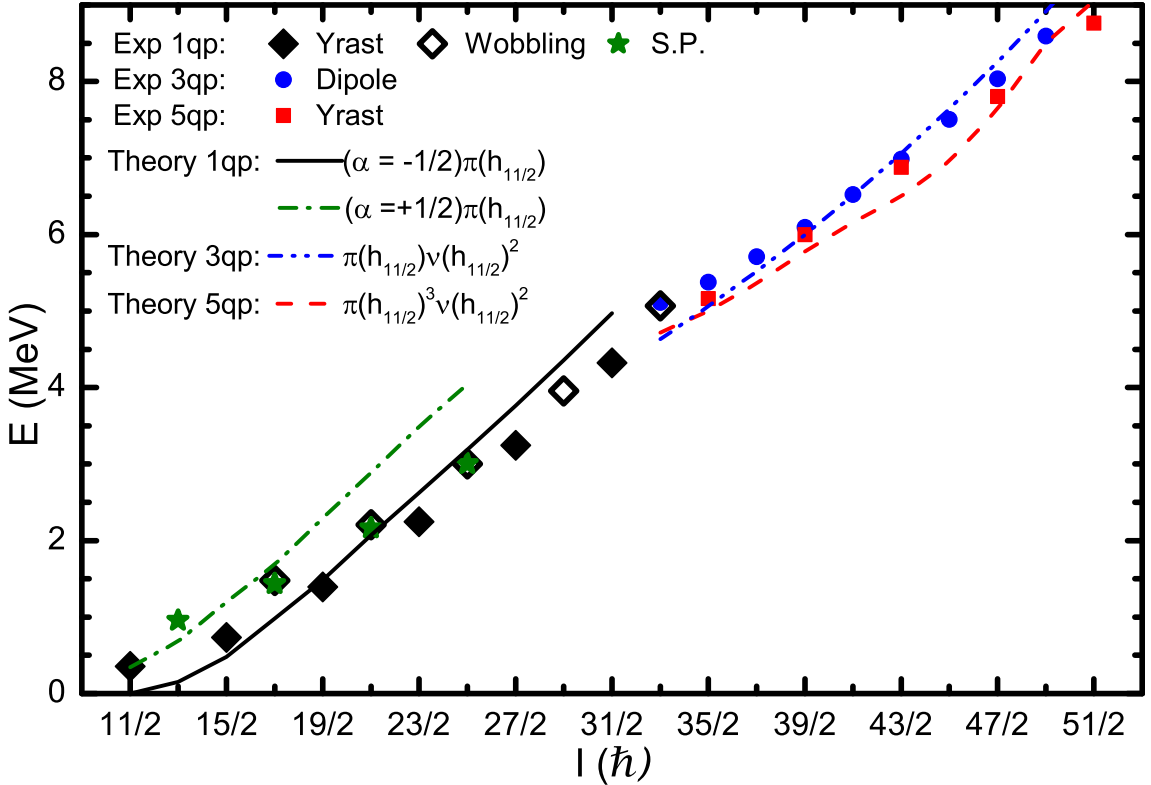


Figure 4.14. Experimental and theoretical (TAC) level energies for the yrast band, $n_w = 1$ band, the signature partner band, and dipole band 1. Error bars for energies are not plotted as they are smaller than the plotted points.

culations predict the signature partner band to be ~ 0.5 MeV higher than found experimentally. The TAC calculations however predict its energy approximately correctly.

With the observation of $\Delta I = 1, E2 n_w = 1 \rightarrow n_w = 0$ transitions, transverse wobbling has been shown conclusively to exist in ^{135}Pr . The very good agreement between experiment and theoretical models proves the understanding of the phenomenon is robust. Transverse wobbling seems to be the solution to the previous discrepancy between the QTR model wobbling energies [48, 49, 110, 111] and the experimentally observed energies. The previous wobblers $^{161,163,165,167}\text{Lu}$ [1, 23, 60, 84, 102] and ^{167}Ta [54] should be reevaluated from the perspective of transverse wobbling. Additionally,

the discovery of transverse wobbling in ^{135}Pr opens up the $A \sim 130$ region for a systematic search for other wobbling bands. Finally the possible $n_w = 2$ band gives hope that the wobbling mode in ^{135}Pr is robust enough to support multiple phonons. With a two phonon band in this energy and spin range, lifetime measurements could be carried out to examine the wobbling phonon and its nature in detail.

CHAPTER 5

SUMMARY AND OUTLOOK

The purpose of this work was two-fold: confirm the theory of transverse wobbling by establishing its existence in ^{135}Pr and show that wobbling can be found outside the $A \sim 160$ mass region. These objectives have been met.

By rearranging the negative parity level scheme and performing a careful angular distribution analysis of the $n_w = 1 \rightarrow n_w = 0$ transitions in that level scheme, clear evidence for the existence of the transverse wobbling mode in ^{135}Pr was found. The $\Delta I = 1, E2$ nature of the transitions gives clear evidence for wobbling. Additionally, the decreasing wobbling energy confirms that the wobbling observed was in fact transverse in nature. This confirms Frauendorf's and Dönau's theory and suggests that the wobblers seen in the $A \sim 160$ region in Refs. [1, 23, 54, 60, 84, 102] should be reevaluated as having transverse nature as well.

The experimental data for the zero and one phonon wobbling states of this nucleus are in fair agreement with QTR calculations. The wobbling energy of the band exhibits the characteristic decrease of a transverse wobbler; however at $J^\pi = ^{29/2}^-$ a minimum is reached and the wobbling energy starts to increase. Calculations show that this is due to the Coriolis force realigning the angular momentum, \vec{j} , of the $h_{11/2}$ proton from the short to the medium axis, causing a transition from the transverse wobbling mode to the longitudinal mode. The experimental upturn is more pronounced due to the yrast band transitioning from a single quasiparticle $\pi(h_{11/2})$ structure to a $\pi(h_{11/2})^3\nu(h_{11/2})^2$ five quasiparticle structure. Intensity in the wobbling band disappears above $J^\pi = ^{33/2}^-$ due to the appearance of an energetically favorable

dipole band with configuration $\pi(h_{11/2})\nu(h_{11/2})^2$, whose band-head has the same J^π and nearly degenerate energy.

A possible $n_w = 2$ band was observed in this work. A further high statistics measurement is needed to confirm the nature of this band. Should the band be a two phonon wobbling band, then ^{135}Pr would be the third nucleus to exhibit this after ^{163}Lu and ^{165}Lu . A proposal for this experiment has been submitted to the ATLAS program advisory committee and beam time has been granted.

With the observation of transverse wobbling in ^{135}Pr , the $A \sim 130$ region has been opened for searches for wobbling. While this region is known to have triaxial deformation, confirmed by the many observations of chirality in the region [5, 51, 55, 64, 79, 91, 108, 123], this is the first observation of wobbling in this region. Studies in this region following up on the work in Ref. [72] show longitudinal wobbling in ^{133}La [12]. Finally, an examination of past data in odd-A members of the region, where the previously identified signature partner bands are interpreted as wobbling bands shows a few cases where the wobbling energy follows the pattern expected for a transverse wobbler, ^{139}Pm , ^{135}La , and ^{131}Cs .

APPENDIX A

GAMMASPHERE RING AND DETECTOR INFORMATION

This appendix contains five tables. In table [A.1](#) the characteristics of each ring of detectors in Gammasphere are given. The ring ID number, ring polar angle θ , number of detectors in the ring, and ID numbers of the detectors in the ring are given for each ring. In table [A.2](#) the detector ID and azimuthal angle ϕ are given for each detector. In table [A.3](#) each ring that was missing detectors for the experiment has the missing detectors listed by ID number. In table [A.4](#) the parameters of the energy calibration polynomial (as in Eqn. [3.16](#)) are listed. In table [A.5](#) the parameters of the relative efficiency calibration polynomial (as in Eqn. [3.17](#)) are listed.

The coordinate system for the angle measurements is as follows: the positive \hat{z} -axis points in the same direction as the beam, the positive \hat{x} -axis points straight into the ground, and the positive \hat{y} -axis points in such a way to form a right-handed coordinate system. Within this framework, the polar angle θ is measured with respect to the positive \hat{z} -axis and the azimuthal angle ϕ is measured from the positive \hat{x} -axis.

TABLE A.1
GAMMASPHERE RING CHARACTERISTICS.

Ring ID	θ ($^{\circ}$)	No. Det	Constituent Detector IDs					
1	17.27465	5	1	3	2	4	6	
2	31.71747	5	5	7	9	8	10	
3	37.37737	5	11	13	12	14	16	
4	50.06504	10	15	17	19	21	23	
			18	20	22	24	26	
5	58.28253	5	25	27	28	35	37	
6	69.82033	10	29	31	33	35	37	
			34	36	38	40	42	
7	79.18768	5	39	41	44	46	48	
8	80.70960	5	43	45	47	50	52	
9	90.00000	10	49	51	53	55	57	
			54	56	58	60	62	
10	99.29040	5	59	61	64	66	68	
11	100.81232	5	63	65	67	70	72	
12	110.17967	10	69	71	73	75	77	
			74	76	78	80	82	
13	121.71747	5	79	81	83	84	86	
14	129.93496	10	85	87	89	91	93	
			88	90	92	94	96	
15	142.62263	5	95	97	99	98	100	
16	148.28253	5	101	103	102	104	106	
17	162.72535	5	105	107	109	108	110	

TABLE A.2
GAMMASPHERE DETECTOR AZIMUTHAL ANGLES.

ID	ϕ (°)								
1	72.00	3	144.00	2	216.00	4	288.00	6	360.00
5	36.00	7	108.00	9	180.00	8	252.00	10	324.00
11	72.00	13	144.00	12	216.00	14	288.00	16	360.00
15	22.84	17	49.16	19	94.84	21	121.16	23	166.84
18	193.16	20	238.84	22	265.16	24	310.84	26	337.16
25	72.00	27	144.00	28	216.00	35	288.00	37	360.00
29	18.49	31	53.51	33	90.49	35	125.51	37	162.49
34	197.51	36	234.49	38	269.51	40	306.49	42	341.51
39	72.00	41	144.00	44	216.00	46	288.00	48	360.00
43	36.00	45	108.00	47	180.00	50	252.00	52	324.00
49	18.00	51	54.00	53	90.00	55	126.00	57	162.00
54	198.00	56	234.00	58	270.00	60	306.00	62	342.00
59	72.00	61	144.00	64	216.00	66	288.00	68	360.00
63	36.00	65	108.00	67	180.00	70	252.00	72	324.00
69	17.51	71	54.49	73	89.51	75	126.49	77	161.51
74	198.49	76	233.51	78	270.49	80	305.51	82	342.49
79	36.00	81	108.00	83	180.00	84	252.00	86	324.00
85	13.16	87	58.84	89	85.16	91	130.84	93	157.16
88	202.84	90	229.16	92	274.84	94	301.16	96	346.84
95	36.00	97	108.00	99	180.00	98	252.00	100	324.00
101	72.00	103	144.00	102	216.00	104	288.00	106	360.00
105	36.00	107	108.00	109	180.00	108	252.00	110	324.00

TABLE A.3
GAMMASPHERE MISSING DETECTORS.

Ring ID	Missing Detector IDs				
1	1	3	2	4	6
2	5	7	10		
4	17	18			
9	53	54	58	59	
15	95				

TABLE A.4
GAMMASPHERE ENERGY CALIBRATION POLYNOMIALS

Det ID	a_0	a_1	a_2	a_3	a_4	a_5
1
2
3
4
5
6
7	-0.39239	0.33375	-1.1729×10^{-7}	8.8275×10^{-12}	0.0	0.0
8	-1.02687	0.33467	-1.0862×10^{-6}	4.8418×10^{-10}	-1.0744×10^{-13}	9.0276×10^{-18}
9	-0.79447	0.33393	-3.0373×10^{-7}	8.0915×10^{-11}	-8.6092×10^{-15}	0.0
10
11	-0.46752	0.33383	-3.1483×10^{-7}	8.6323×10^{-11}	-9.1962×10^{-15}	0.0
12	-1.21363	0.33527	-1.3446×10^{-6}	5.3414×10^{-10}	-1.1158×10^{-13}	9.1266×10^{-18}
13	-0.54146	0.33399	-4.7128×10^{-7}	1.4051×10^{-10}	-1.5058×10^{-14}	0.0

TABLE A.4

Continued

Det ID	a_0	a_1	a_2	a_3	a_4	a_5
14	-1.37449	0.33527	-2.0169×10^{-6}	9.1246×10^{-10}	-1.9684×10^{-13}	1.5946×10^{-17}
15	-1.00592	0.33411	-4.8160×10^{-7}	1.4741×10^{-10}	-1.6032×10^{-14}	0.0
16	-0.81644	0.33404	-1.9640×10^{-7}	1.7848×10^{-11}	0.0	0.0
17
18
19	-0.53012	0.33512	-1.9600×10^{-6}	9.4291×10^{-10}	-2.0580×10^{-13}	1.6457×10^{-17}
20	-0.71551	0.33446	-7.4267×10^{-7}	2.1449×10^{-10}	-2.2596×10^{-14}	0.0
21	-0.87803	0.33443	-5.2558×10^{-7}	1.2631×10^{-10}	-1.2105×10^{-14}	0.0
22	-0.60293	0.33406	-4.0522×10^{-7}	9.7395×10^{-11}	-9.4174×10^{-15}	0.0
23	-0.41724	0.33362	3.2132×10^{-7}	-3.5288×10^{-10}	1.1351×10^{-13}	-1.1955×10^{-17}
24	-0.92102	0.33430	-3.0579×10^{-7}	2.6768×10^{-11}	0.0	0.0
25	-0.20611	0.33344	1.7952×10^{-7}	-1.9597×10^{-10}	6.2653×10^{-14}	-6.6456×10^{-18}
26	-0.69853	0.33463	-1.1077×10^{-6}	4.8788×10^{-10}	-1.0278×10^{-13}	8.0479×10^{-18}

TABLE A.4

Continued

Det ID	a_0	a_1	a_2	a_3	a_4	a_5
27	-0.29011	0.33365	-3.8600×10^{-8}	-1.1595×10^{-10}	5.3898×10^{-14}	-6.7249×10^{-18}
28	-0.82435	0.33452	-6.6905×10^{-7}	1.7454×10^{-10}	-1.7798×10^{-14}	0.0
29	-0.38963	0.33364	1.6204×10^{-7}	-2.4855×10^{-10}	8.7807×10^{-14}	-9.7992×10^{-18}
30	-0.86643	0.33410	1.0110×10^{-7}	-2.9035×10^{-10}	1.0021×10^{-13}	-1.0624×10^{-17}
31	-0.23596	0.33351	2.9406×10^{-7}	-2.8505×10^{-10}	8.9848×10^{-14}	-9.5193×10^{-18}
32	-0.83147	0.33446	-5.9084×10^{-7}	1.5460×10^{-10}	-1.6301×10^{-14}	0.0
33	-0.57768	0.33383	-4.0302×10^{-9}	-1.5027×10^{-10}	6.2492×10^{-14}	-7.5544×10^{-18}
34	-0.82636	0.33458	-9.2505×10^{-7}	3.7015×10^{-10}	-6.9918×10^{-14}	4.8397×10^{-18}
35	-0.36087	0.33284	1.2953×10^{-6}	-8.6019×10^{-10}	2.3071×10^{-13}	-2.1933×10^{-17}
36	-0.61626	0.33449	-7.8304×10^{-7}	2.1912×10^{-10}	-2.2772×10^{-14}	0.0
37	-0.43945	0.33366	2.3611×10^{-7}	-3.1652×10^{-10}	1.0676×10^{-13}	-1.1527×10^{-17}
38	-0.40662	0.33342	5.6189×10^{-7}	-4.8454×10^{-10}	1.4463×10^{-13}	-1.4647×10^{-17}
39	-0.41015	0.33355	2.6163×10^{-7}	-3.0945×10^{-10}	1.0080×10^{-13}	-1.0714×10^{-17}

TABLE A.4

Continued

Det ID	a_0	a_1	a_2	a_3	a_4	a_5
40	-0.53422	0.33349	7.0185×10^{-7}	-6.1128×10^{-10}	1.8218×10^{-13}	-1.8423×10^{-17}
41	-0.63385	0.33416	-5.5994×10^{-7}	1.7214×10^{-10}	-1.8755×10^{-14}	0.0
42	-0.62462	0.33432	-6.2949×10^{-7}	1.8412×10^{-10}	-2.0077×10^{-14}	0.0
43	-0.61144	0.33382	1.6896×10^{-7}	-2.7936×10^{-10}	9.4400×10^{-14}	-1.0082×10^{-17}
44	-0.86073	0.33445	-6.8899×10^{-7}	2.0247×10^{-10}	-2.1926×10^{-14}	0.0
45	-0.35062	0.33384	-2.5896×10^{-7}	6.3126×10^{-11}	-6.6157×10^{-15}	0.0
46	-0.80768	0.33509	-1.4532×10^{-6}	6.6682×10^{-10}	-1.4220×10^{-13}	1.1038×10^{-17}
47	-0.53266	0.33368	2.8624×10^{-7}	-3.3396×10^{-10}	1.0447×10^{-13}	-1.0749×10^{-17}
48	-1.03334	0.33488	-1.0113×10^{-6}	3.0427×10^{-10}	-3.2903×10^{-14}	0.0
49	-0.53465	0.33372	1.6574×10^{-7}	-2.3204×10^{-10}	7.4944×10^{-14}	-7.8298×10^{-18}
50	-0.70354	0.33448	-7.4202×10^{-7}	2.1357×10^{-10}	-2.3162×10^{-14}	0.0
51	-0.50616	0.33345	6.8737×10^{-7}	-5.9237×10^{-10}	1.7837×10^{-13}	-1.8233×10^{-17}
52	-0.80794	0.33517	-1.3261×10^{-6}	5.3233×10^{-10}	-9.9365×10^{-14}	6.6699×10^{-18}

TABLE A.4

Continued

Det ID	a_0	a_1	a_2	a_3	a_4	a_5
53
54
55	-0.56140	0.33347	5.0908×10^{-7}	-4.1655×10^{-10}	1.1988×10^{-13}	-1.1907×10^{-17}
56	-0.96089	0.33486	-1.0059×10^{-6}	3.0046×10^{-10}	-3.2514×10^{-14}	0.0
57	-0.41598	0.33411	-5.9167×10^{-7}	1.7668×10^{-10}	-1.8939×10^{-14}	0.0
58
59
60	-0.83189	0.33439	-5.5198×10^{-7}	1.4601×10^{-10}	-1.5127×10^{-14}	0.0
61	-0.47447	0.33363	3.9498×10^{-7}	-4.2636×10^{-10}	1.3777×10^{-13}	-1.4556×10^{-17}
62	-0.75427	0.33396	1.2183×10^{-7}	-2.7642×10^{-10}	9.6908×10^{-14}	-1.0544×10^{-17}
63	-0.71989	0.33486	-1.2563×10^{-6}	5.6129×10^{-10}	-1.2350×10^{-13}	1.0265×10^{-17}
64
65	-0.54977	0.33349	7.5015×10^{-7}	-5.9685×10^{-10}	1.6725×10^{-13}	-1.6131×10^{-17}

TABLE A.4

Continued

Det ID	a_0	a_1	a_2	a_3	a_4	a_5
66	-0.82956	0.33412	1.7955×10^{-7}	-3.3060×10^{-10}	1.1051×10^{-13}	-1.1607×10^{-17}
67	-0.33019	0.33425	-6.3584×10^{-7}	1.7283×10^{-10}	-1.7686×10^{-14}	0.0
68	-0.81383	0.33449	-6.0252×10^{-7}	1.5771×10^{-10}	-1.6268×10^{-14}	0.0
69	-0.31611	0.33325	6.4119×10^{-7}	-4.6607×10^{-10}	1.3101×10^{-13}	-1.2906×10^{-17}
70	-0.89924	0.33442	-5.5923×10^{-7}	1.4987×10^{-10}	-1.5634×10^{-14}	0.0
71	-0.75887	0.33408	-1.8239×10^{-7}	1.4211×10^{-11}	0.0	0.0
72	-0.59444	0.33403	-1.3230×10^{-7}	-1.2917×10^{-10}	6.1111×10^{-14}	-7.4236×10^{-18}
73	-0.39172	0.33349	3.9475×10^{-7}	-3.4193×10^{-10}	9.8294×10^{-14}	-9.5771×10^{-18}
74	-0.67820	0.33445	-7.5431×10^{-7}	2.1627×10^{-10}	-2.2891×10^{-14}	0.0
75	-0.35622	0.33412	-6.0931×10^{-7}	1.9212×10^{-10}	-2.1293×10^{-14}	0.0
76	-0.59758	0.33367	4.5139×10^{-7}	-4.3606×10^{-10}	1.3046×10^{-13}	-1.3099×10^{-17}
77	-0.42860	0.33385	8.0398×10^{-8}	-2.3816×10^{-10}	8.8892×10^{-14}	-9.9735×10^{-18}
78	-0.26192	0.33320	8.5999×10^{-7}	-6.2838×10^{-10}	1.7181×10^{-13}	-1.6475×10^{-17}

TABLE A.4

Continued

Det ID	a_0	a_1	a_2	a_3	a_4	a_5
79	-0.46585	0.33414	-5.1181×10^{-7}	1.5285×10^{-10}	-1.6537×10^{-14}	0.0
80	-0.42643	0.33332	2.7591×10^{-7}	-2.7914×10^{-10}	8.7532×10^{-14}	-9.1302×10^{-18}
81	-0.53030	0.33365	2.7403×10^{-7}	-3.3267×10^{-10}	1.0898×10^{-13}	-1.1542×10^{-17}
82	-0.41572	0.33338	8.1613×10^{-7}	-6.6138×10^{-10}	1.9071×10^{-13}	-1.8798×10^{-17}
83	-0.48291	0.33368	2.8435×10^{-7}	-3.4250×10^{-10}	1.1259×10^{-13}	-1.2091×10^{-17}
84	-0.78827	0.33395	1.6144×10^{-7}	-3.0307×10^{-10}	1.0359×10^{-13}	-1.1103×10^{-17}
85	-0.76710	0.33427	-5.3006×10^{-7}	1.4113×10^{-10}	-1.4519×10^{-14}	0.0
86	-0.75934	0.33424	-4.8158×10^{-7}	1.2774×10^{-10}	-1.3167×10^{-14}	0.0
87	-0.74432	0.33413	-4.0553×10^{-7}	1.0700×10^{-10}	-1.1077×10^{-14}	0.0
88	-0.76350	0.33429	-5.5826×10^{-7}	1.5874×10^{-10}	-1.7007×10^{-14}	0.0
89	-0.52567	0.33405	-5.0929×10^{-7}	1.6542×10^{-10}	-1.8591×10^{-14}	0.0
90	-0.69111	0.33440	-7.1876×10^{-7}	2.0952×10^{-10}	-2.2143×10^{-14}	0.0
91	-0.66513	0.33363	-4.6168×10^{-8}	0.0	0.0	0.0

TABLE A.4

Continued

Det ID	a_0	a_1	a_2	a_3	a_4	a_5
92	-0.67075	0.33434	-5.8589×10^{-7}	1.6102×10^{-10}	-1.7331×10^{-14}	0.0
93	-0.37561	0.33388	-3.4217×10^{-7}	1.0135×10^{-10}	-1.1216×10^{-14}	0.0
94	-0.52956	0.33429	-6.5245×10^{-7}	2.0067×10^{-10}	-2.1870×10^{-14}	0.0
95
96	-1.25003	0.33527	-1.0943×10^{-6}	2.8333×10^{-10}	-2.7767×10^{-14}	0.0
97	-0.44924	0.33362	2.4212×10^{-7}	-3.1900×10^{-10}	1.0925×10^{-13}	-1.1931×10^{-17}
98	-0.93062	0.33356	9.5686×10^{-7}	-7.6763×10^{-10}	2.1143×10^{-13}	-1.9958×10^{-17}
99	-0.43111	0.33326	6.3928×10^{-7}	-5.1149×10^{-10}	1.5073×10^{-13}	-1.5177×10^{-17}
100	-0.86993	0.33386	3.7055×10^{-7}	-3.9382×10^{-10}	1.2440×10^{-13}	-1.3044×10^{-17}
101	-0.02540	0.33319	5.4696×10^{-7}	-4.2548×10^{-10}	1.2247×10^{-13}	-1.2180×10^{-17}
102	-0.92913	0.33452	-6.8794×10^{-7}	1.9721×10^{-10}	-2.0859×10^{-14}	0.0
103	-0.47449	0.33399	-4.5302×10^{-7}	1.3368×10^{-10}	-1.4534×10^{-14}	0.0
104	-0.39283	0.33399	-4.0178×10^{-7}	1.1517×10^{-10}	-1.2459×10^{-14}	0.0

TABLE A.4

Continued

Det ID	a_0	a_1	a_2	a_3	a_4	a_5
105	-0.82270	0.33485	-1.4268×10^{-6}	7.2708×10^{-10}	-1.7111×10^{-13}	1.4716×10^{-17}
106	-0.73140	0.33459	-7.3556×10^{-7}	2.1253×10^{-10}	-2.2379×10^{-14}	0.0
107	0.09604	0.33240	1.5314×10^{-6}	-9.2177×10^{-10}	2.3430×10^{-13}	-2.1333×10^{-17}
108	-0.64034	0.33426	-5.5793×10^{-7}	1.6141×10^{-10}	-1.7110×10^{-14}	0.0
109	-0.16494	0.33374	-3.2834×10^{-7}	1.0658×10^{-10}	-1.2635×10^{-14}	0.0
110	-0.57994	0.33432	-7.8064×10^{-7}	2.5874×10^{-10}	-2.9346×10^{-14}	0.0

TABLE A.5
GAMMASPHERE RELATIVE EFFICIENCY CALIBRATION
PARAMETERS

Det ID	<i>A</i>	<i>B</i>	<i>C</i>	<i>D</i>	<i>E</i>	<i>F</i>	<i>G</i>
1
2
3
4
5
6
7	-0.30413	1.9150	0.0	0.66092	-0.61764	0.0	12
8	-0.36902	1.9991	0.0	0.75235	-0.53745	0.0	7
9	-0.32479	1.8537	0.0	0.69405	-0.51020	5.1020×10^{-2}	15
10
11	-0.67742	3.2962	0.0	0.69340	-0.65144	0.0	2
12	-0.69510	2.9379	0.0	0.48778	-0.82135	0.0	2

TABLE A.5

Continued

Det ID	<i>A</i>	<i>B</i>	<i>C</i>	<i>D</i>	<i>E</i>	<i>F</i>	<i>G</i>
13	-0.73052	2.1791	-5.9990×10^{-4}	0.62183	-0.59327	-5.3331×10^{-2}	15
14	-1.7863	2.5269	0.0	0.49413	-0.55780	-0.28072	15
15	-1.2019	3.0951	0.0	0.67168	-0.63433	0.0	2
16	-0.10434	1.5739	0.0	0.59481	-0.57224	0.0	15
17
18
19	-1.5328	2.6708	0.0	0.79483	-0.47094	0.0	2
20	-0.43962	3.3655	0.0	0.83511	-0.59681	0.0	2
21	-0.66462	3.1415	0.0	0.60012	-0.70802	0.0	2
22	-0.49528	3.2258	0.0	0.75370	-0.65642	0.0	2
23	-0.66129	3.1392	0.0	0.68736	-0.62643	0.0	2
24	-0.56019	2.9422	0.0	0.56560	-0.70814	4.0594×10^{-3}	2
25	-0.75503	3.4913	0.0	0.70548	-0.61708	0.0	2

TABLE A.5

Continued

Det ID	<i>A</i>	<i>B</i>	<i>C</i>	<i>D</i>	<i>E</i>	<i>F</i>	<i>G</i>
26	-0.32004	1.9165	0.0	0.77511	-0.54187	0.0	15
27	-0.47267	1.8883	0.0	0.68680	-0.49552	0.0	15
28	-0.74742	3.0710	0.0	0.71952	-0.58015	0.0	2
29	-1.0151	3.4204	0.0	0.73533	-0.59057	0.0	2
30	-0.79602	3.3642	0.0	0.64473	-0.60039	0.0	2
31	-1.0144	2.2141	0.0	0.11802	-0.60124	0.0	2
32	-0.82114	3.5192	0.0	0.65474	-0.78140	-0.13510	2
33	-0.82873	3.3871	0.0	0.62924	-0.69905	-9.4051×10^{-2}	2
34	-1.0706	3.1345	0.0	0.61735	-0.49648	-4.9815×10^{-2}	2
35	-1.4193	2.6740	0.0	0.52953	-0.61682	-8.0569×10^{-2}	2
36	-0.80050	3.4582	0.0	0.65383	-0.67516	-0.11997	2
37	-1.1653	3.0872	0.0	0.62836	-0.54001	-8.2477×10^{-2}	2
38	-0.79053	3.1097	0.0	0.76918	-0.55077	4.3575×10^{-2}	2

TABLE A.5

Continued

Det ID	<i>A</i>	<i>B</i>	<i>C</i>	<i>D</i>	<i>E</i>	<i>F</i>	<i>G</i>
39	-0.52317	2.0125	0.0	0.65629	-0.66670	-0.13620	15
40	-0.17284	1.7669	0.0	0.79030	-0.58735	-8.4339×10^{-2}	15
41	-0.42339	1.9315	0.0	0.71051	-0.59727	-7.9150×10^{-2}	15
42	-0.10164	2.3496	0.0	0.80973	-0.61946	5.5401×10^{-2}	2
43	-0.16446	1.7594	0.0	0.74845	-0.57982	-3.9740×10^{-2}	15
44	-0.61791	2.9987	0.0	0.69430	-0.58153	8.4931×10^{-3}	2
45	-0.53733	1.9628	0.0	0.63808	-0.49550	-2.2035×10^{-2}	15
46	-0.62417	2.1106	0.0	0.74566	-0.52567	-4.9563×10^{-2}	15
47	-0.94315	2.3136	0.0	0.68089	-0.61873	-0.17807	15
48	-0.45877	1.9056	0.0	0.68531	-0.66584	-0.14476	15
49	-0.67378	3.0702	0.0	0.74809	-0.65390	-9.1405×10^{-3}	2
50	-0.68991	2.1112	0.0	0.68619	-0.50006	-5.4881×10^{-2}	15
51	-0.38493	1.9154	0.0	0.76405	-0.60734	-0.11918	15

TABLE A.5

Continued

Det ID	<i>A</i>	<i>B</i>	<i>C</i>	<i>D</i>	<i>E</i>	<i>F</i>	<i>G</i>
52	-0.33374	1.8750	0.0	0.67288	-0.56528	-2.6076×10^{-2}	15
53
54
55	0.38448	1.2118	0.0	0.73425	-0.67186	-8.8782×10^{-2}	15
56	-0.26084	1.8413	0.0	0.73827	-0.55848	-5.5329×10^{-2}	15
57	-0.31367	1.8936	0.0	0.78251	-0.57038	-6.9419×10^{-2}	15
58
59
60	-0.77600	2.2056	0.0	0.73567	-0.57665	-0.11366	15
61	-0.54681	2.0642	0.0	0.76831	-0.55805	-6.3466×10^{-2}	15
62	-0.71175	3.3086	0.0	0.76525	-0.58325	-2.5063×10^{-2}	2
63	-0.64430	3.6303	0.0	0.60127	-0.76586	-8.4847×10^{-2}	2
64

TABLE A.5

Continued

Det ID	<i>A</i>	<i>B</i>	<i>C</i>	<i>D</i>	<i>E</i>	<i>F</i>	<i>G</i>
65	-0.59131	4.3585	0.0	0.60409	-0.83772	-0.13426	2
66	-1.1266	2.9884	0.0	0.58476	-0.60667	-8.7052×10^{-2}	2
67	-0.25012	1.7954	0.0	0.68197	-0.60517	-4.9885×10^{-2}	15
68	-0.71239	2.7267	0.0	0.59200	-0.96533	-0.38062	15
69	-0.62644	3.6897	0.0	0.69916	-0.61451	-7.3821×10^{-2}	2
70	-0.46090	1.9872	0.0	0.74578	-0.63395	-0.13381	15
71	-0.29438	1.8686	0.0	0.73693	-0.68803	-0.13649	15
72	-0.18429	1.7992	0.0	0.82022	-0.55794	-7.6548×10^{-2}	15
73	-0.29847	1.8468	0.0	0.69395	-0.59128	-4.5355×10^{-2}	15
74	-0.81039	3.5129	0.0	0.79442	-0.62109	-4.9638×10^{-2}	2
75	-0.41839	1.9649	0.0	0.68650	-0.63270	-8.9372×10^{-2}	15
76	-0.30075	1.8578	0.0	0.77830	-0.55191	-5.5393×10^{-2}	15
77	-0.69758	2.1879	0.0	0.72965	-0.61126	-9.0561×10^{-2}	15

TABLE A.5

Continued

Det ID	<i>A</i>	<i>B</i>	<i>C</i>	<i>D</i>	<i>E</i>	<i>F</i>	<i>G</i>
78	-0.39931	1.9311	0.0	0.63591	-0.76993	-0.16048	15
79	-1.0055	3.4420	0.0	0.80842	-0.59138	1.9421×10^{-2}	2
80	-0.81138	2.2461	0.0	0.69101	-0.54827	-9.1058×10^{-2}	15
81	-0.31378	1.9377	0.0	0.80935	-0.58485	-9.2245×10^{-2}	15
82	-0.65083	2.0388	0.0	0.71091	-0.58940	-0.14479	15
83	-0.26508	1.7919	0.0	0.75000	-0.57154	-4.4759×10^{-2}	15
84	-0.71382	2.2202	0.0	0.79622	-0.59479	-0.12605	15
85	-2.1277	4.3427	0.0	0.63051	-0.57209	-6.9896×10^{-2}	2
86	-0.072342	1.5751	0.0	0.73470	-0.52662	-3.1850×10^{-2}	15
87	-0.30049	1.8327	0.0	0.70430	-0.59214	-4.5312×10^{-2}	15
88	-0.91211	3.5622	0.0	0.75944	-0.56181	1.3241×10^{-2}	2
89	-0.18142	1.8102	0.0	0.80775	-0.60638	-8.6728×10^{-2}	15
90	-0.47193	2.0293	0.0	0.75680	-0.61182	-8.5828×10^{-2}	15

TABLE A.5

Continued

Det ID	<i>A</i>	<i>B</i>	<i>C</i>	<i>D</i>	<i>E</i>	<i>F</i>	<i>G</i>
91	-0.29761	1.7353	0.0	0.64218	-0.58481	-3.6425×10^{-2}	15
92	-0.79997	3.5867	0.0	0.69339	-0.76507	-0.13147	2
93	-0.16718	1.8006	0.0	0.79299	-0.52438	-5.1228×10^{-3}	15
94	0.079896	1.6020	0.0	0.85608	-0.58374	-7.1900×10^{-2}	15
95
96	-0.98269	3.2383	0.0	0.53089	-1.0053	-0.19767	2
97	-0.27413	1.8894	0.0	0.83795	-0.56375	-2.7274×10^{-2}	15
98	-0.49718	2.0975	0.0	0.68291	-0.89499	-0.24412	15
99	-0.36503	1.9761	0.0	0.83954	-0.52936	-3.0208×10^{-2}	15
100	-0.35057	1.8689	0.0	0.69154	-0.66009	-0.11182	15
101	-0.51643	2.0005	0.0	0.80700	-0.55854	-9.6116×10^{-2}	15
102	-0.45526	2.0162	0.0	0.81902	-0.58359	-0.11425	15
103	-0.026845	1.6617	0.0	0.74699	-0.57017	-1.1424×10^{-2}	15

TABLE A.5

Continued

Det ID	<i>A</i>	<i>B</i>	<i>C</i>	<i>D</i>	<i>E</i>	<i>F</i>	<i>G</i>
104	-0.49975	2.0092	0.0	0.70968	-0.53648	-2.8968×10^{-2}	15
105	-1.2169	2.7485	0.0	0.67336	-0.61675	-7.6866×10^{-2}	2
106	-0.62670	2.1207	0.0	0.77935	-0.58520	-7.6038×10^{-2}	15
107	0.17723	1.4377	0.0	0.69797	-0.53417	3.0104×10^{-2}	15
108	-0.66731	2.2447	0.0	0.88377	-0.54142	-8.1666×10^{-2}	15
109	0.38056	1.2189	0.0	0.84465	-0.57378	-1.1694×10^{-2}	15
110	-0.34158	2.0148	0.0	0.84839	-0.59267	-7.5341×10^{-2}	15

APPENDIX B

INGA RING AND DETECTOR INFORMATION

This appendix contains two tables of information about INGA detector positioning. Since INGA’s composition is more fluid than Gammasphere rather than referencing detector numbers, the number of the pocket in the support frame is given. In table B.1 the characteristics of each ring of INGA is given, listing ID number, polar angle θ , number of slots, and which pockets are in the ring. In table B.2 the detector ID and azimuthal angle ϕ , module number, and channel numbers are given for each pocket. If a pocket did not host a detector during the experiment then the module and channel columns are filled with “...”. In table B.3 the parameters of the energy calibration polynomial (as in Eqn. 3.16) are listed.

The coordinate system for the angle measurements is as follows: the positive \hat{z} -axis points in the same direction as the beam, the positive \hat{x} -axis points straight into the ground, and the positive \hat{y} -axis points in such a way to form a right-handed coordinate system. Within this framework, the polar angle θ is measured with respect to the positive \hat{z} -axis and the azimuthal angle ϕ is measured from the positive \hat{x} -axis.

TABLE B.1
INGA RING CHARACTERISTICS.

Ring ID	θ (°)	No. Slots	Pocket No.		
			1	2	3
1	157	3	1	2	3
2	140	3	4	5	6
3	115	3	7	8	9
4	90	6	10	11	12
			13	14	15
5	65	3	16	17	18
6	40	3	19	20	21
7	23	3	22	23	24

TABLE B.2
INGA POCKET AND DETECTOR ELECTRONICS INFORMATION

Pocket	ϕ (°)	Mod	Channels	Pocket	ϕ (°)	Mod	Channels
1	0	0	0 → 3	2	120	0	4 → 7
3	240	0	8 → 11	4	60	0	12 → 15
5	180	1	0 → 3	6	300	1	4 → 7
7	30	1	8 → 11	8	150	1	12 → 15
9	270	2	0 → 3	10	0
11	60	2	8 → 11	12	120	2	12 → 15
13	180	14	240	3	4 → 7
15	300	3	8 → 11	16	90	4	4 → 7
17	210	4	0 → 3	18	330	3	0 → 3
19	180	4	8 → 11	20	60	4	12 → 15
21	300	2	4 → 7	22	120
23	240	24	0

TABLE B.3
INGA ENERGY CALIBRATION POLYNOMIALS

Det ID	a_0	a_1	a_2
0	0.0	0.16200	1.5000×10^{-8}
1	-1.70459	0.31932	-3.3303×10^{-7}
2	-1.23018	0.31886	9.9813×10^{-9}
3	-1.36564	0.31956	-3.2522×10^{-8}
4	-1.65193	0.32876	-3.2565×10^{-7}
5	-1.63814	0.33006	-7.6714×10^{-8}
6	-1.60632	0.26589	4.2319×10^{-9}
7	-2.82354	0.35477	-1.7032×10^{-6}
8	-1.25234	0.34045	1.8887×10^{-8}
9	-1.81279	0.36784	-5.5405×10^{-7}
10	-1.80927	0.34114	-3.0240×10^{-7}
11	-1.56474	0.32675	-4.1622×10^{-8}
12	-1.58655	0.32167	-6.9345×10^{-8}
13	-1.61042	0.32528	-1.1597×10^{-7}
14	-1.42781	0.32174	-7.8135×10^{-8}
15	-1.87322	0.33209	-3.7524×10^{-7}
16
17	-1.29889	0.32792	8.4114×10^{-9}
18	-1.30542	0.32550	2.3746×10^{-8}
19	-1.38423	0.34110	-3.3162×10^{-8}
20	-1.36564	0.31956	-3.2522×10^{-8}
21	-1.74357	0.33728	-3.5346×10^{-7}

TABLE B.3

Continued

Det ID	a_0	a_1	a_2
22	-1.36025	0.33104	-5.7272×10^{-8}
23	-1.58115	0.33721	-6.1847×10^{-8}
24	-1.27541	0.32220	-7.1403×10^{-9}
25	-1.15996	0.31872	5.0068×10^{-8}
26	-1.18230	0.31050	3.3569×10^{-8}
27	-1.50390	0.32520	-2.9113×10^{-7}
28	-0.98916	0.34776	1.1524×10^{-7}
29	-1.31029	0.33130	-2.7831×10^{-8}
30	-1.65588	0.32822	-6.2863×10^{-8}
31	-1.31182	0.32960	-2.4218×10^{-8}
32	-1.75179	0.27567	-2.4791×10^{-7}
33	-1.45115	0.33663	-6.1067×10^{-8}
34	-1.32072	0.32597	-3.2289×10^{-8}
35	-1.66043	0.40873	-1.7636×10^{-7}
36	-1.42765	0.32376	-6.6723×10^{-8}
37	-1.67657	0.32769	-4.4752×10^{-8}
38	-1.40719	0.31903	-2.2180×10^{-8}
39
40	-1.31926	0.29913	-3.8832×10^{-8}
41	-1.54265	0.36882	-5.0330×10^{-8}
42	-1.35012	0.38245	-4.9770×10^{-8}
43	-1.24299	0.36599	-1.1283×10^{-8}

TABLE B.3

Continued

Det ID	a_0	a_1	a_2
44	-1.49393	0.29566	-7.5610×10^{-8}
45	-2.08268	0.80500	-3.7789×10^{-7}
46	-1.41421	0.32319	-3.8744×10^{-8}
47	-1.64014	0.85162	-2.1415×10^{-7}
48	-0.96133	0.17751	9.9178×10^{-9}
49	-1.11860	0.18024	-8.6744×10^{-9}
50
51
52	-1.41655	0.30731	-4.6511×10^{-8}
53	-1.71947	0.29950	-1.9790×10^{-8}
54	-1.41984	0.30509	-3.2770×10^{-8}
55	-1.48353	0.29579	-1.6608×10^{-8}
56	-1.44326	0.34393	-4.3054×10^{-8}
57	-1.60110	0.33154	-2.5961×10^{-8}
58	-1.26956	0.33154	-2.5961×10^{-8}
59	-1.52848	0.34880	2.1485×10^{-8}
60
61
62
63
64	-1.26295	0.33752	2.2936×10^{-8}
65	-1.51122	0.34880	-8.6057×10^{-8}

TABLE B.3

Continued

Det ID	a_0	a_1	a_2
66	-1.50175	0.33550	1.5767×10^{-9}
67	-1.35403	0.32965	-1.2873×10^{-8}
68
69	-1.44491	0.28531	-5.1464×10^{-8}
70
71	-1.31099	0.30930	6.9138×10^{-9}
72	-1.60527	0.33877	-8.2580×10^{-8}
73	1.69134	0.33888	-6.7899×10^{-7}
74	-1.63941	0.33235	-1.0687×10^{-7}
75	-0.37703	0.47270	1.3016×10^{-7}
76
77	-1.70881	0.33008	-1.7548×10^{-7}
78	-1.39461	0.31610	-2.6656×10^{-8}
79	-1.25661	0.33220	-9.4265×10^{-8}

APPENDIX C

NEGATIVE PARITY LEVEL AND TRANSITION INFORMATION

This appendix contains transition information for the negative parity level scheme of ^{135}Pr shown in Fig. 4.5. A table of information for the levels of Fig. 4.5 is present in Table C.1. A table of transition information for the transitions in Fig. 4.5 is present in Table C.2. The errors in level energies are equal to $\sqrt{0.1 \times n}$, where n is the minimum number of gamma rays between that level and the ground state.

TABLE C.1

TABLE OF LEVEL INFORMATION FOR NEGATIVE PARITY ^{135}Pr ,
SORTED BY BAND

Level Energy	J^π	Band
358.0	11/2 ⁻	Yrast
730.8	15/2 ⁻	Yrast
1391.0	19/2 ⁻	Yrast
2245.2	23/2 ⁻	Yrast
3245.3	27/2 ⁻	Yrast
4320.8	31/2 ⁻	Yrast
5164.7	35/2 ⁻	Yrast
5998.6	39/2 ⁻	Yrast

TABLE C.1

Continued

Level Energy	J^π	Band
6880.3	$43/2^-$	Yrast
7803.2	$47/2^-$	Yrast
8760.2	$51/2^-$	Yrast
1477.8	$17/2^-$	$n_w = 1$
2203.8	$21/2^-$	$n_w = 1$
2999.8	$25/2^-$	$n_w = 1$
3955.4	$29/2^-$	$n_w = 1$
5067.4	$33/2^-$	$n_w = 1$
5113.1	$33/2^-$	Dipole Band 1
5711.0	$37/2^-$	Dipole Band 1
6524.4	$41/2^-$	Dipole Band 1
7502.9	$45/2^-$	Dipole Band 1
8595.4	$49/2^-$	Dipole Band 1
5376.4	$35/2^-$	Dipole Band 1
6095.3	$39/2^-$	Dipole Band 1
6983.6	$43/2^-$	Dipole Band 1
8033.1	$47/2^-$	Dipole Band 1
951.9	$13/2^-$	Signature Partner
1433.5	$17/2^-$	Signature Partner
2158.5	$21/2^-$	Signature Partner
3003.5	$(25/2^-)$	Signature Partner
1927.9	$19/2^-$	Possible $n_w = 2$

TABLE C.1

Continued

Level Energy	J^π	Band
2754.3	$23/2^-$	Possible $n_w = 2$
3517.5	$27/2^-$	Possible $n_w = 2$
3864.1	$29/2^-$	Dipole Band 2
4705.1	$33/2^-$	Dipole Band 2
5454.1	$37/2^-$	Dipole Band 2
6507.8	$41/2^-$	Dipole Band 2
2617.1	$23/2^-$	Dipole Band 2
3489.1	$27/2^-$	Dipole Band 2
4294.0	$31/2^-$	Dipole Band 2
5030.1	$35/2^-$	Dipole Band 2
5952.9	$39/2^-$	Dipole Band 2
2715.4	$(21/2^-)$	Unassigned
3381.9	$(25/2^-)$	Unassigned
3531.1	$(27/2^-)$	Unassigned

TABLE C.2

 TABLE OF GAMMA-RAY TRANSITION INFORMATION FOR
 NEGATIVE PARITY ^{135}Pr SORTED BY GAMMA-RAY ENERGY

E_γ	E_i	$Band_i$	\rightarrow	$Band_f$	J_i^π	\rightarrow	J_f^π	I_γ	Mult.
86.8(1)	1478	$n_w = 1$	\rightarrow	Yrast	$17/2^-$	\rightarrow	$19/2^-$	0.3(4)	M1
149.2(1)	3531	Unassigned	\rightarrow	Unassigned	$(27/2^-)$	\rightarrow	$25/2^-$	0.29(4)	M1
221.1(1)	952	Signature Partner	\rightarrow	Yrast	$13/2^-$	\rightarrow	$15/2^-$	1.07(16)	M1
230.6(1)	2158	Signature Partner	\rightarrow	Possible $n_w = 2$	$21/2^-$	\rightarrow	$19/2^-$	3.3(4)	M1
263.3(1)	5376	Dipole Band 1	\rightarrow	Dipole Band 1	$35/2^-$	\rightarrow	$33/2^-$	0.670(16)	M1
309.0(1)	5376	Dipole Band 1	\rightarrow	$n_w = 1$	$35/2^-$	\rightarrow	$33/2^-$	0.690(14)	M1
324.9(1)	5030	Dipole Band 2	\rightarrow	Dipole Band 2	$35/2^-$	\rightarrow	$33/2^-$	1.30(17)	M1
333.0(1)	3864	Dipole Band 2	\rightarrow	Unassigned	$29/2^-$	\rightarrow	$(27/2^-)$	1.70(15)	M1
334.6(1)	5711	Dipole Band 1	\rightarrow	Dipole Band 1	$37/2^-$	\rightarrow	$35/2^-$	1.030(20)	M1
346.6(1)	3864	Dipole Band 2	\rightarrow	Possible $n_w = 2$	$29/2^-$	\rightarrow	$27/2^-$	1.07(5)	M1
372.8(1)	731	Yrast	\rightarrow	Yrast	$15/2^-$	\rightarrow	$11/2^-$	100.0(4)	E2
375.0(1)	3864	Dipole Band 2	\rightarrow	Dipole Band 2	$29/2^-$	\rightarrow	$27/2^-$	0.71(3)	M1

TABLE C.2

Continued

E_γ	E_i	$Band_i$	\rightarrow	$Band_f$	J_i^π	\rightarrow	J_f^π	I_γ	Mult.
382.7(1)	3000	$n_w = 1$	\rightarrow	Dipole Band 2	$25/2^-$	\rightarrow	$23/2^-$	1.11(10)	M1
384.3(1)	6095	Dipole Band 1	\rightarrow	Dipole Band 1	$39/2^-$	\rightarrow	$37/2^-$	0.596(10)	M1
384.3(1)	4705	Dipole Band 2	\rightarrow	Yrast	$33/2^-$	\rightarrow	$31/2^-$	2.04(7)	M1
411.2(1)	4705	Dipole Band 2	\rightarrow	Dipole Band 2	$33/2^-$	\rightarrow	$31/2^-$	1.47(20)	M1
413.3(1)	2617	Dipole Band 2	\rightarrow	$n_w = 1$	$23/2^-$	\rightarrow	$21/2^-$	1.06(10)	M1
424.1(1)	5454	Dipole Band 2	\rightarrow	Dipole Band 2	$37/2^-$	\rightarrow	$35/2^-$	0.90(9)	M1
429.1(1)	6524	Dipole Band 1	\rightarrow	Dipole Band 1	$41/2^-$	\rightarrow	$39/2^-$	0.291(4)	M1
429.8(1)	4294	Dipole Band 2	\rightarrow	Dipole Band 2	$31/2^-$	\rightarrow	$29/2^-$	2.42(22)	M1
450.1(1)	1928	Possible $n_w = 2$	\rightarrow	$n_w = 1$	$19/2^-$	\rightarrow	$17/2^-$	3.25(7)	M1
456.7(1)	4321	Yrast	\rightarrow	Dipole Band 2	$31/2^-$	\rightarrow	$29/2^-$	0.48(7)	M1
459.2(1)	6984	Dipole Band 1	\rightarrow	Dipole Band 1	$43/2^-$	\rightarrow	$41/2^-$	0.188(3)	M1
470.2(1)	2715	Unassigned	\rightarrow	Yrast	$(21/2^-)$	\rightarrow	$23/2^-$	1.15(4)	M1
481.6(1)	1434	Signature Partner	\rightarrow	Signature Partner	$17/2^-$	\rightarrow	$13/2^-$	6.9(3)	E2

TABLE C.2

Continued

E_γ	E_i	$Band_i$	\rightarrow	$Band_f$	J_i^π	\rightarrow	J_f^π	I_γ	Mult.
494.4(1)	1928	Possible $n_w = 2$	\rightarrow	Signature Partner	$19/2^-$	\rightarrow	$17/2^-$	0.3(4)	M1
498.8(1)	5953	Dipole Band 2	\rightarrow	Dipole Band 2	$39/2^-$	\rightarrow	$37/2^-$	0.81(8)	M1
517.7(1)	3517	Possible $n_w = 2$	\rightarrow	$n_w = 1$	$27/2^-$	\rightarrow	$25/2^-$	1.35(7)	M1
519.3(1)	7503	Dipole Band 1	\rightarrow	Dipole Band 1	$45/2^-$	\rightarrow	$43/2^-$	0.1443(24)	M1
525.9(1)	1478	$n_w = 1$	\rightarrow	Signature Partner	$17/2^-$	\rightarrow	$13/2^-$	1.50(12)	E2
530.2(1)	8033	Dipole Band 1	\rightarrow	Dipole Band 1	$47/2^-$	\rightarrow	$45/2^-$	0.0647(16)	M1
550.5(1)	2754	Possible $n_w = 2$	\rightarrow	$n_w = 1$	$23/2^-$	\rightarrow	$21/2^-$	1.91(6)	M1
554.8(1)	6508	Dipole Band 2	\rightarrow	Dipole Band 2	$41/2^-$	\rightarrow	$39/2^-$	0.67(7)	M1
562.3(1)	8595	Dipole Band 1	\rightarrow	Dipole Band 1	$49/2^-$	\rightarrow	$47/2^-$	0.02(3)	M1
593.9(1)	952	Signature Partner	\rightarrow	Yrast	$13/2^-$	\rightarrow	$11/2^-$	9.30(4)	M1
595.8(1)	2754	Possible $n_w = 2$	\rightarrow	Signature Partner	$23/2^-$	\rightarrow	$21/2^-$	1.28(7)	M1
597.8(1)	5711	Dipole Band 1	\rightarrow	Dipole Band 1	$37/2^-$	\rightarrow	$33/2^-$	0.10(12)	E2
660.2(1)	1391	Yrast	\rightarrow	Yrast	$19/2^-$	\rightarrow	$15/2^-$	77.71(3)	E2

TABLE C.2

Continued

E_γ	E_i	$Band_i$	\rightarrow	$Band_f$	J_i^π	\rightarrow	J_f^π	I_γ	Mult.
666.5(1)	3382	Unassigned	\rightarrow	Unassigned	$(25/2^-)$	\rightarrow	$(21/2^-)$	0.6(2)	E2
689.2(1)	2617	Dipole Band 2	\rightarrow	Possible $n_w = 2$	$23/2^-$	\rightarrow	$19/2^-$	6.18(13)	E2
702.7(1)	1434	Signature Partner	\rightarrow	Yrast	$17/2^-$	\rightarrow	$15/2^-$	1.8(5)	M1
710.2(1)	3955	$n_w = 1$	\rightarrow	Yrast	$29/2^-$	\rightarrow	$27/2^-$	0.320(18)	M1
718.9(1)	6095	Dipole Band 1	\rightarrow	Dipole Band 1	$39/2^-$	\rightarrow	$35/2^-$	0.074(4)	E2
725.0(1)	2158	Signature Partner	\rightarrow	Signature Partner	$21/2^-$	\rightarrow	$17/2^-$	3.9(4)	E2
726.0(1)	2204	$n_w = 1$	\rightarrow	$n_w = 1$	$21/2^-$	\rightarrow	$17/2^-$	6.28(5)	E2
734.8(1)	3489	Dipole Band 2	\rightarrow	Possible $n_w = 2$	$27/2^-$	\rightarrow	$23/2^-$	0.161(20)	E2
736.1(1)	5030	Dipole Band 2	\rightarrow	Dipole Band 2	$35/2^-$	\rightarrow	$31/2^-$	0.03(4)	E2
747.0(1)	1478	$n_w = 1$	\rightarrow	Yrast	$17/2^-$	\rightarrow	$15/2^-$	12.00(7)	M1
749.0(1)	5454	Dipole Band 2	\rightarrow	Dipole Band 2	$37/2^-$	\rightarrow	$33/2^-$	0.03(4)	E2
754.6(1)	3000	$n_w = 1$	\rightarrow	Yrast	$25/2^-$	\rightarrow	$23/2^-$	1.92(3)	M1
763.2(1)	3517	Possible $n_w = 2$	\rightarrow	Possible $n_w = 2$	$27/2^-$	\rightarrow	$23/2^-$	1.24(13)	E2

TABLE C.2

Continued

E_γ	E_i	$Band_i$	\rightarrow	$Band_f$	J_i^π	\rightarrow	J_f^π	I_γ	Mult.
767.5(1)	2158	Signature Partner	\rightarrow	Yrast	$21/2^-$	\rightarrow	$19/2^-$	0.7(6)	M1
770.3(1)	2204	$n_w = 1$	\rightarrow	Signature Partner	$21/2^-$	\rightarrow	$17/2^-$	0.0(4)	E2
776.8(1)	3531	Unassigned	\rightarrow	Possible $n_w = 2$	$(27/2^-)$	\rightarrow	$23/2^-$	0.96(8)	E2
796.0(1)	3000	$n_w = 1$	\rightarrow	$n_w = 1$	$25/2^-$	\rightarrow	$21/2^-$	3.50(9)	E2
804.8(1)	4294	Dipole Band 2	\rightarrow	Dipole Band 2	$31/2^-$	\rightarrow	$27/2^-$	0.86(8)	E2
812.8(1)	2204	$n_w = 1$	\rightarrow	Yrast	$21/2^-$	\rightarrow	$19/2^-$	7.60(15)	M1
813.4(1)	6524	Dipole Band 1	\rightarrow	Dipole Band 1	$41/2^-$	\rightarrow	$37/2^-$	0.03(4)	E2
826.4(1)	2754	Possible $n_w = 2$	\rightarrow	Possible $n_w = 2$	$23/2^-$	\rightarrow	$19/2^-$	1.06(6)	E2
833.9(1)	5999	Yrast	\rightarrow	Yrast	$39/2^-$	\rightarrow	$35/2^-$	3.04(7)	E2
841.0(1)	4705	Dipole Band 2	\rightarrow	Dipole Band 2	$33/2^-$	\rightarrow	$29/2^-$	0.18(3)	E2
841.3(1)	3000	$n_w = 1$	\rightarrow	Signature Partner	$25/2^-$	\rightarrow	$21/2^-$	0.47(11)	E2
844.0(1)	5165	Yrast	\rightarrow	Yrast	$35/2^-$	\rightarrow	$31/2^-$	4.94(10)	E2
845.0(1)	3004	Signature Partner	\rightarrow	Signature Partner	$(25/2^-)$	\rightarrow	$21/2^-$	1.37(15)	E2

TABLE C.2

Continued

E_γ	E_i	$Band_i$	\rightarrow	$Band_f$	J_i^π	\rightarrow	J_f^π	I_γ	Mult.
854.2(1)	2245	Yrast	\rightarrow	Yrast	$23/2^-$	\rightarrow	$19/2^-$	35.80(3)	E2
870.8(1)	5165	Yrast	\rightarrow	Dipole Band 2	$35/2^-$	\rightarrow	$31/2^-$	0.62(6)	E2
872.0(1)	3489	Dipole Band 2	\rightarrow	Dipole Band 2	$27/2^-$	\rightarrow	$23/2^-$	2.96(9)	E2
881.7(1)	6880	Yrast	\rightarrow	Yrast	$43/2^-$	\rightarrow	$39/2^-$	2.70(7)	E2
888.3(1)	6984	Dipole Band 1	\rightarrow	Dipole Band 1	$43/2^-$	\rightarrow	$39/2^-$	0.0450(8)	E2
900.4(1)	3517	Possible $n_w = 2$	\rightarrow	Dipole Band 2	$27/2^-$	\rightarrow	$23/2^-$	0.97(5)	E2
914.0(1)	3531	Unassigned	\rightarrow	Dipole Band 2	$(27/2^-)$	\rightarrow	$23/2^-$	0.53(6)	E2
922.9(1)	7803	Yrast	\rightarrow	Yrast	$47/2^-$	\rightarrow	$43/2^-$	1.77(6)	E2
955.6(1)	3955	$n_w = 1$	\rightarrow	$n_w = 1$	$29/2^-$	\rightarrow	$25/2^-$	1.51(4)	E2
957.0(1)	8760	Yrast	\rightarrow	Yrast	$51/2^-$	\rightarrow	$47/2^-$	1.39(5)	E2
978.6(1)	7503	Dipole Band 1	\rightarrow	Dipole Band 1	$45/2^-$	\rightarrow	$41/2^-$	0.0156(8)	E2
1000.1(1)	3245	Yrast	\rightarrow	Yrast	$27/2^-$	\rightarrow	$23/2^-$	9.62(19)	E2
1048.7(1)	4294	Dipole Band 2	\rightarrow	Yrast	$31/2^-$	\rightarrow	$27/2^-$	2.14(9)	E2

TABLE C.2

Continued

E_γ	E_i	$Band_i$	\rightarrow	$Band_f$	J_i^π	\rightarrow	J_f^π	I_γ	Mult.
1049.5(1)	8033	Dipole Band 1	\rightarrow	Dipole Band 1	$47/2^-$	\rightarrow	$43/2^-$	0.0250(8)	E2
1075.5(1)	4321	Yrast	\rightarrow	Yrast	$31/2^-$	\rightarrow	$27/2^-$	5.72(13)	E2
1092.4(1)	8595	Dipole Band 1	\rightarrow	Dipole Band 1	$49/2^-$	\rightarrow	$45/2^-$	0.007(8)	E2
1112.0(1)	5067	$n_w = 1$	\rightarrow	$n_w = 1$	$33/2^-$	\rightarrow	$29/2^-$	0.734(20)	E2
1157.7(1)	5113	Dipole Band 1	\rightarrow	$n_w = 1$	$33/2^-$	\rightarrow	$29/2^-$	0.59(14)	E2
1197.1(1)	1928	Possible $n_w = 2$	\rightarrow	Yrast	$19/2^-$	\rightarrow	$15/2^-$	2.2(3)	E2
1226.1(1)	2617	Dipole Band 2	\rightarrow	Yrast	$23/2^-$	\rightarrow	$19/2^-$	4.54(6)	E2
1243.9(1)	3489	Dipole Band 2	\rightarrow	Yrast	$27/2^-$	\rightarrow	$23/2^-$	1.20(8)	E2
1272.3(1)	3517	Possible $n_w = 2$	\rightarrow	Yrast	$27/2^-$	\rightarrow	$23/2^-$	0.69(10)	E2
1285.9(1)	3531	Unassigned	\rightarrow	Yrast	$(27/2^-)$	\rightarrow	$23/2^-$	2.07(4)	E2
1363.3(1)	2754	Possible $n_w = 2$	\rightarrow	Yrast	$23/2^-$	\rightarrow	$19/2^-$	1.01(12)	E2

BIBLIOGRAPHY

1. H. Amro, W. Ma, G. Hagemann, R. Diamond, J. Domscheit, P. Fallon, A. Grgen, B. Herskind, H. Hbel, D. Jensen, Y. Li, A. Macchiavelli, D. Roux, G. Sletten, J. Thompson, D. Ward, I. Wiedenhver, J. Wilson, and J. Winger. *PHYS LETT B*, 553(34):197 – 203, 2003. doi: [http://dx.doi.org/10.1016/S0370-2693\(02\)03199-4](http://dx.doi.org/10.1016/S0370-2693(02)03199-4). URL <http://www.sciencedirect.com/science/article/pii/S0370269302031994>.
2. C. D. Anderson. *PHYS REV*, 43:491–494, Mar 1933. doi: 10.1103/PhysRev.43.491. URL <http://link.aps.org/doi/10.1103/PhysRev.43.491>.
3. G. Audi, A. Wapstra, and C. Thibault. *NUCL PHYS A*, 729(1):337 – 676, 2003. doi: <http://dx.doi.org/10.1016/j.nuclphysa.2003.11.003>. URL <http://www.sciencedirect.com/science/article/pii/S0375947403018098>.
4. A. Ayangeakaa. *Exotic Modes of Collective Excitations Nuclear Tidal Waves and Chirality*. PhD thesis, University of Notre Dame, 2013.
5. A. D. Ayangeakaa, U. Garg, M. D. Anthony, S. Frauendorf, J. T. Matta, B. K. Nayak, D. Patel, Q. B. Chen, S. Q. Zhang, P. W. Zhao, B. Qi, J. Meng, R. V. F. Janssens, M. P. Carpenter, C. J. Chiara, F. G. Kondev, T. Lauritsen, D. Seweryniak, S. Zhu, S. S. Ghugre, and R. Palit. *PHYS REV LETT*, 110:172504, Apr 2013. doi: 10.1103/PhysRevLett.110.172504. URL <http://link.aps.org/doi/10.1103/PhysRevLett.110.172504>.
6. D. L. Balabanski, M. Danchev, D. J. Hartley, L. L. Riedinger, O. Zeidan, J.-y. Zhang, C. J. Barton, C. W. Beausang, M. A. Caprio, R. F. Casten, J. R. Cooper, A. A. Hecht, R. Krücken, J. R. Novak, N. V. Zamfir, and K. E. Zyromski. *PHYS REV C*, 70:044305, Oct 2004. doi: 10.1103/PhysRevC.70.044305. URL <http://link.aps.org/doi/10.1103/PhysRevC.70.044305>.
7. J. Bardeen, L. N. Cooper, and J. R. Schrieffer. *PHYS REV*, 108:1175–1204, Dec 1957. doi: 10.1103/PhysRev.108.1175. URL <http://link.aps.org/doi/10.1103/PhysRev.108.1175>.
8. A. Baxter, T. Khoo, M. Bleich, M. Carpenter, I. Ahmad, R. Janssens, E. Moore, I. Bearden, J. Beene, and I. Lee. *NUCL INSTRUM METH A*, 317(12):101 – 110, 1992. doi: [http://dx.doi.org/10.1016/0168-9002\(92\)90597-W](http://dx.doi.org/10.1016/0168-9002(92)90597-W). URL <http://www.sciencedirect.com/science/article/pii/016890029290597W>.

9. C. W. Beausang and J. Simpson. *J PHYS G NUCL PARTIC*, 22(5):527, 1996. doi: 10.1088/0954-3899/22/5/003. URL <http://dx.doi.org/10.1088/0954-3899/22/5/003>.
10. S. Belyaev. *MAT FYS MEDD DAN VID*, 31(11), Jan 1959.
11. R. Bengtsson and S. Frauendorf. *Nuclear Physics A*, 314(1):27 – 36, 1979. ISSN 0375-9474. doi: [http://dx.doi.org/10.1016/0375-9474\(79\)90552-9](http://dx.doi.org/10.1016/0375-9474(79)90552-9). URL <http://www.sciencedirect.com/science/article/pii/0375947479905529>.
12. S. Biswas, R. Palit, U. Garg, G. H. Bhat, J. A. Sheikh, S. Frauendorf, J. Sethi, S. Saha, P. Singh, D. Choudhury, W. Li, J. T. Matta, A. D. Ayangeakaa, W. A. Dar, V. Singh, and S. Sihotra. Longitudinal wobbling mode in ^{133}la . *To be published in PRL*, 2015.
13. D. Blumenthal. *A Study of Cooling Following Compound Nuclear Reactions*. PhD thesis, Yale, 1994.
14. A. Bohr. *MAT FYS MEDD DAN VID*, 26(14):1, 1952.
15. A. Bohr and B. R. Mottelson. *PHYS REV*, 89:316–317, Jan 1953. doi: 10.1103/PhysRev.89.316. URL <http://link.aps.org/doi/10.1103/PhysRev.89.316>.
16. A. Bohr and B. R. Mottelson. *Nuclear structure, vol. II*. Benjamin, New York, 1975.
17. A. Bohr and B. R. Mottelson. *MAT FYS MEDD DAN VID*, 27:1, 1953.
18. A. Bohr, B. R. Mottelson, and D. Pines. *PHYS REV*, 110:936–938, May 1958. doi: 10.1103/PhysRev.110.936. URL <http://link.aps.org/doi/10.1103/PhysRev.110.936>.
19. N. Bohr. *NATURE*, 137(3461):344–348, 1936. doi: 10.1038/137344a0. URL <http://dx.doi.org/10.1038/137344a0>.
20. N. Bohr and J. A. Wheeler. *PHYS REV*, 56:426–450, Sep 1939. doi: 10.1103/PhysRev.56.426. URL <http://link.aps.org/doi/10.1103/PhysRev.56.426>.
21. B. Borderie, M. Berlanger, D. Gardés, F. Hanappe, L. Nowicki, J. Pèter, and B. Tamain. *Z PHYS*, 299:263, 1981.
22. S. Botelho, W. A. Seale, L. G. R. Emediato, J. R. B. Oliveira, M. N. Rao, R. V. Ribas, N. H. Medina, E. W. Cybulska, M. A. Rizzutto, F. R. Espinoza-Quiñones, G. García-Bermúdez, H. Somacal, and M. A. Cardona. *PHYS REV C*, 58:3726–3729, Dec 1998. doi: 10.1103/PhysRevC.58.3726. URL <http://link.aps.org/doi/10.1103/PhysRevC.58.3726>.

23. P. Bringel, G. Hagemann, H. Hbel, A. Al-khatib, P. Bednarczyk, A. Brger, D. Curien, G. Gangopadhyay, B. Herskind, D. Jensen, D. Joss, T. Krll, G. Lo Bianco, S. Lunardi, W. Ma, N. Nenoff, A. Neuer-Neffgen, C. Petracche, G. Schnwasser, J. Simpson, A. Singh, N. Singh, and G. Sletten. *EUR PHYS J A*, 24(2):167–172, 2005. doi: 10.1140/epja/i2005-10005-7. URL <http://dx.doi.org/10.1140/epja/i2005-10005-7>.
24. R. Brun and F. Rademakers. *NUCL INSTRUM METH A*, 389(12):81 – 86, 1997. doi: [http://dx.doi.org/10.1016/S0168-9002\(97\)00048-X](http://dx.doi.org/10.1016/S0168-9002(97)00048-X). URL <http://www.sciencedirect.com/science/article/pii/S016890029700048X>. New Computing Techniques in Physics Research V.
25. H. Casimir. On the interaction between atomic nuclei and electrons. In *On the Interaction between Atomic Nuclei and Electrons*, pages 201–283. Springer Netherlands, 1936. ISBN 9789401757201. doi: 10.1007/978-94-017-6067-6_1. URL http://dx.doi.org/10.1007/978-94-017-6067-6_1.
26. R. Casten. *Nuclear Structure from a Simple Perspective*. Oxford science publications. Oxford University Press, 1990. ISBN 9780198507246.
27. J. Cerny, editor. *Nuclear Spectroscopy and Reactions Part C*. Academic Press, 1974.
28. C. J. Chiara, M. Devlin, E. Ideguchi, D. R. LaFosse, F. Lerma, W. Reviol, S. K. Ryu, D. G. Sarantites, O. L. Pechenaya, C. Baktash, A. Galindo-Uribarri, M. P. Carpenter, R. V. F. Janssens, T. Lauritsen, C. J. Lister, P. Reiter, D. Seweryniak, P. Fallon, A. Görzen, A. O. Macchiavelli, D. Rudolph, G. Stoitcheva, and W. E. Ormand. *PHYS REV C*, 75:054305, May 2007. doi: 10.1103/PhysRevC.75.054305. URL <http://link.aps.org/doi/10.1103/PhysRevC.75.054305>.
29. S. Cohen, F. Plasil, and W. Swiatecki. *ANN PHYS-NEW YORK*, 82(2):557 – 596, 1974. doi: [http://dx.doi.org/10.1016/0003-4916\(74\)90126-2](http://dx.doi.org/10.1016/0003-4916(74)90126-2). URL <http://www.sciencedirect.com/science/article/pii/0003491674901262>.
30. A. H. Compton. *PHYS REV*, 21:483–502, May 1923. doi: 10.1103/PhysRev.21.483. URL <http://link.aps.org/doi/10.1103/PhysRev.21.483>.
31. M. Cromaz, T. Symons, G. Lane, I. Lee, and R. MacLeod. *NUCL INSTRUM METH A*, 462(3):519 – 529, 2001. doi: [http://dx.doi.org/10.1016/S0168-9002\(00\)01126-8](http://dx.doi.org/10.1016/S0168-9002(00)01126-8). URL <http://www.sciencedirect.com/science/article/pii/S0168900200011268>.
32. A. Davydov and G. Filippov. *NUCL PHYS*, 8(0):237 – 249, 1958. doi: [http://dx.doi.org/10.1016/0029-5582\(58\)90153-6](http://dx.doi.org/10.1016/0029-5582(58)90153-6). URL <http://www.sciencedirect.com/science/article/pii/0029558258901536>.
33. M. Devlin, L. Sobotka, D. Sarantites, and D. LaFosse. *NUCL INSTRUM METH A*, 383(23):506 – 512, 1996. doi: <http://dx.doi.org/10.1016/>

- S0168-9002(96)00857-1. URL <http://www.sciencedirect.com/science/article/pii/S0168900296008571>.
34. V. I. Dimitrov, S. Frauendorf, and F. Dönau. *PHYS REV LETT*, 84:5732–5735, Jun 2000. doi: 10.1103/PhysRevLett.84.5732. URL <http://link.aps.org/doi/10.1103/PhysRevLett.84.5732>.
 35. G. Duchne, F. Beck, P. Twin, G. de France, D. Curien, L. Han, C. Beausang, M. Bentley, P. Nolan, and J. Simpson. *NUCL INSTRUM METH A*, 432(1):90 – 110, 1999. doi: [http://dx.doi.org/10.1016/S0168-9002\(99\)00277-6](http://dx.doi.org/10.1016/S0168-9002(99)00277-6). URL <http://www.sciencedirect.com/science/article/pii/S0168900299002776>.
 36. J. Eberth, P. V. Brentano, W. Teichert, H. Thomas, A. Werth, R. Lieder, H. Jger, H. Kmmerling, D. Kutchin, K. Maier, M. Berst, D. Gutknecht, and R. Henck. *PROG PART NUCL PHYS*, 28(0):495 – 504, 1992. doi: [http://dx.doi.org/10.1016/0146-6410\(92\)90051-3](http://dx.doi.org/10.1016/0146-6410(92)90051-3). URL <http://www.sciencedirect.com/science/article/pii/0146641092900513>.
 37. A. Einstein. *ANN PHYS-BERLIN*, 322(6):132–148, 1905. doi: 10.1002/andp.19053220607. URL <http://dx.doi.org/10.1002/andp.19053220607>.
 38. S. Frauendorf. *REV MOD PHYS*, 73:463–514, Jun 2001. doi: 10.1103/RevModPhys.73.463. URL <http://link.aps.org/doi/10.1103/RevModPhys.73.463>.
 39. S. Frauendorf. *NUCL PHYS A*, 677(14):115 – 170, 2000. doi: [http://dx.doi.org/10.1016/S0375-9474\(00\)00308-0](http://dx.doi.org/10.1016/S0375-9474(00)00308-0). URL <http://www.sciencedirect.com/science/article/pii/S0375947400003080>.
 40. S. Frauendorf. *NUCL PHYS A*, 557(0):259 – 276, 1993. doi: [http://dx.doi.org/10.1016/0375-9474\(93\)90546-A](http://dx.doi.org/10.1016/0375-9474(93)90546-A). URL <http://www.sciencedirect.com/science/article/pii/037594749390546A>.
 41. S. Frauendorf and F. Dönau. *PHYS REV C*, 89:014322, Jan 2014. doi: 10.1103/PhysRevC.89.014322. URL <http://link.aps.org/doi/10.1103/PhysRevC.89.014322>.
 42. S. Frauendorf and J. Meng. *NUCL PHYS A*, 617(2):131 – 147, 1997. doi: [http://dx.doi.org/10.1016/S0375-9474\(97\)00004-3](http://dx.doi.org/10.1016/S0375-9474(97)00004-3). URL <http://www.sciencedirect.com/science/article/pii/S0375947497000043>.
 43. A. Galindo-Uribarri, H. R. Andrews, G. C. Ball, T. E. Drake, V. P. Janzen, J. A. Kuehner, S. M. Mullins, L. Persson, D. Prévost, D. C. Radford, J. C. Waddington, D. Ward, and R. Wyss. *PHYS REV LETT*, 71:231–234, Jul 1993. doi: 10.1103/PhysRevLett.71.231. URL <http://link.aps.org/doi/10.1103/PhysRevLett.71.231>.
 44. A. Gavron. *PHYS REV C*, 21:230–236, Jan 1980. doi: 10.1103/PhysRevC.21.230. URL <http://link.aps.org/doi/10.1103/PhysRevC.21.230>.

45. M. Goldhaber and A. W. Sunyar. *PHYS REV*, 83:906–918, Sep 1951. doi: 10.1103/PhysRev.83.906. URL <http://link.aps.org/doi/10.1103/PhysRev.83.906>.
46. J. Greene, A. Pawlak, S. Zhu, and U. Garg. *J RADIOANAL NUCL CH*, 299(2):1125–1128, 2014. doi: 10.1007/s10967-013-2675-8. URL <http://dx.doi.org/10.1007/s10967-013-2675-8>.
47. C. Gustafson, L. I. L., B. Nilsson, and S. G. Nilsson. *ARK FYS*, 36:613, 1967.
48. I. Hamamoto. *PHYS REV C*, 65:044305, Mar 2002. doi: 10.1103/PhysRevC.65.044305. URL <http://link.aps.org/doi/10.1103/PhysRevC.65.044305>.
49. I. Hamamoto and G. B. Hagemann. *PHYS REV C*, 67:014319, Jan 2003. doi: 10.1103/PhysRevC.67.014319. URL <http://link.aps.org/doi/10.1103/PhysRevC.67.014319>.
50. W. Hamilton, editor. *The Electromagnetic Interaction in Nuclear Spectroscopy*. North-Holland Publishing Company, 1972.
51. D. J. Hartley, L. L. Riedinger, M. A. Riley, D. L. Balabanski, F. G. Kondev, R. W. Laird, J. Pfohl, D. E. Archer, T. B. Brown, R. M. Clark, M. Devlin, P. Fallon, I. M. Hibbert, D. T. Joss, D. R. LaFosse, P. J. Nolan, N. J. O'Brien, E. S. Paul, D. G. Sarantites, R. K. Sheline, S. L. Shepherd, J. Simpson, R. Wadsworth, J.-y. Zhang, P. B. Semmes, and F. Dönau. *PHYS REV C*, 64:031304, Aug 2001. doi: 10.1103/PhysRevC.64.031304. URL <http://link.aps.org/doi/10.1103/PhysRevC.64.031304>.
52. D. J. Hartley, W. H. Mohr, J. R. Vanhoy, M. A. Riley, A. Aguilar, C. Teal, R. V. F. Janssens, M. P. Carpenter, A. A. Hecht, T. Lauritsen, E. F. Moore, S. Zhu, F. G. Kondev, M. K. Djongolov, M. Danchev, L. L. Riedinger, G. B. Hagemann, G. Sletten, P. Chowdhury, S. K. Tandel, W. C. Ma, and S. W. Ødegård. *PHYS REV C*, 72:064325, Dec 2005. doi: 10.1103/PhysRevC.72.064325. URL <http://link.aps.org/doi/10.1103/PhysRevC.72.064325>.
53. D. J. Hartley, W. H. Mohr, J. R. Vanhoy, M. A. Riley, A. Aguilar, C. Teal, R. V. F. Janssens, M. P. Carpenter, A. A. Hecht, T. Lauritsen, E. F. Moore, S. Zhu, F. G. Kondev, M. K. Djongolov, M. Danchev, L. L. Riedinger, G. B. Hagemann, G. Sletten, P. Chowdhury, S. K. Tandel, W. C. Ma, and S. W. Ødegård. *PHYS REV C*, 74:054314, Nov 2006. doi: 10.1103/PhysRevC.74.054314. URL <http://link.aps.org/doi/10.1103/PhysRevC.74.054314>.
54. D. J. Hartley, R. V. F. Janssens, L. L. Riedinger, M. A. Riley, A. Aguilar, M. P. Carpenter, C. J. Chiara, P. Chowdhury, I. G. Darby, U. Garg, Q. A. Ijaz, F. G. Kondev, S. Lakshmi, T. Lauritsen, A. Ludington, W. C. Ma, E. A. McCutchan, S. Mukhopadhyay, R. Pifer, E. P. Seyfried, I. Stefanescu, S. K. Tandel, U. Tandel, J. R. Vanhoy, X. Wang, S. Zhu, I. Hamamoto, and S. Frauendorf.

- PHYS REV C*, 80:041304, Oct 2009. doi: 10.1103/PhysRevC.80.041304. URL <http://link.aps.org/doi/10.1103/PhysRevC.80.041304>.
55. A. A. Hecht, C. W. Beausang, K. E. Zyromski, D. L. Balabanski, C. J. Barton, M. A. Caprio, R. F. Casten, J. R. Cooper, D. J. Hartley, R. Krückken, D. Meyer, H. Newman, J. R. Novak, E. S. Paul, N. Pietralla, A. Wolf, N. V. Zamfir, J.-Y. Zhang, and F. Dönau. *PHYS REV C*, 63:051302, Apr 2001. doi: 10.1103/PhysRevC.63.051302. URL <http://link.aps.org/doi/10.1103/PhysRevC.63.051302>.
 56. B. Herskind, G. B. Hagemann, G. Sletten, T. Dssing, C. R. Hansen, N. Schunck, S. degrd, H. Hbel, P. Bringel, A. Brger, A. Neusser, A. K. Singh, A. Al-Khatib, S. B. Patel, A. Bracco, S. Leoni, F. Camera, G. Benzoni, P. Mason, A. Paleni, B. Million, O. Wieland, P. Bednarczyk, F. Azaiez, T. Byrski, D. Curien, O. Dakov, G. Duchene, F. Khalfallah, B. Gall, L. Piqeras, J. Robin, J. Dudek, N. Rowley, B. M. Nyak, A. Algora, Z. Dombradi, J. Gal, G. Kalinka, D. Sohler, J. Molnr, J. Timr, L. Zolnai, K. Juhsz, N. Redon, F. Hannachi, J. N. Scheurer, J. N. Wilson, A. Lopez-Martens, A. Korichi, K. Hauschild, J. Roccaz, S. Siem, P. Fallon, I. Y. Lee, A. Grgen, A. Maj, M. Kmiecik, M. Brekiesz, J. Styczen, K. Zuber, J. C. Lisle, B. Cederwall, K. Lagergren, A. O. Evans, G. Rainovski, G. D. Angelis, G. L. Rana, R. Moro, W. Gast, R. M. Lieder, E. Podsvirova, H. Jger, C. M. Petrache, and D. Petrache. *PHYS SCRIPTA*, 2006(T125):108, 2006. URL <http://stacks.iop.org/1402-4896/2006/i=T125/a=025>.
 57. C. Y. Ho, R. W. Powell, and P. E. Liley. *J PHYS CHEM REF DATA*, 1(2):279–421, 1972. doi: <http://dx.doi.org/10.1063/1.3253100>. URL <http://scitation.aip.org/content/aip/journal/jpcrd/1/2/10.1063/1.3253100>.
 58. V. Iacob and G. Duchne. *NUCL INSTRUM METH A*, 399(1):57 – 64, 1997. doi: [http://dx.doi.org/10.1016/S0168-9002\(97\)00872-3](http://dx.doi.org/10.1016/S0168-9002(97)00872-3). URL <http://www.sciencedirect.com/science/article/pii/S0168900297008723>.
 59. R. V. Janssens. *NATURE*, 435(7044):897–898, 2005.
 60. D. R. Jensen, G. B. Hagemann, I. Hamamoto, S. W. Ødegård, B. Herskind, G. Sletten, J. N. Wilson, K. Spohr, H. Hübel, P. Bringel, A. Neußer, G. Schönwaßer, A. K. Singh, W. C. Ma, H. Amro, A. Bracco, S. Leoni, G. Benzoni, A. Maj, C. M. Petrache, G. L. Bianco, P. Bednarczyk, and D. Curien. *PHYS REV LETT*, 89:142503, Sep 2002. doi: 10.1103/PhysRevLett.89.142503. URL <http://link.aps.org/doi/10.1103/PhysRevLett.89.142503>.
 61. A. Kerman and O. Naoki. *NUCL PHYS A*, 361(1):179 – 191, 1981. doi: [http://dx.doi.org/10.1016/0375-9474\(81\)90475-9](http://dx.doi.org/10.1016/0375-9474(81)90475-9). URL <http://www.sciencedirect.com/science/article/pii/0375947481904759>.
 62. C. A. Klein. *IEEE T NUCL SCI*, 15(3):214–225, June 1968. doi: 10.1109/TNS.1968.4324940.

63. G. F. Knoll. *Radiation Detection and Measurement*. John Wiley & Sons, INC., third ed. edition, 2000.
64. T. Koike, K. Starosta, C. J. Chiara, D. B. Fossan, and D. R. LaFosse. *PHYS REV C*, 63:061304, May 2001. doi: 10.1103/PhysRevC.63.061304. URL <http://link.aps.org/doi/10.1103/PhysRevC.63.061304>.
65. A. Krämer-Flecken, T. Morek, R. Lieder, W. Gast, G. Hebbinghaus, H. Jger, and W. Urban. *NUCL INSTRUM METH A*, 275(2):333 – 339, 1989. doi: [http://dx.doi.org/10.1016/0168-9002\(89\)90706-7](http://dx.doi.org/10.1016/0168-9002(89)90706-7). URL <http://www.sciencedirect.com/science/article/pii/0168900289907067>.
66. K. Krane, R. Steffen, and R. Wheeler. *ATOM DATA NUCL DATA*, 11(5):351 – 406, 1973. doi: [http://dx.doi.org/10.1016/S0092-640X\(73\)80016-6](http://dx.doi.org/10.1016/S0092-640X(73)80016-6). URL <http://www.sciencedirect.com/science/article/pii/S0092640X73800166>.
67. K. S. Krane. *ATOM DATA NUCL DATA*, 11(5):407 – 431, 1973. doi: [http://dx.doi.org/10.1016/S0092-640X\(73\)80017-8](http://dx.doi.org/10.1016/S0092-640X(73)80017-8). URL <http://www.sciencedirect.com/science/article/pii/S0092640X73800178>.
68. I.-Y. Lee. *NUCL PHYS A*, 520(0):c641 – c655, 1990. doi: [http://dx.doi.org/10.1016/0375-9474\(90\)91181-P](http://dx.doi.org/10.1016/0375-9474(90)91181-P). URL <http://www.sciencedirect.com/science/article/pii/037594749091181P>. Nuclear Structure in the Nineties.
69. M.A.Riley, C.Baktash, J.Becker, M.P.Carpenter, R.M.Clark, M.Devlin, D.Cline, P.Fallon, D.B.Fossan, S.J.Freedman, S.Flibotte, B.K.Fujikawa, D.S.Haslip, R.V.F.Janssens, T.L.Khoo, F.G.Kondev, R.Kruecken, D. LaFosse, T.Lauritsen, I.Y.Lee, C. Lister, A. Macchiavelli, P.McMahan, W. Nazarewicz, E.B.Norman, L.L.Riedinger, D. Rudolph, D.G.Sarantites, F.S.Stephens, and J.C.Waddington. Gammasphere online booklet. Website. URL <http://nucalp.physics.fsu.edu/~riley/gamma/>. Accessed: 07-15-2015.
70. M. Matsuzaki, Y. R. Shimizu, and K. Matsuyanagi. *PHYS REV C*, 65:041303, Mar 2002. doi: 10.1103/PhysRevC.65.041303. URL <http://link.aps.org/doi/10.1103/PhysRevC.65.041303>.
71. M. Matsuzaki, Y. R. Shimizu, and K. Matsuyanagi. *PHYS REV C*, 69:034325, Mar 2004. doi: 10.1103/PhysRevC.69.034325. URL <http://link.aps.org/doi/10.1103/PhysRevC.69.034325>.
72. J. T. Matta, U. Garg, W. Li, S. Frauendorf, A. D. Ayangeakaa, D. Patel, K. W. Schlax, R. Palit, S. Saha, J. Sethi, T. Trivedi, S. S. Ghugre, R. Raut, A. K. Sinha, R. V. F. Janssens, S. Zhu, M. P. Carpenter, T. Lauritsen, D. Seweryniak, C. J. Chiara, F. G. Kondev, D. J. Hartley, C. M. Petrache, S. Mukhopadhyay, D. V. Lakshmi, M. K. Raju, P. V. Madhusudhana Rao, S. K. Tandel, S. Ray, and F. Dönau. *PHYS REV LETT*, 114:082501, Feb 2015. doi: 10.1103/PhysRevLett.114.082501. URL <http://link.aps.org/doi/10.1103/PhysRevLett.114.082501>.

73. M. G. Mayer. *PHYS REV*, 78:22–23, Apr 1950. doi: 10.1103/PhysRev.78.22. URL <http://link.aps.org/doi/10.1103/PhysRev.78.22>.
74. L. Meitner and O. R. Frisch. *NATURE*, 143(239):1939, 1939.
75. A. Migdal. *NUCL PHYS*, 13(5):655 – 674, 1959. doi: [http://dx.doi.org/10.1016/0029-5582\(59\)90264-0](http://dx.doi.org/10.1016/0029-5582(59)90264-0). URL <http://www.sciencedirect.com/science/article/pii/0029558259902640>.
76. P. Moller, J. Nix, W. Myers, and W. Swiatecki. *ATOM DATA NUCL DATA*, 59(2):185 – 381, 1995. doi: <http://dx.doi.org/10.1006/adnd.1995.1002>. URL <http://www.sciencedirect.com/science/article/pii/S0092640X85710029>.
77. P. Möller, R. Bengtsson, B. G. Carlsson, P. Olivius, and T. Ichikawa. *PHYS REV LETT*, 97:162502, Oct 2006. doi: 10.1103/PhysRevLett.97.162502. URL <http://link.aps.org/doi/10.1103/PhysRevLett.97.162502>.
78. B. R. Mottelson and J. G. Valatin. *PHYS REV LETT*, 5:511–512, Dec 1960. doi: 10.1103/PhysRevLett.5.511. URL <http://link.aps.org/doi/10.1103/PhysRevLett.5.511>.
79. S. Mukhopadhyay, D. Almehed, U. Garg, S. Frauendorf, T. Li, P. V. M. Rao, X. Wang, S. S. Ghugre, M. P. Carpenter, S. Gros, A. Hecht, R. V. F. Janssens, F. G. Kondev, T. Lauritsen, D. Seweryniak, and S. Zhu. *PHYS REV LETT*, 99: 172501, Oct 2007. doi: 10.1103/PhysRevLett.99.172501. URL <http://link.aps.org/doi/10.1103/PhysRevLett.99.172501>.
80. S. Muralithar, K. Rani, R. Kumar, R. Singh, J. Das, J. Gehlot, K. Golda, A. Jhingan, N. Madhavan, S. Nath, P. Sugathan, T. Varughese, M. Archunan, P. Barua, A. Gupta, M. Jain, A. Kothari, B. Kumar, A. Malyadri, U. Naik, R. Kumar, R. Kumar, J. Zacharias, S. Rao, S. Saini, S. Suman, M. Kumar, E. Subramaniam, S. Venkataramanan, A. Dhal, G. Jnaneswari, D. Negi, M. Raju, T. Trivedi, and R. Bhowmik. *NUCL INSTRUM METH A*, 622(1):281 – 287, 2010. doi: <http://dx.doi.org/10.1016/j.nima.2010.06.200>. URL <http://www.sciencedirect.com/science/article/pii/S0168900210013902>.
81. S. Muralithar, K. Rani, R. P. Singh, R. Kumar, J. J. Das, J. Gehlot, K. S. Golda, A. Jhingan, N. Madhavan, S. Nath, P. Sugathan, T. Varughese, M. Archunan, P. Barua, A. Gupta, M. Jain, A. Kothari, B. P. A. Kumar, A. J. Malyadri, U. G. Naik, R. Kumar, R. Kumar, J. Zacharias, S. Rao, S. K. Saini, S. K. Suman, M. Kumar, E. T. Subramaniam, S. Venkataramanan, A. Dhal, G. Jnaneswari, D. Negi, M. K. Raju, T. Trivedi, R. K. Bhowmik, and I. collaboration. *J PHYS G NUCL PARTIC*, 312(5):052015, 2011. URL <http://stacks.iop.org/1742-6596/312/i=5/a=052015>.
82. S. Nilsson. *MAT FYS MEDD DAN VID*, 29(16):1, 1955. URL <https://books.google.com/books?id=R4L5PwaACAAJ>.

83. P. J. Nolan, F. A. Beck, and D. B. Fossan. *ANNU REV NUCL PART S*, 44(1): 561–607, 1994. doi: 10.1146/annurev.ns.44.120194.003021.
84. S. W. Ødegård, G. B. Hagemann, D. R. Jensen, M. Bergström, B. Herskind, G. Sletten, S. Törmänen, J. N. Wilson, P. O. Tjøm, I. Hamamoto, K. Spohr, H. Hübel, A. Görgen, G. Schönwasser, A. Bracco, S. Leoni, A. Maj, C. M. Petrache, P. Bednarczyk, and D. Curien. *PHYS REV LETT*, 86:5866–5869, Jun 2001. doi: 10.1103/PhysRevLett.86.5866. URL <http://link.aps.org/doi/10.1103/PhysRevLett.86.5866>.
85. M. Oi. *PHYS ATOM NUCL*, 70(9):1577–1581, 2007. doi: 10.1134/S106377880709013X. URL <http://dx.doi.org/10.1134/S106377880709013X>.
86. J. R. Oppenheimer and M. S. Plesset. *PHYS REV*, 44:53–55, Jul 1933. doi: 10.1103/PhysRev.44.53.2. URL <http://link.aps.org/doi/10.1103/PhysRev.44.53.2>.
87. R. Palit, S. Saha, J. Sethi, T. Trivedi, S. Sharma, B. Naidu, S. Jadhav, R. Donthi, P. Chavan, H. Tan, and W. Hennig. *NUCL INSTRUM METH A*, 680(0): 90 – 96, 2012. doi: <http://dx.doi.org/10.1016/j.nima.2012.03.046>. URL <http://www.sciencedirect.com/science/article/pii/S0168900212003476>.
88. S. C. Pancholi. *Exotic nuclear excitations*, volume 242. Springer, 2011.
89. N. Pattabiraman, Y. Gu, S. Frauendorf, U. Garg, T. Li, B. Nayak, X. Wang, S. Zhu, S. Ghugre, R. Janssens, R. Chakrawarthy, M. Whitehead, and A. Macchiavelli. *PHYS LETT B*, 647(4):243 – 248, 2007. doi: <http://dx.doi.org/10.1016/j.physletb.2007.01.057>. URL <http://www.sciencedirect.com/science/article/pii/S0370269307001839>.
90. E. S. Paul, C. Fox, A. J. Boston, H. J. Chantler, C. J. Chiara, R. M. Clark, M. Cromaz, M. Descovich, P. Fallon, D. B. Fossan, A. A. Hecht, T. Koike, I. Y. Lee, A. O. Macchiavelli, P. J. Nolan, K. Starosta, R. Wadsworth, and I. Ragnarsson. *PHYS REV C*, 84:047302, Oct 2011. doi: 10.1103/PhysRevC.84.047302. URL <http://link.aps.org/doi/10.1103/PhysRevC.84.047302>.
91. C. Petrache, D. Bazzacco, S. Lunardi, C. R. Alvarez, G. de Angelis, M. D. Poli, D. Bucurescu, C. Ur, P. Semmes, and R. Wyss. *NUCL PHYS A*, 597(1): 106 – 126, 1996. doi: [http://dx.doi.org/10.1016/0375-9474\(95\)00416-5](http://dx.doi.org/10.1016/0375-9474(95)00416-5). URL <http://www.sciencedirect.com/science/article/pii/0375947495004165>.
92. R. Prasad, V. Venugopal, Z. Singh, and D. Sood. *J CHEM THERMO-DYN*, 11(10):963 – 970, 1979. doi: [http://dx.doi.org/10.1016/0021-9614\(79\)90045-4](http://dx.doi.org/10.1016/0021-9614(79)90045-4). URL <http://www.sciencedirect.com/science/article/pii/0021961479900454>.

93. L. B. I. Project. High-spin and nuclear structure home page. Website. URL <http://ie.lbl.gov/toipdf-nilsson.pdf>. Accessed: 07-15-2015.
94. D. Radford. *NUCL INSTRUM METH A*, 361(12):297 – 305, 1995. doi: [http://dx.doi.org/10.1016/0168-9002\(95\)00183-2](http://dx.doi.org/10.1016/0168-9002(95)00183-2). URL <http://www.sciencedirect.com/science/article/pii/0168900295001832>.
95. D. Radford. *NUCL INSTRUM METH A*, 361(12):306 – 316, 1995. doi: [http://dx.doi.org/10.1016/0168-9002\(95\)00184-0](http://dx.doi.org/10.1016/0168-9002(95)00184-0). URL <http://www.sciencedirect.com/science/article/pii/0168900295001840>.
96. J. Rainwater. *PHYS REV*, 79:432–434, Aug 1950. doi: 10.1103/PhysRev.79.432. URL <http://link.aps.org/doi/10.1103/PhysRev.79.432>.
97. S. RAMAN, C. N. JR., and P. TIKKANEN. *ATOM DATA NUCL DATA*, 78(1):1 – 128, 2001. doi: <http://dx.doi.org/10.1006/adnd.2001.0858>. URL <http://www.sciencedirect.com/science/article/pii/S0092640X01908587>.
98. T. W. Raudorf and R. H. Pehl. *NUCL INSTRUM METH A*, 255(3):538 – 551, 1987. doi: [http://dx.doi.org/10.1016/0168-9002\(87\)91225-3](http://dx.doi.org/10.1016/0168-9002(87)91225-3). URL <http://www.sciencedirect.com/science/article/pii/0168900287912253>.
99. P. Ring and P. Schuck. *The Nuclear Many-Body Problem*. Physics and astronomy online library. Springer, 2004. ISBN 9783540212065. URL <https://books.google.com/books?id=PTynSM-nMA8C>.
100. E. Rutherford. *PHILOS MAG*, 21(125):669–688, 1911. doi: 10.1080/14786440508637080. URL <http://dx.doi.org/10.1080/14786440508637080>.
101. H. Schnack-Petersen, R. Bengtsson, R. Bark, P. Bosetti, A. Brockstedt, H. Carlsson, L. Ekstrm, G. Hagemann, B. Herskind, F. Ingebretsen, H. Jensen, S. Leoni, A. Nordlund, H. Ryde, P. Tjm, and C. Yang. *NUCL PHYS A*, 594(2):175 – 202, 1995. doi: [http://dx.doi.org/10.1016/0375-9474\(95\)00363-6](http://dx.doi.org/10.1016/0375-9474(95)00363-6). URL <http://www.sciencedirect.com/science/article/pii/0375947495003636>.
102. G. Schönwaßer, H. Hübel, G. Hagemann, P. Bednarczyk, G. Benzoni, A. Bracco, P. Bringel, R. Chapman, D. Curien, J. Domscheit, B. Herskind, D. Jensen, S. Leoni, G. L. Bianco, W. Ma, A. Maj, A. Neuer, S. Ødegård, C. Petrache, D. Roßbach, H. Ryde, K. Spohr, and A. Singh. *PHYS LETT B*, 552(12):9 – 16, 2003. doi: [http://dx.doi.org/10.1016/S0370-2693\(02\)03095-2](http://dx.doi.org/10.1016/S0370-2693(02)03095-2). URL <http://www.sciencedirect.com/science/article/pii/S0370269302030952>.
103. T. M. Semkow, D. G. Sarantites, K. Honkanen, V. Abenante, L. A. Adler, C. Baktash, N. R. Johnson, I. Y. Lee, M. Oshima, Y. Schutz, Y. S. Chen, J. X. Saladin, C. Y. Chen, O. Dietzsch, A. J. Larabee, L. L. Riedinger, and H. C. Griffin. *PHYS REV C*, 34:523–535, Aug 1986. doi: 10.1103/PhysRevC.34.523. URL <http://link.aps.org/doi/10.1103/PhysRevC.34.523>.

104. Y. R. Shimizu, T. Shoji, and M. Matsuzaki. *PHYS REV C*, 77:024319, Feb 2008. doi: 10.1103/PhysRevC.77.024319. URL <http://link.aps.org/doi/10.1103/PhysRevC.77.024319>.
105. T. Shoji and Y. R. Shimizu. *PROG THEOR PHYS*, 121(2):319–355, 2009.
106. B. Singh and J. Waddington. j^π and multipolarity assignments in $(hi, xnypz\alpha\gamma)$ reactions. Website. URL <http://www.nndc.bnl.gov/nndc/evalcorner/hijpi.pdf>. Accessed: 07-15-2015.
107. K. Starosta, T. Morek, C. Droste, S. Rohoziński, J. Srebrny, A. Wierzchucka, M. Bergström, B. Herskind, E. Melby, T. Czosnyka, and P. Napiorkowski. *NUCL INSTRUM METH A*, 423(1):16 – 26, 1999. doi: [http://dx.doi.org/10.1016/S0168-9002\(98\)01220-0](http://dx.doi.org/10.1016/S0168-9002(98)01220-0). URL <http://www.sciencedirect.com/science/article/pii/S0168900298012200>.
108. K. Starosta, T. Koike, C. J. Chiara, D. B. Fossan, D. R. LaFosse, A. A. Hecht, C. W. Beausang, M. A. Caprio, J. R. Cooper, R. Krücken, J. R. Novak, N. V. Zamfir, K. E. Zyromski, D. J. Hartley, D. L. Balabanski, J.-y. Zhang, S. Frauendorf, and V. I. Dimitrov. *PHYS REV LETT*, 86:971–974, Feb 2001. doi: 10.1103/PhysRevLett.86.971. URL <http://link.aps.org/doi/10.1103/PhysRevLett.86.971>.
109. K. Starosta, D. Fossan, T. Koike, C. Vaman, D. Radford, and C. Chiara. *NUCL INSTRUM METH A*, 515(3):771 – 781, 2003. doi: <http://dx.doi.org/10.1016/j.nima.2003.07.008>. URL <http://www.sciencedirect.com/science/article/pii/S0168900203023131>.
110. K. Tanabe and K. Sugawara-Tanabe. *PHYS REV C*, 73:034305, Mar 2006. doi: 10.1103/PhysRevC.73.034305. URL <http://link.aps.org/doi/10.1103/PhysRevC.73.034305>.
111. K. Tanabe and K. Sugawara-Tanabe. *PHYS REV C*, 77:064318, Jun 2008. doi: 10.1103/PhysRevC.77.064318. URL <http://link.aps.org/doi/10.1103/PhysRevC.77.064318>.
112. O. Tarasov and D. Bazin. *NUCL INSTRUM METH A*, 204(0):174 – 178, 2003. doi: [http://dx.doi.org/10.1016/S0168-583X\(02\)01917-1](http://dx.doi.org/10.1016/S0168-583X(02)01917-1). URL <http://www.sciencedirect.com/science/article/pii/S0168583X02019171>. 14th International Conference on Electromagnetic Isotope Separators and Techniques Related to their Applications.
113. C. Teal, K. Lagergren, A. Aguilar, D. J. Hartley, M. A. Riley, J. Simpson, M. P. Carpenter, U. Garg, R. V. F. Janssens, D. T. Joss, F. G. Kondev, T. Lauritsen, C. J. Lister, X. Wang, S. Zhu, and I. Ragnarsson. *PHYS REV C*, 78:017305, Jul 2008. doi: 10.1103/PhysRevC.78.017305. URL <http://link.aps.org/doi/10.1103/PhysRevC.78.017305>.

114. C. H. Townes, H. M. Foley, and W. Low. *PHYS REV*, 76:1415–1416, Nov 1949. doi: 10.1103/PhysRev.76.1415. URL <http://link.aps.org/doi/10.1103/PhysRev.76.1415>.
115. C. Vaman, D. B. Fossan, T. Koike, K. Starosta, I. Y. Lee, and A. O. Macchiavelli. *PHYS REV LETT*, 92:032501, Jan 2004. doi: 10.1103/PhysRevLett.92.032501. URL <http://link.aps.org/doi/10.1103/PhysRevLett.92.032501>.
116. S. Wang, B. Qi, L. Liu, S. Zhang, H. Hua, X. Li, Y. Chen, L. Zhu, J. Meng, S. Wyngaardt, P. Papka, T. Ibrahim, R. Bark, P. Datta, E. Lawrie, J. Lawrie, S. Majola, P. Masiteng, S. Mullins, J. Gl, G. Kalinka, J. Molnr, B. Nyak, J. Timr, K. Juhsz, and R. Schwengner. *PHYS LETT B*, 703(1):40 – 45, 2011. doi: <http://dx.doi.org/10.1016/j.physletb.2011.07.055>. URL <http://www.sciencedirect.com/science/article/pii/S0370269311008598>.
117. X. Wang. *Exotic Collective Excitations at High Spin: Triaxial Rotation and Octupole Condensation*. PhD thesis, University of Notre Dame, 2008.
118. A. Wapstra, G. Audi, and C. Thibault. *NUCL PHYS A*, 729(1):129 – 336, 2003. doi: <http://dx.doi.org/10.1016/j.nuclphysa.2003.11.002>. URL <http://www.sciencedirect.com/science/article/pii/S0375947403018086>.
119. S. Wen-Xian and C. Qi-Bo. *CHINESE PHYS C*, 39(5):054105, 2015. URL <http://stacks.iop.org/1674-1137/39/i=5/a=054105>.
120. S. Wong. *Introductory Nuclear Physics*. Physics textbook. Wiley, 2008. ISBN 9783527617913.
121. T. Yamazaki. *NUCL DATA SHEETS SEC A*, 3(1):1 – 23, 1967. doi: [http://dx.doi.org/10.1016/S0550-306X\(67\)80002-8](http://dx.doi.org/10.1016/S0550-306X(67)80002-8). URL <http://www.sciencedirect.com/science/article/pii/S0550306X67800028>.
122. Y. C. Zhang, W. C. Ma, A. V. Afanasjev, G. B. Hagemann, J. Begnaud, M. P. Carpenter, P. Chowdhury, D. M. Cullen, M. K. Djongolov, D. J. Hartley, R. V. F. Janssens, T. L. Khoo, F. G. Kondev, T. Lauritsen, E. F. Moore, E. Ngijoi-Yogo, S. Ødegård, L. L. Riedinger, S. V. Rigby, D. G. Roux, D. T. Scholes, R. B. Yadav, J.-Y. Zhang, and S. Zhu. *PHYS REV C*, 76:064321, Dec 2007. doi: 10.1103/PhysRevC.76.064321. URL <http://link.aps.org/doi/10.1103/PhysRevC.76.064321>.
123. S. Zhu, U. Garg, B. K. Nayak, S. S. Ghugre, N. S. Pattabiraman, D. B. Fossan, T. Koike, K. Starosta, C. Vaman, R. V. F. Janssens, R. S. Chakrawarthy, M. Whitehead, A. O. Macchiavelli, and S. Frauendorf. *PHYS REV LETT*, 91:132501, Sep 2003. doi: 10.1103/PhysRevLett.91.132501. URL <http://link.aps.org/doi/10.1103/PhysRevLett.91.132501>.

*This document was prepared & typeset with pdfL^AT_EX, and formatted with
NDdiss2_ε classfile (v3.2013[2013/04/16]) provided by Sameer Vijay and updated
by Megan Patnott.*